TECHNISCHE UNIVERSITÄT WIEN

DIPLOMA THESIS

MXenes as Additives to Green/Environmentally Friendly Lubricants - Tribological Performance Evaluated with a MTM (Mini-Traction Machine) and a Brugger-Tester

zur Erlangung des akademischen Grades

Master of Science

im Rahmen des Studiums

Physikalische Energie und Messtechnik

eingereicht von

Roman Neuhauser

Matrikelnummer 01639380

ausgeführt am Institut für Angewandte Physik

der Fakultät für Physik der Technischen Universität Wien

Betreuer: Univ. Prof. Dr. Markus Valtiner,

Univ. Prof. Dr. Carsten Gachot und

Univ. Ass. Dr. Philipp Grützmacher

_____   _____   _____

Ort, Datum   (Unterschrift Verfasser)   (Unterschrift Betreuer)

Abstract

The development of new lubricants and additives is currently attracting great scientific interest, driven by the high demands for sustainability and enhanced performance. Among the substances drawing attention are ionic liquids (ILs), water and glycerol, each presenting unique opportunities for advancement in lubrication technologies. A promising additive to further improve the performance of traditional lubricants and possibly these new candidates, are transition metal carbides and carbonitrides, called MXenes. MXenes exhibit excellent anti-wear properties, largely due to their distinctive two-dimensional structure. This, coupled with the capability to modify surface termination groups, positions MXenes as highly customizable and versatile lubricant additives.

In this work, we study the potential of two ILs ($[P_{8881}]$ $(BuO)_2PO_2{}^-$ and $[P_{8881}]$ $(MeO)_2PO_2{}^-$) and glycerol as base lubricants in combination with varying amounts of $Ti_3C_2T_x$ multilayer MXenes, exploring their synergistic effects with two tribometers.

Initially, the effectiveness of two ILs, water and glycerol, mixed with a 0.5 wt.-% concentration of MXenes, was evaluated under high-load conditions using the Brugger lubricant tester. The results demonstrated an improvement in the Brugger load-carrying capacity with MXene additives, which necessitated more in-depth analysis with a mini-traction machine (MTM) tribometer. Using the MTM, Ball-on-disc experiments were conducted under varying parameters such as speeds, temperatures, loads, slide-to-roll ratios and MXene concentrations (0.25 and 1 wt.-%) in conditions of non-conformal contact between steel surfaces.

Our results demonstrate that MXenes considerably reduced the coefficient of friction (COF) of the ILs under a broad spectrum of conditions, with the reduction reaching over 80 % at low-speed and high-load environments. This reveals that MXene nanosheets have excellent compatibility with ILs. A subsequent transmission electron microscopy (TEM) characterization of the wear tracks proved that MXene flakes are an integral part of the amorphous tribofilm that was formed by the ILs. In contrast, the combination of glycerol and MXenes exhibited a consistent decrease in performance across the full spectrum of parameters.

Zusammenfassung

Die Entwicklung neuer Schmierstoffe und Additive weckt großes wissenschaftliches Interesse, angetrieben durch hohe Anforderungen an Nachhaltigkeit und verbesserte Leistung. Unter den Substanzen, die Aufmerksamkeit erregen, befinden sich ionische Flüssigkeiten (ILs), Wasser und Glycerin, die einzigartige Möglichkeiten für Fortschritte in der Schmierstofftechnologie bieten. Ein vielversprechendes Additiv, um die Leistung herkömmlicher Schmierstoffe und möglicherweise dieser neuen Kandidaten zu verbessern, sind Übergangsmetallkarbide und -carbonitride, genannt MXene. MXene weisen ausgezeichnete Verschleißschutzeigenschaften auf, die größtenteils auf ihre charakteristische zweidimensionale Struktur zurückzuführen sind. Dies, gepaart mit der Fähigkeit, Oberflächenterminierungsgruppen zu modifizieren, positioniert MXene als hochgradig anpassbare und vielseitige Schmierstoffadditive.

In unserer Arbeit analysieren wir mit zwei unterschiedlichen Tribometern das Potenzial zweier ILs ($[P_{8881}]$ $(BuO)_2PO_2^-$ und $[P_{8881}]$ $(MeO)_2PO_2^-$) sowie Glycerin als Schmierstoffe. Diese werden in Kombination mit variierenden Mengen von $Ti_3C_2T_x$ MXenen untersucht, um ihre synergistischen tribologischen Eigenschaften zu erkunden.

Zunächst wurde die Wirksamkeit von zwei ILs, Wasser und Glycerin, gemischt mit einer 0.5 % Konzentration von MXenen, unter Hochlastbedingungen mit dem Brugger-Schmierstofftester evaluiert. Die Ergebnisse zeigten eine Verbesserung der Brugger-Tragfähigkeit mit MXene-Additiven, was eine eingehendere Analyse mit einem MTM-Tribometer erforderlich machte. Mit der MTM wurden Kugel-auf-Scheibe Versuche mit verschiedenen Parametern wie Geschwindigkeiten, Temperaturen, Lasten, Gleit-zu-Roll-Verhältnissen und MXene-Konzentrationen (0,25 und 1 Gew.-%) unter den Bedingungen eines nicht konformen Kontakts zwischen Stahloberflächen durchgeführt.

Unsere Ergebnisse zeigen, dass MXene die Reibungskoeffizienten der ILs unter einem breiten Spektrum von Bedingungen erheblich reduzierten, wobei die Reduktion bei niedriger Geschwindigkeit und hohen Lastbedingungen über 80 % erreichte. Dies zeigt, dass MXene-Nanoblättchen eine ausgezeichnete Kompatibilität mit ILs aufweisen. Eine anschließende TEM-Charakterisierung der Verschleißspuren bewies, dass MXene ein integraler Bestandteil des amorphen Tribofilms waren, der von den ILs gebildet wurde. Im Gegensatz dazu zeigte die Kombination von Glycerin und MXenen eine konstante Leistungsabnahme über das gesamte Spektrum der Parameter.

Contents

iv

Abbreviations

AFM   Atomic Force Microscopy.
COF   Coefficient Of Friction.
CVD   Chemical Vapor Deposition.
DBP   Dibutyl Phthalate.
DFT   Density functional theory.
DLC   Diamond Like Carbon.
DMP   Dimethyl Phthalate.
DMSO   Dimethyl Sulfoxide.
EDX   Energy Dispersive X-ray.
EHL   Elastohydrodynamic Lubrication.
FIB   Focused Ion Beam.
HCL   Hydrochloric Acid.
HF   Hydrofluoric Acid.
ILs   Ionic Liquids.
MD   Molecular Dynamic.
MILD   Minimally Intensive Layer Delamination.
MTM   Mini-traction Machine.
PVA   Polyvinyl Alcohol.
ROS   Reactive Oxygen Species.
RTILs   Room Temperature Ionic Liquids.
SAED   selected-area electron diffraction.
SEM   Scanning Electron Microscopy.
SLIM   Spacer Layer Imaging.
SRR   Slide-to-roll Ratio.
STEM   Scanning Transmission Electron Microscopy.
TBAOH   Tetrabutylammonium Hydroxide.
TEM   Transmission Electron Microscopy.
TMAOH   Tetramethylammonium Hydroxide.
TMDs   Transition Metal Dichalcogenides.
XPS   X-ray photoelectron spectroscopy.
ZDDP   Zinc Dialkyldithiophosphate.

1 Motivation and Scientific Question

The demand for innovative lubricants and advanced additives is soaring as there is a pressing need to reduce emissions. Enhanced lubricants can raise the lifespans of machinery and guarantee smoother operations and increase efficiency [1–3]. Estimates suggest, that 8 % of the world's total energy usage might be conserved through improved lubrication technologies [3, 4]. Therefore, tribology, the study of friction, wear and lubrication, is vital for advancing sustainability and serves as a gateway towards a more sustainable future. Approximately 20 % [3, 5] of the world's energy is currently used to overcome friction in mechanical systems. This percentage is even higher in transportation, where it's estimated to be around 30 % [3]. Advancements in tribology can lead to improved machine performance, reduced maintenance costs and considerable energy savings [2], highlighting the enormous potential of tribological research.

The prospects of these efficiency gains have sparked a keen interest among researchers to discover and develop new materials. One category of substances that has gained significant attention in this regard are 2D materials, a class of substances notable for their thin, layered structure. Studies have revealed that these materials, consisting of just one or a few atomic layers, can effectively lower the friction coefficient to levels well below 0.01, entering the realm commonly known as superlubricity [6, 7]. Beyond the intrinsically low friction features of 2D material surfaces, the crystalline alignment between two interacting 2D materials can result in an interlayer sliding phenomenon characterized by nearly negligible friction, commonly known as structural superlubricity [6, 8].

Among 2D materials, MXene nanosheets have received considerable recognition. MXenes possess outstanding properties that make them excellent candidates in tribological systems. Similar to many other 2D materials, their laminate structure offers weak inter-layer interactions and easy-to-shear characteristics [9]. Furthermore, MXenes' chemical reactivity allows the formation of tribofilms [10, 11]. A key point in introducing MXenes to tribology is their modifiable surface termination groups, which render them highly versatile lubricants with great adaptability. It has been observed that MXenes can be particularly effective additives in polar-based lubricants such as water or glycerol due to the material's hydrophilicity stemming from the surface termination groups [12].

Recent research in tribology is geared towards identifying environmentally friendly alternatives to conventional oils. It's already established that MXene additives enhance the performance of conventional oils [12]. Among potential substitutes, room temperature ionic liquids (RTILs) show promise due to their non-flammable nature, low volatility and high thermal stability [11]. ILs are polar solvents made of organic cations and a mix of organic or inorganic anions. Studies have shown that ILs can match the tribological effectiveness of mineral oils [13, 14]. The intriguing query now is whether integrating an IL/MXene blend could further enhance this performance.

In summary, the goal of this study is to delve into the relatively uncharted territory of evaluating the performance of a unique mix, consisting of two revolutionary and

highly versatile substances - ionic liquids and MXenes. In addition to investigating ILs, the study also encompasses an analysis of a glycerol-MXene mixture. Glycerol with MXenes has also demonstrated promising results as a sustainable lubricant in scientific research [15, 16], but the pragmatic application of pure glycerol with MXene additives in steel contact areas needs further insight.

Two existing papers [12, 17] authored by the Tribology Research Division and the Austrian Competence Centre for Tribology (AC2T) in Vienna serve as the foundation of this thesis. These papers focus on the application of MXenes and ILs as additives to conventional base oils. The insights gained from the papers strongly suggest that both MXenes and ILs exhibit remarkable potential as additives to enhance the performance of traditional mineral oils. This realization prompted the pursuit of a broader investigation to determine whether the originally used ILs, which were initially employed as additives, can also function effectively as standalone base lubricants. Additionally, the study aims to explore the possibility of further enhancing their lubricant performance by incorporating MXenes as additives. In essence, our approach seeks to evaluate the compatibility and synergy of novel lubricants with MXenes, giving insight into the complexities of interactions between ILs or glycerol combined with MXenes. If their compatibility is confirmed, it unlocks substantial opportunities for creating application-specific tailored lubricants. The possibility of using both substances as additives to conventional mineral oils is also worth considering if the results are promising.

2 Introduction and Scientific Background

2.1 Tribological Background

Tribology, the study of friction, wear, and lubrication, is a scietific field that spans across various engineering disciplines, influencing the design, efficiency and durability of mechanical systems [18]. The name tribology, originates from the Greek word 'tribos' for 'rubbing,' dates back to ancient practices like fire starting and heavy object transportation, with its formal study beginning with Leonardo da Vinci's systematic analysis of friction types in the late 15th century [18]. This interdisciplinary field studies the microscopic interactions between surfaces, explores the properties of lubricants and analyzes the wear mechanisms occurring during tribological loading. By optimizing these interactions, tribology achieves improved performance through reduced energy consumption, noise generation and heat dissipation.

One of the foundational insights in tribology was articulated by Amontons [19] in 1699, proposing that the force of friction is independent of the contact surface area and instead is governed by the applied normal force. This principle was substantiated by Coulomb [20], who also established that the frictional force is unaffected by the sliding speed. He quantified the frictional force with the equation below. In Equation 1, F_R represents the frictional force, F_N denotes the normal force, and μ is the coefficient of friction.

$$F_R = \mu * F_N \tag{1}$$

Bowden and Tabor developed an adhesion-based model [21]. They theorized that during tribological interactions, contact is mainly established at the most elevated points of surface roughness. Consequently, the actual area of contact, dictated by the applied normal force, is smaller than the overall geometric contact surface [21]. This perspective provided by Bowden and Tabor supports that the frictional forces rely on the actual area of contact.

However the relevance of tribology extends beyond historical curiosity. It has practical implications in energy conservation and environmental protection. It is reported that the potential for savings of up to 1.4 % of a country's GDP with minimal investment in tribological research and development is possible [22]. Furthermore, advancements in tribology can contribute to reducing CO_2 emissions by enhancing energy efficiency, particularly in the transportation sector.

The following content introduces various areas of tribology, providing an overview of their features and uses.

- **Classical Tribology:** Focuses on wear and friction in mechanical components and manufacturing processes, emphasizing the importance of lubricants in reducing wear and friction.

- **Bio Tribology:** Applies tribological principles to biological systems, affecting areas such as dentistry and joint replacement.

- **Green Tribology:** Prioritizes environmentally friendly approaches to minimize friction and wear, striving for sustainability and reduced environmental impact.

- **Nano Tribology:** Investigates tribological phenomena at the nanoscale, essential for understanding and improving micro and nano-systems.

- **Computational Tribology:** Utilizes simulation models to study and predict tribological behavior in complex systems.

2.1.1 Wear Mechanisms and Influential Factors

In tribological contacts, wear is a phenomenon that results from the relative motion between two contacting bodies, leading to permanent changes in size, shape, or material of the surface areas involved [23]. This concept of wear encompasses changes in mass or body configuration.

Figure 1 shows the variables that influence wear. Temperature, load, hardness, modulus of elasticity, sliding speed and material composition are key factors that determine wear [22]. Rising temperatures reduce material hardness and yield strength [24], intensifying plastic deformation. Increased loads increases shear forces and friction, accelerating wear [25]. The impact of sliding speed on wear varies depending on factors like load, lubrication and surface topography, while elastic modulus indicates the material's resistance to deformation.
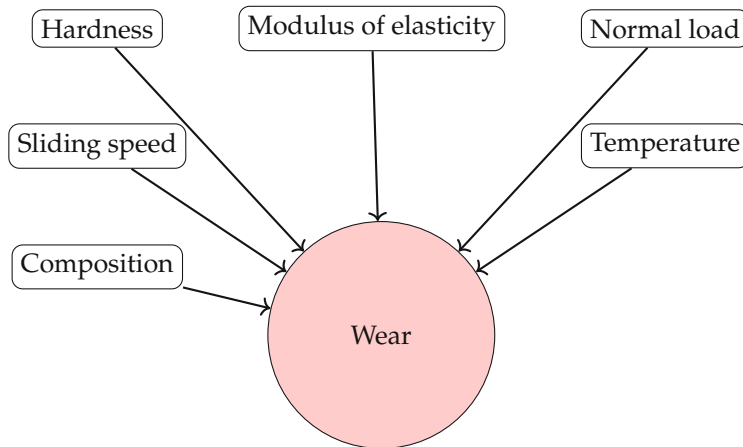

Figure 1: Overview of wear factors, highlighting the key variables impacting material wear. Adapted from ref. [22].

The characteristics of wear, as well as the form and type of resultant wear particles, are direct outcomes of the wear processes [26]. These wear processes involves a variety of phenomena that ultimately change the physical characteristics of materials in contact. The processes of wear are presented in Figure 2. For instance, adhesive wear happens when materials bind together at their interface and wear then occurs, when interacting forces surpass the materials own strength [24]. On the other hand, abrasive wear happens when a harder material erodes a softer one, leading to material loss [24]. This can take the form of either two-body or three-body wear, with the former involving direct contact and material removal by hard particles and the latter occurring when loose particles roll or slide across a surface [27]. Corrosive wear, on

the other hand, is a unique interaction between mechanical abrasion and chemical degradation [27]. This type of wear continuously strips away protective layers from a material, making it more vulnerable to further corrosive attacks [26]. Lastly, surface fatigue is associated with repeated stress cycles that can cause cracks on the material's surface, which is comparable to the way repeated bending can weaken a metal wire until it snaps [27].
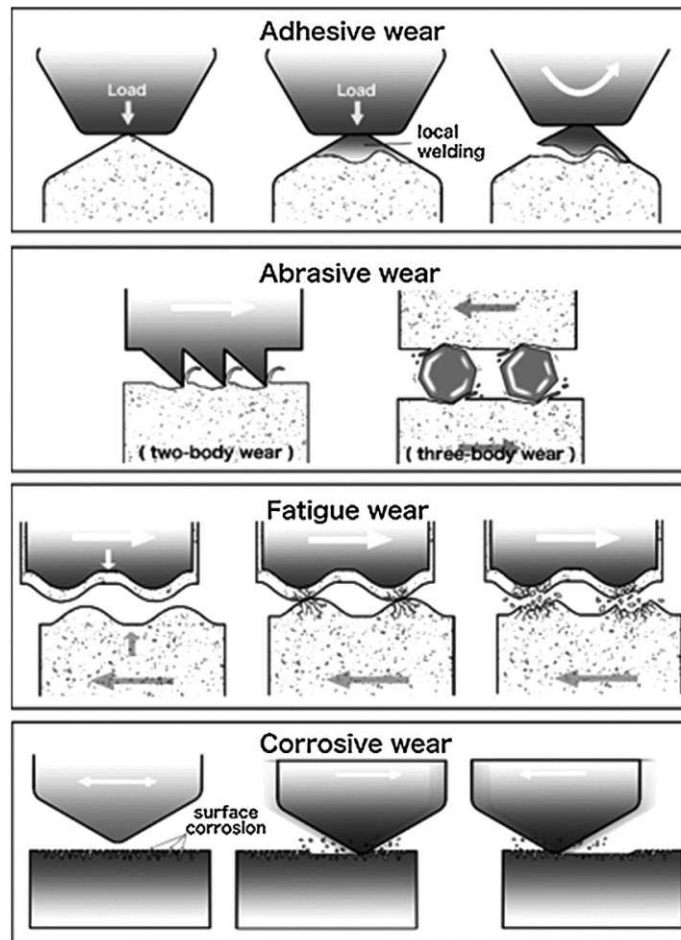

Figure 2: Wear mechanisms including adhesion, abrasion, surface fatigue, and tribochemical reactions. Reprinted from ref. [28] Copyright 2017, Japanese Science Review.

2.1.2 Surface Roughness

Surface roughness of both the base and counter bodies significantly impacts wear and friction. This is because the actual contact areas are considerably smaller than the nominal contact surfaces due to surface roughness [29]. The local stress fields generated by surface roughness contribute to surface degradation.

Surfaces can be evaluated using various roughness parameters. These parameters, while sharing the common goal of quantifying surface irregularities, approach the assessment from different angles. They include the roughness average S_a, root mean square roughness S_q and average height difference between the five highest peaks and the five lowest valleys S_z [30]. Within the roughness reference length, the mean

roughness value S_a is the arithmetic mean of the absolute values of profile deviations. Root mean square roughness S_q is obtained by squaring each height value and then calculating the square root of the mean value [30].

In this work, the surface roughness parameter S_z was evaluated therefore it is necessary to provide a more in-depth explanation of its implications. Equation 2 demonstrates that the S_z value is calculated by taking the arithmetic mean of the five height differences obtained in the previous step. This average represents the S_z parameter, providing insight into the overall height variation between the highest peaks and lowest valleys on the surface.

$$S_z = \frac{1}{5} \sum_{i=1}^{5} |Z_i| \tag{2}$$

2.1.3 Lubricant Film Thickness

Dowson and Higginson [31], as well as Hamrock and Dowson [32], were pioneers in calculating lubricant film thickness. The foundational work by Dowson and Higginson established the basis for numerical predictions of lubricated film thickness in line contacts within elastohydrodynamic lubrication (EHL) theory [33]. Hamrock and Dowson built upon this to specifically enhance film thickness predictions in elliptical contacts [33], significantly extending the theory's relevance to various mechanical components. They established a relationship between the film thickness and various factors such as velocity, load, contact geometry and the properties of the materials and lubricants involved [34]. Their theoretical models received are verified from experiments conducted under conditions where the contacts were smooth and the contact zone was fully flooded with lubricant. Equation 3 represents the equation introduced by Hamrock and Dowson. It models the critical film thickness in lubricated contacts, incorporating the effects of material properties, velocity, load and curvature parameters [32].

$$H_c = 2.69 * G^{0.53} * U^{0.67} * W^{-0.067} \left(1 - 0.61 e^{-0.73k}\right) \tag{3}$$

The parameters in the equation from Hamrock and Dowson [32] are described as follows:

$$
\begin{aligned}
k &\approx 1.03 \left(\frac{R_Y}{R_X}\right)^{0.64} \\
G &= \alpha_p E' \\
U &= \frac{\mu u}{E' R_X} \\
W &= \frac{F}{E' R_X^2}
\end{aligned}
$$

To fully understand the Hamrock-Dowson equation, it is essential to define all parameters involved, as detailed below:

6

- Young's modulus of elasticity E, in Pascals (Pa), quantifies the material's stiffness.

- Equivalent elastic constant $E' = \left(\frac{1-\nu_A^2}{E_A} + \frac{1-\nu_B^2}{E_B}\right)^{-1}$, in Pascals (Pa), combines the elastic properties of materials A and B in contact.

- Base oil viscosity (dynamic) μ_0, in Pascal-seconds (Pa·s), measures the fluid's resistance to gradual deformation.

- Pressure-viscosity coefficient α_p, in inverse Pascals (Pa^{-1}), indicates how the lubricant's viscosity changes with pressure.

- Mean entraining velocity $u = 0.5 \cdot (u_1 + u_2)$, in meters per second (m/s), averages the velocities of two surfaces in contact. Equations by Chittenden et al. and Hamrock & Dowson. Nijenbanning & Moes use the sum velocity: $u = u_1 + u_2$, in m/s.

- Equivalent radii of curvature in the (X, Y) directions (ellipse) R_X, R_Y, in meters (m), describe the contact geometry.

- Normal applied load F, in Newtons (N), is the force exerted perpendicular to the surfaces in contact.

- Material parameter $G = \alpha_p E'$, dimensionless, combines the pressure-viscosity coefficient and the equivalent elastic constant.

- Speed parameter $U = \frac{\eta_0 u}{E' R_X}$, dimensionless, relates the lubricant's viscosity and the contact's entrainment velocity to its geometry and material properties.

- Load parameter $W = \frac{F}{E' R_X^2}$, dimensionless, normalizes the applied load by the material and geometric properties of the contact.

The Barus equation posits that the viscosity μ of a lubricant at a given pressure P can be described by the following relationship:

$$\mu = \mu_0 * e^{\alpha P} \tag{4}$$

where μ_0 is the viscosity at atmospheric pressure, α is the pressure-viscosity coefficient and e is the base of the natural logarithm.

2.1.4 Friction Regimes - Stribeck Curve

The Stribeck curve, proposed by Richard Stribeck in 1901 [35], is a crucial concept in tribology that illustrates the relationship between the COF and the Hersey number, under lubrication. The Hersey number is a dimensionless parameter used in tribology to characterize the lubrication regime of a contact, relating the viscosity of the lubricant, speed of the contact surfaces, and the load or pressure acting on them [35]. Figure 3 serves as a representative example of the Stribeck curve, illustrating the progression of different lubrication regimes. Starting with solid friction, where surfaces in contact rub directly against each other at low speeds without a lubricating film. In the boundary lubrication regime, a thin layer of lubricant molecules adheres

to the surfaces, with asperity contacts bearing most of the load, leading to high friction and wear [24]. Mixed lubrication occurs as a transition between boundary and elastohydrodynamic lubrication, where the load is supported by both asperities and a developing lubricant film, reducing friction and wear [24]. As speed increases, a full-film lubrication develops due to pressure-induced changes in lubricant viscosity and elastic deformation of surfaces, leading to an increase in viscous friction [24].

The lambda ratio (λ) is important in tribology for classifying lubrication regimes. It is defined as:

$$\lambda = \frac{H_c}{\sigma},$$ (5)

where H_c represents the previously discussed central film thickness, and σ is the combined root mean square surface roughness, calculated as:

$$\sigma = \sqrt{Sq_1^2 + Sq_2^2}.$$ (6)

In Figure 3, lubrication regimes are defined by the λ ratio. With $\lambda \geq 3$, the system is in the full film lubrication regime, indicating complete separation by a lubricant film. For $0.1 < \lambda < 3$, it enters the mixed lubrication regime and for For $\lambda \leq 0.1$, the regime is boundary lubrication.
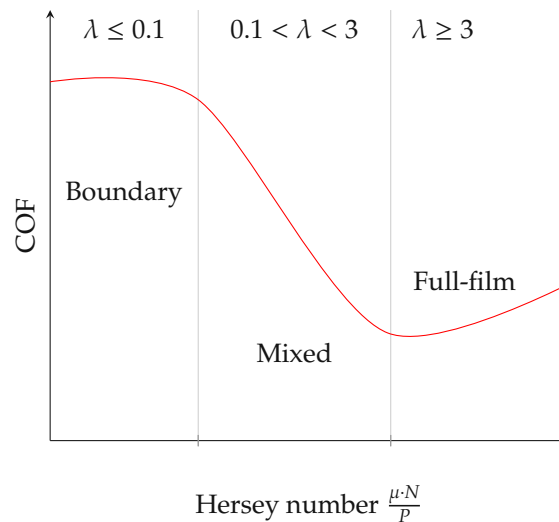

Figure 3: Stribeck Curve illustrating lubrication regimes with the Hersey number (combining viscosity (μ), entrainment speed (N) and load (P)) on the x-axis and coefficient of friction (COF) on the y-axis.

2.2 MXenes

MXenes are a category of inorganic compounds with a two-dimensional structure, composed of atomically thin layers of transition metal carbides, nitrides, or carbonitrides [36]. In 2011, Yuri Gogotsi's and Michel W. Barsoum's research groups at Drexel University uncovered MXenes, revealing an entirely new class of 2D materials [36].

They are described by the formula $M_{n+1}X_nT_x$, where "M" denotes a transition metal, "X" encompasses carbon and/or nitrogen and "T" refers to the surface termination

(e.g., –O, –OH, –F) as can be seen in Figure 4. The bond between the M and X parts shows covalent, metallic and ionic binding characteristics [37]. In this work, $Ti_3C_2T_x$ MXenes supplied by the University of Chile were used. MXenes exhibit an accordion-like morphology [38], depending on the size of sheet-stacks MXenes are categorized as multi-layer MXene (ML-MXene) or few-layer MXene (FL-MXene) when containing fewer than five layers in each stack.
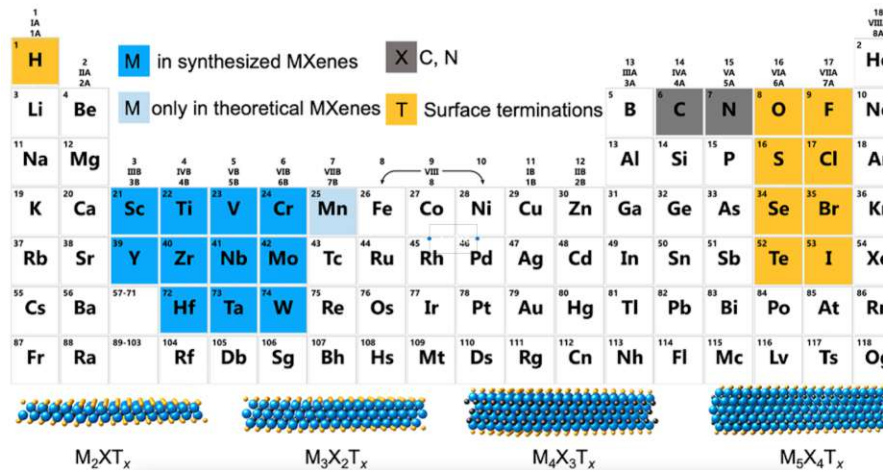

Figure 4: Periodic table with the elements used in the construction of MXenes. Four MXene structures are schematically presented at the bottom. Reprinted from ref. [39] Copyright 2021, American Chemical Society.

Individual $Ti_3C_2T_x$ MXenes sheets have a theoretical height of one to two nanometers and the lateral size varies from 100 nm to 10–20 µm [40]. Due to their exceptionally low height profile, they are part of the two-dimensional materials category that can in general be allocated into five members: Xenes, MXenes, transition metal dichalcogenides (TMDs), nitrides and organic frameworks [41]. One of the most familiar 2D material is graphene, which belongs to the Xene group, as it consists of only one element.

As of 2023, more than 40 [42] MXene compositions have been published. MXenes are obtainable from a range of parent MAX phases, a topic that will be discussed in the following chapter. This opens the door to synthesizing a broad spectrum of MXenes by selecting parent MAX phases that differ in the transition metal (M) or the configuration of carbon or nitrogen (X).
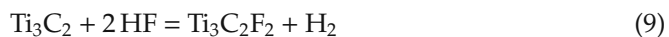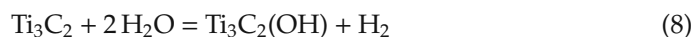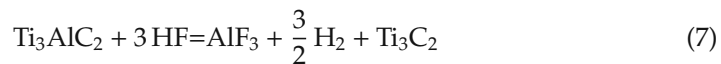
Tunability, one of the most important attributes of this novel material, can be allocated into three fundamental aspects: elemental composition, surface terminations [43] and structural properties. This highlights that uncovering the full potential of MXenes is a gradual process and could pose an ongoing challenge for research. When dealing with MXenes, the elemental composition is typically well understood. However uncovering the other two, surface terminations and structural changes, poses a challenge. Of course, various analytical and characterization techniques are used but comparability is always an issue. Producing MXenes of consistent quality can be tricky [44], as slight deviations in the starting material or the synthesis process can lead to significant deviations. Hence, the following chapter will focus on the

synthesis process.

2.2.1 MXene Synthesis

MXenes have a close association with MAX phases, as their synthesis involves the selective removal of the MAX phase's A element. The term "MAX phase" refers to a family of ternary carbides and nitrides. These layer-structured materials are described by the chemical formula $M_{n+1}AX_n$ [45]. MAX phases can display both metallic and ceramic characteristics under various conditions. Their crystal structure is a layered hexagonal arrangement. The robust M–X bond is a blend of covalent, metallic and ionic binding characteristics, while the weaker M–A bond is purely metallic [37]. Given the weaker M-A bond, selectively removing the MAX phase's A element becomes possible. MAX phases have varying mechanical properties, for instance, they can be pseudo-ductile at high temperatures and fragile at room temperature [45].

The most prevalent approach for extracting the A element from the MAX phase in MXene synthesis involves etching it with hydrofluoric acid (HF). During this process, MAX phases undergo transformation into MXenes, revealing the layered 2D structure. Formula (7) shows the reaction that takes place during the hydrofluoric acid (HF) etching procedure of the Ti_3AlC_2 MAX phase. The remaining Ti atoms of Ti_3C_2 in the first reaction have unpolarized 3d orbits and are adsorbing, that is the reason why they react with the remaining HF or H_2O [41] as seen in (8) and (9). This reaction also results in the creation of -F and -OH groups, which are bound to the outer M layer. The MXenes used in this thesis were etched with the described HF procedure.

$$Ti_3AlC_2 + 3\,HF = AlF_3 + \frac{3}{2}\,H_2 + Ti_3C_2 \qquad (7)$$

$$Ti_3C_2 + 2\,H_2O = Ti_3C_2(OH) + H_2 \qquad (8)$$

$$Ti_3C_2 + 2\,HF = Ti_3C_2F_2 + H_2 \qquad (9)$$

Alternative etching agents include a mix of HF with hydrochloric acid (HCL) or HCL combined with fluoride salts, which results in the generation of HF [44, 46]. Alternative methods being explored include molten salt and electrochemical etching techniques [44, 47, 48]. Other methods such as ball-milling and hydrothermal processes have also been explored for synthesizing $Ti_3C_2T_x$ MXenes [44, 49]. It is important to note, however, that these methods do not begin with a MAX phase precursor. The MXenes produced often maintain a multilayer form [50] with an accordion-like morphology. To achieve delamination into single-layer MXene flakes,

it is necessary to expand the interlayer spacing between the 2D MXenes using intercalating compounds. Successful delamination agents include dimethyl sulfoxide (DMSO), tetrabutylammonium hydroxide (TBAOH) and tetramethylammonium hydroxide (TMAOH) [50].

Additionally, bottom-up synthesis methods like chemical vapor deposition (CVD), template techniques and plasma-enhanced pulsed laser deposition [51–53] have been investigated for creating MXene-based structures. These approaches not only yield high-quality MXenes but also enable the fabrication of structures that are not possible with the etching approach. In 2016, Shahzad et al. [54] found the minimally intensive layer delamination (MILD) method for delaminating MXene sheets, applying manual shaking over sonication and becoming key for high-quality, large flake applications [55]. This technique has emerged as the primary method for producing MXene materials in studies and applications where high-quality, large flakes are required [56].

The multilayer $Ti_3C_2T_x$ nanosheets used in this work were produced through the selective etching process of 2 g of MAX-Ti_3AlC_2 powder, sourced from Forsman Scientific Co. Ltd., Beijing, China, in 20 mL of 40 wt.-% concentration HF. This process involved stirring the Ti_3AlC_2 powder in HF at 60 rpm and maintaining a temperature of 35 °C for a duration of 24 hours. Post-etching, the mixture underwent centrifugation at 3500 rpm, followed by several washes with deionized water until reaching a neutral pH of 6. The resultant product was then vacuum-filtered and subjected to freeze-drying at 60 °C for 24 hours under a vacuum of less than 30 Pa.

Colleagues from our group [57] examined the synthesized MXene's structural integrity, quality and interlayer spacing using the Tecnai F20 TEM from FEI, operated at an acceleration voltage of 200 kV. They also explored surface chemistry attributes via Raman spectroscopy, utilizing a Witec Alpha 300 RA instrument in a backscatter configuration, with an excitation wavelength of 532 nm. Raman spectra ranged from 80 to 1000 cm^{-1}, collected over 128 seconds per spectrum, achieving a spectral resolution of 3 cm^{-1}, facilitated by a 300 lines per mm grating [57].

Their TEM analysis revealed that the synthesis process produced multilayer $Ti_3C_2T_x$ flakes with an interlayer spacing of approximately 0.91 ± 0.09 nm, as seen in Figure 5b. In Figure 5a, the lateral dimensions of one flake can be seen. Furthermore, the hexagonal structure of the flakes was further confirmed by the selected-area electron diffraction (SAED) pattern, visible in the inset of Figure 5b [57]. The Raman results, depicted in Figure 5c, display characteristic vibrational modes at 160, 220, and 707 cm^{-1}, with additional broader peaks at 285, 376, and 600 cm^{-1}. These peaks correspond to the -O, -OH, and -F surface terminations [57].
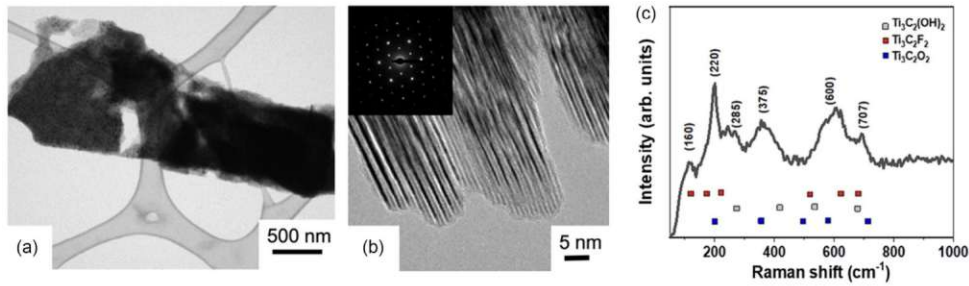
Figure 5: TEM images showing (a) a broader view and (b) a detailed, high-resolution examination, alongside (c) the associated Raman spectrum of the synthesized multilayer $Ti_3C_2T_x$. Reprinted from ref. [57] Copyright 2023, Advanced Engineering Materials.

2.2.2 Challenges in Achieving Stable MXene Dispersions

In many applications, MXenes are employed using a dispersion. Since MXene sheets have a strong tendency to aggregate and form agglomerates, properly dispersing the nanoflakes is not an easy task. Especially, when producing lubricants or coatings only a well-dispersed sample will yield favorable results [10, 58]. Therefore, it is critical to use the right chemical and dispersion procedure to ensure a homogeneous blend. For instance, the natural tendency of MXenes towards hydrophilicity, due to their polar surface terminations, is a key factor in their limited success as additives in pure base oils [10].

When MXenes or other nanomaterials are dispersed in a fluid, the resulting mixture is referred to as a nanofluid [59]. There are three critical factors for nanofluid stability: chemical stability, kinetic stability and thermodynamic stability [60]. Chemical stability is governed by the interactions between particles and between particles and the fluid [59]. Kinetic dispersion stability is influenced by the particle's physical movements, particularly Brownian motion [59], which helps prevent settling and sedimentation by gravity. It is achieved through the energy barrier that prevents the particles from coming together, often facilitated by the viscosity of the base liquid [61]. Lastly, thermodynamic dispersion stability determined by the forces that drive particle agglomeration [60]. Thermodynamic dispersion stability occurs when the dispersed state represents the energetically favored configuration [61].

It is generally observed that when the deviation between interactions of solvent with nanosheets and those among solvent molecules themselves is minimized, the resultant dispersion tends to exhibit enhanced stability [62]. In the context of MXenes, the stability of dispersions is closely associated with both the size of the sheets, the presence of defects within them and the surface termination groups [61]. Iqbal et al. for instance discovered that synthesizing larger MXene flakes using optimized methods yielded dispersions with significantly enhanced agglomeration resistance. This finding suggests the potential existence of an optimal sheet size range for MXenes, balancing dispersion stability with other desirable properties such as oxidation characteristics [63].

Highly viscous solvents, such as ILs, provide substantial kinetic dispersion stability

Die approbierte gedruckte Originalversion dieser Diplomarbeit ist an der TU Wien Bibliothek verfügbar
The approved original version of this thesis is available in print at TU Wien Bibliothek.

TU Bibliothek
Your knowledge hub
WIEN

[61]. While this stability differs fundamentally from true thermodynamic dispersion stability [61], it holds significant advantages in tribological applications [10].

Ultrasonication for the preparation of MXene nanofluids has proven effective for properly dispersing the material. However, the final result depends on various factors, such as the frequency or the viscosity of the base liquid [64]. Sonication leads to pressure differences and cavitation between the sheets, resulting in exfoliation (further delamination). Throughout the sonication process, it's important to note that the flakes may undergo degradation. This results in a reduction of the sheet size and smaller sheets are often associated with lower quality. When multilayer MXene flakes are needed, it is crucial to precisely control the power applied during the sonication process. High power can decrease the number of layers in the MXene stacks.

In the context of tribological applications, sonication emerges as the preferred method for dispersing MXenes, as it effectively reduces the presence of multilayer MXenes and enables a well-dispersed medium [65]. The further delamination has a beneficial effect as increasing the concentration of MXene multilayer particles beyond optimal levels can cause an increase in friction, mainly due to agglomerations [66], that affect the stability and quality of the dispersion.

Maleski et al. carried out a comparative analysis on the effectiveness of various organic solvents (including water, ethanol and acetone) as dispersion media for MXenes. Their research, referenced in [61], demonstrated that the MXenes they investigated exhibited remarkably extended periods before sedimentation occurred. When comparing these results to the MXenes examined in our study, it's evident that the superior performance observed in Maleski et al.'s work can be attributed to variations in surface terminations, lateral dimensions, and the presence of defects. In a previous thesis [67], water and ethanol were employed as dispersion mediums for the same MXenes, resulting in notably faster sedimentation compared to Maleski et al's findings.

2.2.3 Durability and Oxidation Resistance of MXenes

Oxidation stability is a major problem across many MXene applications, as MXenes are prone to structural changes and phase transformations under ambient conditions. The Ti element of this 2D material is known to react with CO_2 or H_2O and form TiO_2 nanoparticles. The speed of this reaction is amplified at higher temperatures [68, 69] and TiO_2 particles have deviating properties and therefore they are unwanted in almost all applications.

The research conducted on the oxidation of MXenes has presented inconsistent and sometimes contradictory results across different groups [70]. While some studies suggest that MXenes exhibit exceptional stability under oxidative conditions, others have reported significant degradation of these materials upon exposure to the same conditions [70]. These deviations in the results are influenced by synthesis processes as the oxidation stability of $Ti_3C_2T_x$ is strongly dependent on the grade of the MXenes [70].

Researchers have found multiple ways to increase the oxidation stability. Many of these approaches are related to the synthesis process, as each stage in the synthesis of MXenes has a significant impact on their ultimate structure, physiochemical characteristics and their oxidation resistance [40].

Mathis et al. demonstrated a correlation between the oxidation stability and the grade of the MXenes [71]. They sought to address the instability and rapid oxidation that have limited the potential commercial use and further research of $Ti_3C_2T_x$ MXenes. To achieve this, they added excess aluminum during the synthesis of the Ti_3AlC_2 MAX phase precursor, resulting in the production of Ti_3AlC_2 grains with improved stoichiometry and crystallinity. This, in turn, led to the creation of higher-quality $Ti_3C_2T_x$ nanosheets with improved electrical conductivity and greater resistance to oxidation. The improved MXene had significantly greater stability in both aqueous solutions and ambient air [71], resulting in a much longer shelf life compared to conventional $Ti_3C_2T_x$. They suggest that eliminating defects during the synthesis can greatly enhance its stability and electrical properties, facilitating its widespread use in various fields [71].

Another process that has proven to slow down oxidation is hydrogen annealing. Hydrogen annealing refers to a heat treatment process where a material is exposed to hydrogen gas at high temperature for an extended period, to improve its microstructure and mechanical properties [72]. The hydrogen atoms diffuse into the MXenes and react with the nanomaterial, leading to the improvement of oxidation properties. Hydrogen annealing changes the surface functional groups of the MXene, because the number of –OH terminations on the surface decreases, whereas the number of –O terminations increases. This is accompanied by an increase in oxidation resistance [72].

Additionally, MXene composites with polymers could lengthen the lifespan. According to Habib et al., the oxidation rate of $Ti_3C_2T_x$ MXene polymeric composites with polyvinyl alcohol (PVA) was slower, due to hydrogen bonding between the MXene nanosheets and polymeric chains [73]. This formed an MXene/PVA sandwich structure that showed improved oxidation stability.

2.2.4 Tribological Properties of MXenes

The discovery of graphene in 2004 started the era of two-dimensional materials [74]. Building upon the success of graphene, the exploration of two-dimensional materials expanded, leading to the discovery of MXenes. Following these discoveries, analysis for tribological applications started soon after. Regarding application methods, MXenes exhibit remarkable versatility, as they can be effectively applied through various deposition techniques readily available. Liquid dispersion, spray coating, drop casting, inkjet printing, spin coating and vacuum filtration are the most common methods for applying MXenes [75]. Therefore, in tribology, MXenes can be employed in solid lubrication, liquid lubrication and as additives for reinforcement composites [65]. With MXenes as additives for liquid lubrication, it has been shown, that the desired reduction of friction can already be observed at relatively small quantities of the nanomaterial, in the range of 0.1 to 1 wt.-%. [16, 57, 76].

The stack morphology of MXenes is beneficial for reducing friction and wear, as the individual sheets are loosely bound together after the etching process. These weak interactions between layers contribute to low shear strength between individual layers [77].

The high specific surface area of MXenes facilitates the formation of lubricating or transfer films, called tribofilms [65]. The formation of this film on both surfaces within the contact area allows MXenes to effectively fill small cracks and crevices [78]. To generate a tribofilm, it is advantageous to have a substantial proportion of single-layered flakes [66]. These single flakes can also originate within the wear zone through mechanical exfoliation. To begin with a high concentration of single layers, one may choose to sonicate the material before using it as a lubricant in order to disperse and separate the sheet stacks. The mechanical properties of MXene films can be influenced by several factors, including the size and quality of MXene sheets, the orientation of these sheets within the films, the film thickness [65] and the adhesion of the film to a specific substrate [79]. Miao et al. conducted a comparative analysis of two different studies examining the impact of layer orientation on the tensile strength of films, as documented in [65]. The study involving highly oriented $Ti_3C_2T_x$ films reported an impressive tensile strength of up to 568 MPa [56]. In contrast, another group that investigated randomly stacked MXene layers observed a significantly lower tensile strength of only 40 MPa [80].

Determining which specific properties of a particular MXene affect its performance in tribological tests is a highly active research area. In this context, special attention should be paid to the previously discussed surface terminations. Key characteristics of MXenes are strongly influenced by their surface, as two-dimensional materials basically only consist of surface. This interaction is crucial for processes like ion intercalation, physical/chemical adsorption and chemical reactions [81], all of which have a profound influence on shaping the properties of MXenes.

Density functional theory (DFT) studies by Marquis et al. revealed that surface terminations play the dominant role in determining interlayer and substance adhesion properties [79]. They observed, that a higher concentration of -F terminations weakens the adhesion of the MXene layer to ferrous substrates. This weakening of adhesion may facilitate the removal of the lubricant during sliding conditions. On the other hand, -OH terminations were found to anchor the monolayer to the substrate through H-bond and electrostatic interactions. However, according to their calculations, this leads to a less efficient lubrication compared to the -F terminations. In this context another study by Tian et al. [82] yielded simmilar results. They conducted intercalation and functionalization of MXenes by introducing -OH groups through the use of ethylene glycol. This process facilitated the formation of tribofilms more effectively, leading to reduced shear strength and ultimately contributing to friction reduction [82]. Yang et al. analyzed the shear stress of three bilayer $Ti_3C_2T_x$ MXenes, terminated with O and/or OH, using molecular dynamic (MD) simulations with varying conditions of pressure and temperature. Their study explored the influence of temperature and surface termination on MXene shear stress behavior. O-terminated MXenes exhibited rising shear stress with temperature, except at 300 and 500 K,

where they showed the lowest shear stress. The shift towards higher shear stress in the O-terminated MXene was linked to interlayer bonding and due to the formation of Ti–O–Ti bridges [43]. The number of these bridges increased with higher pressures and temperatures. Incorporating OH terminations generally reduced shear stress. OH-terminated and heterostructure MXenes had similar shear stress, except at lower temperatures. Overall they demonstrated, that temperature and surface termination play pivotal roles in determining the interaction of MXenes layers.

The chemical reactivity of MXenes also offers benefits in tribology, particularly by facilitating the formation of a protective tribolayer [10]. In different environments and depending on the materials in contact, beneficial oxides can form [10], blended with MXenes that have experienced chemical and structural degradation. The positive effects of TiO_2 presence have been thoroughly investigated, as evidenced by studies like those referenced in [83, 84]. For instance research involving hybrid $TiO_2/Ti_3C_2T_x$ nanocomposites [83] and tri-phase MXene/TiO_2/MoS_2 systems [66] has shown reductions in the COF, linked to the presence of oxides. Interestingly, the reduction in friction observed with the oxides cannot be solely attributed to the formation of protective tribofilms. Yanbao et al. [85] conducted atomic force microscopy (AFM) analysis at 25 and 40 25 °C, which has also highlighted changes in adhesion, which correlate with the observed reduction in the COF. Their findings showed that $Ti_3C_2T_x$ MXenes exhibit reduced friction and adhesion forces at elevated temperatures, along with an increase in the oxidation degree. At both temperatures, the composition of $Ti_3C_2T_x$ MXene remained consistent, consisting of the elements C, Ti, and O. However, the X-ray photoelectron spectroscopy (XPS) analysis showed variations in the number of chemical bonds at these two temperatures. At 40 °C Ti-C bonds partially transformed into Ti-O bonds, increasing lattice oxygen content. Additionally, the replacement of some C atoms by O atoms resulted in a more compact Ti-O-Ti structure. This compactness leads to more evenly distributed electron clouds and lower polarization, reducing friction and adhesion at elevated temperatures [85].

However, it was observed that microscale particles of TiO_2 could also cause surface damage due to intense adhesion and abrasion [68, 86, 87]. Particularly, the formation of Ti-O-Ti bridges and the resulting interlayer bonding [43] of MXene sheets can lead to negative effects. During oxidation, MXenes undergo a transformation wherein they lose their characteristic layered structure and become TiO_2 particles. This change affects the low shear forces typically found between the layers, a key feature associated with their low COF. Consequently, the presence of titanium oxides is not always undesirable, but rather a question of concentration. Excessive amounts of significantly degraded and oxidized MXenes are unlikely to produce favorable tribological results.

2.3 Ionic Liquids

ILs are a class of organic salts known for their liquid state at typical room temperatures, hence often referred to as RTILs. These ILs consist of large organic cations paired with small inorganic or organic anions. ILs have remarkable versatility. The estimated number of combinations leading to characteristic properties in ILs exceeds

10^6 [88]. Therefore, they can be tailored to exhibit specific properties, leading to the development of task-specific ILs for various applications. However, characterizing ILs as a whole is challenging due to the considerable variations in their properties, depending on the specific cation and anion structures. For tribology, phosphate anions have shown favorable results [89]. Additionally, improved wear performance has been observed when the cation also incorporates a phosphate group [89]. Phosphate incorporation is a logical choice, given its established compatibility with zinc dialkyldithiophosphate (ZDDP) [90].

2.3.1 Ionic Liquids Synthesis

The ILs used in this study were synthesized by our colleagues in the chemistry group at TU Vienna. They are labeled IL1 and IL2 for a more comprehensible overview. The molecular names are Trioctyl(methyl)phosphonium dibutyl phosphate $[P_{8881}]$ $(BuO)_2PO_2^-$ for IL1 and Trioctyl(methyl)phosphonium dimethyl phosphate $[P_{8881}]$ $(MeO)_2PO_2^-$ for IL2. The difference between IL1 and IL2 is the chemical composition of the anions. While IL1 has dibutyl phthalate (DBP) anions, IL2 has dimethyl phthalate (DMP) anions.

Cations of IL1 and IL2

Anion of IL1   Anion of IL2
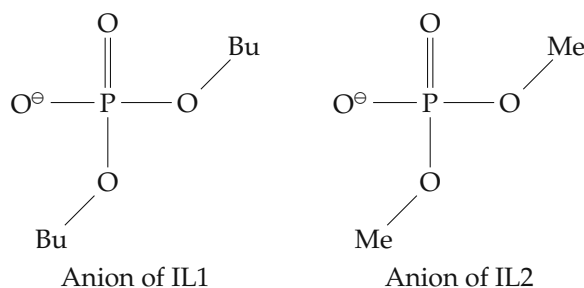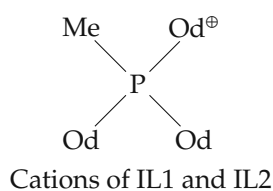
Synthesis of IL1: A round-bottom flask was charged with ($[P_{8881}]$ $(MeO)_2PO_2^-$) (1.0 eq.) and dibutyl phosphate (1.2 eq.) under argon atmosphere. Following this, triethylamine (1.4 eq.) was added dropwise under cooling with an ice bath. After the addition was complete, the reaction mixture was stirred for 20 minutes at 0 °C and overnight at room temperature. Distilled water was then infused into the mixture and it was stirred vigorously for 16h at room temperature. The mixture was transferred in a separatory funnel and was washed once with a mixture of triethylamine and distilled water (10:90 v/v) and four times with distilled water. Finally, the residual water was removed under vacuum (0.2 mbar, 95 °C). The desired IL $[P_{8881}]$ $(BuO)_2PO_2^-$ was obtained as a slightly yellowish, viscous liquid with a yield

of 97%.

<u>Synthesis of IL2:</u> Firstly, freshly distilled trioctylphosphine (1.0 eq.) was transferred to a round-bottom flask under argon atmosphere. Next, trimethyl phosphate (1.2 eq.) was added to the flask while constantly stirring. The temperature was increased stepwise to 140 °C and the mixture was stirred under an inert atmosphere for 72 hours. After completion of the reaction, the excess trimethyl phosphate was removed under vacuum (0.2 mbar, 95 °C). The desired product ($[P_{8881}]$ $(MeO)_2PO_2^-$) was obtained as orange, viscous liquid at a 98% yield.

2.3.2 Tribological Properties of Ionic Liquids

Key characteristics that make ILs promising candidates for new lubricants are thermal stability, low volatility and non-flammability. Especially in applications involving high loads and temperatures, ILs have shown remarkable potential. In 2001 the first study on the lubrication performance of ILs was published by Ye et al. [91]. This resulted in a significant surge of scientific interest for ILs as lubricants. The process through which an IL can enhance tribological properties is attributed, in part, to the adsorption of IL on the surface. Adsorbed ILs are in a more energetically favorable state, as ILs have a dipolar structure resulting in attracting Van der Waals forces between the steel sample and the IL. This adsorption leads to the formation of a protective layer that effectively maintains separation between the moving surfaces. Particularly higher loads can lead to the tribochemical generation of tribofilms [92], for instance from the fluorine-containing anions. This film provides a protective barrier for the surfaces in contact. It has been observed that ILs featuring longer chain lengths consistently display improved antiwear properties [93].

2.3.3 Compatibility of Ionic Liquids with Polymers

In tribology, rubber components play a crucial role in almost every application due to their ability to seal areas and retain lubricants. Given this essential function, evaluating the compatibility of these rubber components with ILs is vital. The interactions between the used ILs referred to as IL1 and IL2 and different types of polymers have not been extensively explored. This gap in research highlights the need for a deeper understanding of how these particular ILs affect various rubber materials. However, several other ILs have been analyzed in terms of their impact on polymers [94–96] and the results indicate that this topic needs thorough investigation before any application of IL lubricants in industrial applications is feasible.

An important aspect in understanding the interaction of ILs with polymers is their hydrogen-bonding behavior [97], because ILs can disrupt inter- and intramolecular hydrogen bonding in polymeric systems [94]. Currently, ILs are also being investigated for usage in depolymerization processes [94, 98]. Such research underscores the impacts of ILs on polymers. These negative and unwanted effects become pronounced when ILs are used in environments with rubber components, such as the MTM2 tribometer used for this work. The MTM system includes two rubber seals: an O-ring and a seal that encases the drive shaft for the disc. Both seals are constructed from Viton, a fluoropolymer elastomer.

Tomimatsu et al. investigated the degradation of various rubbers and resins when in contact with different ILs. The ILs they used include 1-ethyl-3-methylimidazolium diethyl phosphate, 1-ethyl-3-methylimidazolium tetrafluoroborate and others. The tested polymers are Fluoropolymers, Polypropylene, Polyvinyl Chloride, Silicone, Styrene Elastomer and Chloroprene. It was found that most rubbers and resins dissolve in the used ILs, except for silicone rubber [99]. A possible explanation for this is that silicone does not contain hydrogen as a major component in its backbone structure [100]. The study showed that ILs with phosphonium cations and acetate anions were more aggressive towards polymers [99]. The finding that the ILs in the study did not adversely affect silicone rubber presents a potential solution. Using ILs exclusively in systems with compatible seals could mitigate issues related to IL-induced degradation. An alternative approach is to synthesize ILs that have a low likelihood for hydrogen bonding, thereby minimizing their interaction with rubber seals. However, in the context of tribology, hydrogen bonding plays a crucial role in the formation of tribofilms [101], making it essential for achieving optimal tribological performance.

2.4 Glycerol

Glycerol is an odorless and colorless liquid that is readily available. It finds extensive use in pharmaceutical formulations due to its low toxicity and unique properties like water solubility and hygroscopicity (tendency to absorb moisture) [102]. Like other solvents, such as water, glycerol possesses the ability to dissolve various substances, including inorganic salts, acids, bases, enzymes and transition metal complexes [103]. It can also dissolve organic compounds that are typically poorly miscible in water. Additionally, non-volatility at normal atmospheric pressure and a high boiling point of 290°C [103] are properties of glycerol that are desirable in many applications, for instance, tribology. Glycerol is biodegradable and non-flammable, requiring no special handling precautions or storage considerations.

2.4.1 Tribological Properties of Glycerol

Glycerol, a highly viscous liquid, is known to generate friction coefficients in the range of 0.01 up to 0.5 or higher when applied to bearing steels in boundary lubrication [15, 104]. Its non-toxic and biodegradable properties render it an attractive option for applications with sensitivity to environmental sustainability and human health [103].

However, the widespread usage of glycerol in tribological applications has several drawbacks. For instance, in the EHL regions of the Stribeck curve, pure glycerol underperforms compared to conventional oils, as reported in [15]. Additionally, glycerol exhibits a relatively low Brugger-load-carrying capacity when compared to fully formulated mineral oils [57], as evidenced by conducted tests that yielded an average Brugger load-carrying capacity of 19.69 N/mm^2. Currently, glycerol qualifies for limited use as a non-toxic lubricant in selected applications and it is a common component of personal lubricants, but its suitability for industrial use may also be questioned due to its inherent hygroscopic properties. A distinguishing factor

between glycerol and ILs is pricing. Glycerol is a byproduct of biodiesel production from fats [105], which leads to a notably lower price.

Interestingly, in 2008 Matta et al. achieved a significant breakthrough by creating an environment with extremely low friction coefficients of less than 0.01 (superlubricity), on a macro scale by employing a glycerol/water mixture as a lubricant [106]. The mechanism responsible for this remarkable reduction in friction is therefore of substantial interest. They measured the friction of diamond like carbon (DLC) coated steel surfaces in boundary lubrication [106]. For their demonstration, they used a hydrogen-free type of DLC coating. It was discovered that hydroxylation (oxidation reaction of carbon–hydrogen) occurred on the DLC coated surface. This phenomenon was accelerated by contact pressure and high temperature [106]. The now OH-terminated contact surface facilitated the absorption of glycerol molecules and the formation of a tribofilm. The surface-bound molecules are prone to tribodegradation. According to Matta et al., this degradation leads to the release of acids and water in the contact area. Following this, the water might form a nanofilm on the surface [106], leading to an outstanding reduction in friction. The water-like lubrication mechanism observed can be attributed to the formation of a hydrogen bond network. This phenomenon was also reported by Bouchet et al. [107] when they worked with oleic acids, known to behave similarly to glycerol, under conditions comparable to those studied by Matta et al.

Moreover, MD simulations have unveiled that hydrogen atoms can function as polishing "brushes" between the sliding layers of crystalline FeOOH [108], resulting in reduced friction. The tribo-formation of FeOOH with glycerol initiates a distinctive polishing process, consequently establishing a self-sustained EHL regime until the fluid film becomes as thin as a few nanometers [108].

While it has been noted that DLC coatings alone can achieve superlubricity [109], achievements in superlubricity have also been reported with glycerol lubricated steel-on-steel contacts [110, 111]. Researchers at Tsinghua University in Beijing, for instance, have demonstrated that by adjusting the humidity around a glycerol-water mixture, the friction coefficient can be significantly reduced, achieving a stable superlubric state with coefficients as low as 0.006 at the macro-scale [111]. It's important to highlight that the mentioned results predominantly utilized a mixture of glycerol and water. Utilizing pure glycerol typically results in higher friction, making it a less favorable lubricant [106].

As discussed in Section 2.2.2, the interaction between solvents, particularly those with low viscosities and MXenes presents a challenge in maintaining a stable COF over time. This is in part caused by the formation of agglomerates. Specifically, aqueous MXene solutions exhibit pronounced fluctuations in this regard [10, 11]. Researchers have turned to innovative solutions such as an approach that involves the use of a glycerol solution. According to Shuang et al. glycerol, used as a lubricant and viscosity modifier, demonstrates remarkable synergy when combined with MXenes. They demonstrated that an aqueous MXene solution in combination with glycerol creates a lubrication system that reaches super-lubricity [11].

20

2.5 Environmental Considerations of MXenes, Glycerol and Ionic Liquids

Because 2D nanomaterials are relatively new, environmental aspects have not yet been analyzed for long-term effects. In tribological applications, all MXenes should be encapsulated in the lubricant or lubrication zone, preventing contact with the environment or airborne dispersion. However, as these novel substances are examined as potential environmentally friendly alternatives to traditional oils, this topic requires additional discussion.

In terms of biocompatibility, it's important to note that MXenes can pose a threat to microorganisms, either through direct penetration of cells or through the process of endocytosis [112]. Endocytosis is a cellular process where a cell engulfs and takes in particles or substances by enclosing them in a vesicle formed from its cell membrane. MXene particles within the 1-100 nm size range can be internalized by cells through this mechanism [112], potentially influencing cellular functions. Especially when the concentration of TiO_2 nanoparticles (oxidation of Ti_3C_2 MXenes) increased in the culture medium, the levels of reactive oxygen species (ROS) rise [113]. An increase in ROS is problematic for cells because elevated ROS levels can lead to oxidative stress, causing damage to cellular structures such as proteins, lipids and DNA. This cellular damage may disrupt normal cellular functions [114], subsequently leading to environmental problems. Additionally, the strong reduction activity associated with the reactive surface of $Ti_3C_2T_x$ disrupts the cell structure by reacting with the cytoplasm and molecules in the cell wall, resulting in the death of exposed microorganisms. As a conductive material, $Ti_3C_2T_x$ MXenes also act as a bridge on the insulating lipid bilayer, facilitating electron transfer from intracellular components to the external environment [114] and causing cell death. However, these phenomena are only observed at high concentrations of MXene exposure. When MXenes work as additives to lubricants, the main objective is to use a minimal quantity of the powder during application. Despite that, before introducing MXenes to any application with environmental contact further evaluation is necessary.

Another important consideration is the environmental burden resulting from the synthesis of MXenes. The current synthesis of MXenes is deemed environmentally unfriendly due to the utilization of HF and other potentially harmful chemicals. Efforts to reduce or eliminate the use of HF in MXene synthesis involve a mixture of LiF and highly concentrated HCl [50]. However, effectively treating the resulting residual fluoride waste to prevent its release into water resources remains a challenging task [50]. The MXenes produced through such a process maintain a multilayer form [50] with an accordion-like morphology and require additional delamination agents as described in Section 2.2.1. To alleviate these environmental concerns, bottom-up synthesis methods, such as CVD, offer promising alternatives without the need for toxic etchants [50].

Existing methods for synthesizing MXenes are also highly energy-consuming and exhibit low efficiency [115], necessitating the development of more sustainable approaches. It is reported that the primary factor influencing the environmental footprint of $Ti_3C_2T_x$ MXene synthesis is electricity consumption [115]. When assessing

the environmental impact of MXenes, it's crucial to distinguish between lab-scale production for research purposes and mass production for industrial use. Energy consumption significantly decreases when scaling up from producing a gram to a kilogram of MXene, with the energy ratio reported to be 1:10 [115]. This highlights the efficiency gains achievable through larger-scale production. The synthesis of the MAX phase consumes the majority of electricity due to the energy-intensive tube furnace required for this process. As a result, MAX phase production accounts for about 60% [115] of the total energy consumption. When compared to the production of copper and aluminum foil, the industrial-scale manufacturing of MXene is significantly more energy-demanding, requiring roughly 15 and 33 [115] times more energy, respectively. Currently, the synthesis of MAX phases and MXenes remains a lengthy, energy-intensive process and requires careful handling, posing significant obstacles to scalable production and environmental compatibility.

While glycerol is widely acknowledged as an environmentally friendly substance, classifying ILs in terms of environmental friendliness is more complex. Although they have low atmospheric diffusion, their high water solubility poses a threat to aquatic environments [116]. Furthermore, their stability and poor biodegradability [116] contribute to environmental concerns. These factors are strongly dependent on the specific anions and cations that make up the ILs. In many ILs, there is a notable trend where the longer and more branched the side chains on cations are, the more toxic the IL becomes [95]. For the ILs used in this work, there is very limited data available regarding biodegradability. However, IL1 and IL2 were produced through a solvent- and halide-free synthetic process. Notably, these ILs are also free from fluorine and chlorine. This also eliminates potential corrosion concerns when utilized as lubricants [17].

3   Materials and Methods

3.1   Software

In the course of conducting this thesis, several computational tools were employed to facilitate the visualization and analysis of data, the presentation of schematics and syntax refining.

For visualizing the accumulated data, MATLAB and TikZ (LaTeX) scripts were written and ImageJ was used for the analysis and visualization of microscopy images. To illustrate comprehensive sketches, OmniGraffle, a diagramming tool, was utilized. For polishing, rephrasing and translating certain sentences ChatGPT and DeepL were employed. The AI tools however were <u>not</u> used for literature review and gathering information.

3.2   Brugger Tester

As a first appraisal of the possible performance-improving capabilities, MXenes in combination with ILs might offer, the Brugger-Tester was used to evaluate the Brugger load-carrying capacity under room temperature and pure sliding conditions.

It operates within a boundary lubrication regime. This interaction occurs between a stationary cylinder made of AISI 52100 steel with a diameter of 18 mm, and a rotating ring constructed from AISI D6 steel and a diameter of 25 mm [57]. The lubricant is introduced at the contact area through syringe injection. The test setup complies with the DIN 51347-2 norm where the quantity of the lubricant is set to 8 ml [117], the force applied between the two cylinders is calibrated at 400 N (initial Hertzian contact pressure of 1.4 GPa [57]) and the sliding velocity of the cylinders is 1.2 m/s [117]. A great advantage of a Brugger test setup is that the experiments can be conducted in a relatively short time period, with a test duration of 30 seconds. After a lubricant-dependent running-in time period, metal-to-metal contact will occur and therefore simulate an oil starvation period. At the point where the two cylinders come into contact an elliptical wear mark forms. The performance of a lubricant is then evaluated by analyzing the wear mark area, that expands linearly [101] with time. Using an optical microscope, the Brugger load-carrying capacity in N/mm^2 is calculated with the measured diagonal a and b lengths of the area. Equation 10 is used to calculate the specific value for a wear scar with the normal force F_N of 400 N [117].

$$B = \frac{4 * 400}{a * b * \pi} \tag{10}$$

Figure 6 shows the alignment of the two cylinders. This results in a single contact point between the metals.
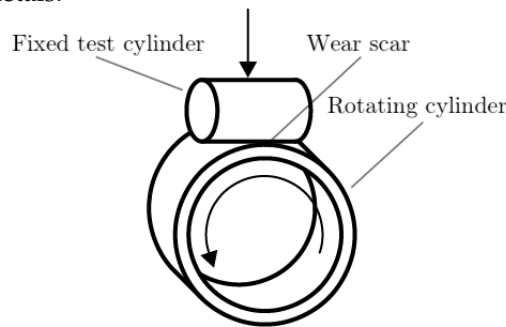
Figure 6: Schematic operating principle of a Brugger-Tester.

3.3 Mini Traction Machine

To validate the friction-improving capabilities in a ball-on-disc setup, we employed the MTM2 by PCS Instruments, which can perform fully automated traction mapping of lubricants under field conditions. The test rig enables evaluation of the friction coefficients at different slide-to-roll ratio (SRR) parameters with varying velocities, normal forces and temperatures. The term SRR describes the ratio between the entrainment and sliding speeds and it is defined by Equation 11. In a pure rolling scenario the SRR equals 0 % and with increasing sliding it can reach 200 % where the ball is fixed and therefore purely sliding over the disc.

$$SRR = \frac{U_{Disc} - U_{Ball}}{(U_{Disc} + U_{Ball})/2} \times 100 \tag{11}$$

The test specimens consist of a 19.05 mm (3/4") steel ball and a 46 mm diameter steel disc, but many other materials can be used. The steel ball and disc are both made of AISI 52100 steel and have a surface finish finer than 20 nmRa. The disc exhibits a hardness ranging from 720 to 780 Hv, while the ball has a hardness between 800 and 920 Hv. The operating principle of the machine is that a ball is loaded against the disc and both the ball and disc are driven independently, creating a mixed rolling and sliding contact. To achieve quantification of the frictional force between the ball and disc, a force transducer is employed. Additionally, the setup includes sensors to measure the applied load and the lubricant temperature.

The MTM2 can be enhanced through various extensions, two of which were applied in this study: the pot-filler and the spacer layer imaging (SLIM) setup described in Section 3.3.1. The inclusion of the pot-filler allows for measurements of only 10 ml of lubricant. Ordinarily, the MTM requires over 40 ml of lubricant to fully submerge the disc in the liquid. However, when working with expensive materials like MXenes, reducing the required volume becomes imperative. However, a notable drawback of the pot-filler is that it surrounds the temperature sensor as can be seen in Figure 8. Consequently, challenges arise, particularly at lower temperatures, due to the lack of test liquid flow in the area enveloping the sensor. This leads to prolonged response times for the sensor to detect lower temperatures.
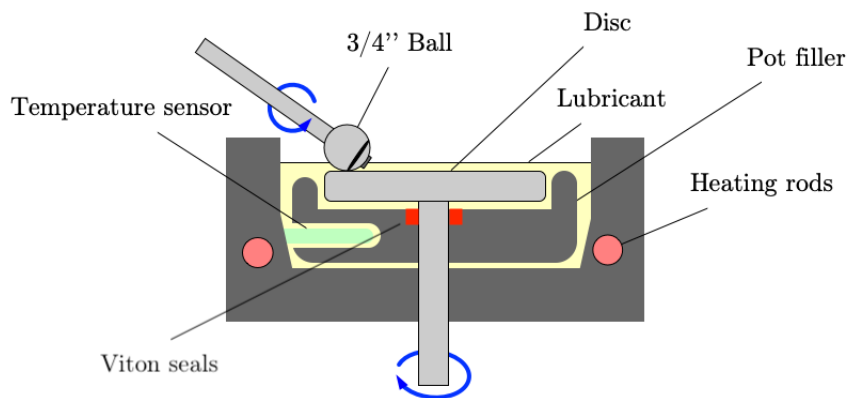
Figure 7: Schematic operating principle of the MTM2.

3.3.1 MTM SLIM Extention

The MTM2 can be upgraded with the 3D SLIM kit. This extension enables the analysis of tribofilms that might form during the measurement, by using optical interferometry. The SLIM system comes with a high-resolution RGB camera and a white light source that can be dimmed. SLIM measurements can be performed amidst the experiment, to progressively monitor film growth. At each SLIM step the steel ball is loaded at the glass surface with a preset force.
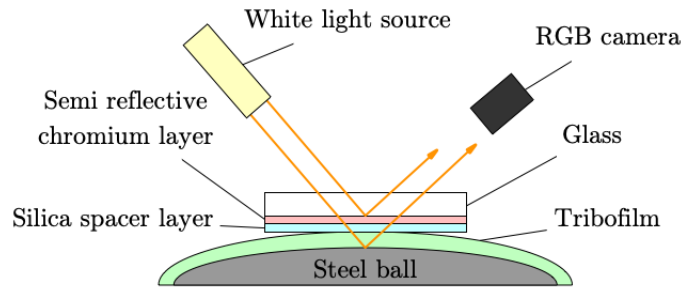
Figure 8: Schematic operating principle of the SLIM setup.

In the measurement process, a white light source is directed downward through a microscope onto the contact point between the steel ball and the coated glass disc. This contact point is illuminated, and the interaction of light with the different layers takes place. Some of the light is reflected off the chrome layer on the glass disc's surface, while another portion of light passes through the silica layer and any additional films that might be present. This light then reflects from the steel ball.

The recombination of these two light paths results in the formation of an interference image. This interference image is focused onto the imaging sensor of a RGB camera. The camera captures this image, and the digital frame grabber records it for analysis. The acquired camera image can then be processed using specialized control software, enabling the determination of a detailed film thickness map across the contact area.

In essence, the 3D-SLIM technique leverages optical principles to create and analyze interference patterns caused by the interaction of light with the various layers in the contact area. This approach enables the accurate quantification of tribofilm thicknesses within submicron ranges, offering valuable insights into the behavior and characteristics of these films during testing.

3.3.2   MTM Test Procedure

To conduct the MTM measurements, a dedicated test file, outlining the analysis parameters, was generated. Three consecutive runs of this test file were performed for each ball and disc set. This approach was chosen to assess the potential impact of tribofilm formation, ensure precision and consequently calculate average COF values. In the subsequent discussion of the gathered results, these three runs of the test file are regarded as one test. After each test, the ball and disc were changed and the temperature and the tested substance were altered.

To guarantee comparability with other tribological experiments the force in N was translated to the pressure in GPa using the correlation for a point contact provided by PCS.

Table 1 shows the test procedure that was carried out with the three tested liquids at two different temperatures. One test comprises three repetitions of conducting test runs at forces of 10, 20 and 30 N, with SRRs ranging from 5 to 120 % in 5 %

Lubricant	MX (wt.-%)	Temp (°C)	Force (N)	Pressure (GPa)	SRR (%)
IL1/IL2/GLY	0/0.25/1	30/80	10	0.35	5-120
			20	0.7	5-120
			30	1.05	5-120

Table 1: MTM Testmatrix.

increments. During the first run, the SLIM measurements were performed. To preserve the valuable SLIM lenses, a minimal number of measurements were taken. These lenses are highly sensitive and become scratched with each measurement, which renders them unusable after 10 to 50 measurements, depending on the tested lubricant and force applied to the lens.

3.4 Sample Preparation

For the Brugger tests samples with a concentration of 0.5 % were used. To enhance the understanding of the stability of the mixture, observations were made at time intervals of 15, 30, 60 and 120 minutes, as well as after 24 hours. The MXene powder in the IL solutions remained well dispersed, even after 24 hours. But with glycerol sedimentation occurred at a faster rate. The results of this experiment are shown in Figure 11. The settling of lubricant additives is undesirable because it reduces the intended enhancing effects of the lubricant when machinery is restarted following a period of inactivity. This phenomenon may increase the COF, as the agglomeration of particles can undermine the friction-reducing capabilities of MXenes [66]. The agglomeration process notably decreases the surface area available for interaction with the contact surfaces, thus impairing the ability of the material to establish protective layers, or tribofilms [10]. When MXene flakes are well-dispersed, they can readily infiltrate microscopic wear scars and surface asperities, forming a barrier that mitigates wear [10]. However, when agglomerated, these particles become excessively large to efficiently reach and protect these critical areas, leading to diminished protective effects.

The three MTM samples (Glycerol, IL1 and IL2) were all dispersed following a consistent procedure to guarantee comparability of the individual results. To calculate the corresponding weight percentage Equation 12 was applied.

$$wt. - \% = \frac{w_{MXenes}}{w_{total}} \times 100 \tag{12}$$

The added amount of MXenes is displayed in Table 2. After adding the powder to the base lubricant the solution was mixed with a magnetic stirrer for ten minutes. Next, the mixtures were sonicated in an ice bath for two hours each. Right before pouring the lubricants into the MTM, they were mixed with the magnetic stirrer once again for five minutes, to ensure a homogeneous blend.

Lubricant (12 ml)	Concentration	Mxenes in mg
Glycerol	1 wt.-%	151.86
	0.25 wt.-%	37.68
IL1	1 wt.-%	110.59
	0.25 wt.-%	27.44
IL2	1 wt.-%	117.24
	0.25 wt.-%	29.09

Table 2: Composition of the samples.

After plotting and analyzing the MTM data, the decision was made to further investigate the surfaces and explore the potential formation of a tribofilm. However, given that the samples initially used for the MTM experiments were several months old, this analysis wouldn't be meaningful due to the previously discussed oxidation of MXenes. Consequently, new tests were conducted. The discs used for TEM analysis were vacuum-sealed immediately after extraction from the MTM. Subsequently, these sealed bags were stored in a desiccator and analyzed within one week.

In this research, an experiment featuring a glycerol-water-MXene blend was conducted to obtain deeper insights and ensure comparability with other studies. A distinct sample preparation method, closely mirroring that used by Yi et al. [11], was adopted. For this test, deionized water was used in conjunction with glycerol. The glycerol-to-deionized water ratio was 1:5 and a 2 % concentration of MXenes was added. Notably, the MXenes underwent sonication in deionized water before the introduction of glycerol. Throughout the five-hour sonication process, no ice bath was utilized, resulting in the temperature of the sonicated lubricant reaching 73 °C. Furthermore, adjustments were made to the MTM test matrix to explore potential timing (run-in period) impacts on the investigation. In this additional test, the SRR was set to 200 %, resulting in a stationary ball. The disc's rotation speed and applied force were fixed at 200 mm/s and 2N, respectively and maintained for five hours without parameter alterations. Subsequently, over the next three hours, the speed and force were incrementally increased to 1000 mm/s and 5 N.

3.5 Lamella preparation for TEM analysis

The preparation of the lamella, intended for TEM assessment, involved the use of the ThermoFisher Scios II. Using scanning electron microscopy (SEM), the surface was scanned with the intention of identifying tribolayer formations. Special attention was given to samples containing MXenes, focusing on selecting surfaces where titanium was detected. The rationale behind choosing these particular surfaces stemmed from the inconsistency of MXene tribofilms [11], particularly as concentration is estimated to be higher in the deeper grooves of the wear scar.

In Figure 9 a SEM image of the wear scar surface can be seen. For the focused ion beam (FIB) cuts, an area characterized by deep grooves was specifically chosen. During this lamella preparation gallium ions were employed for the cuts to precisely

mill and manipulate the sample at the nanoscale for in-depth TEM analysis.
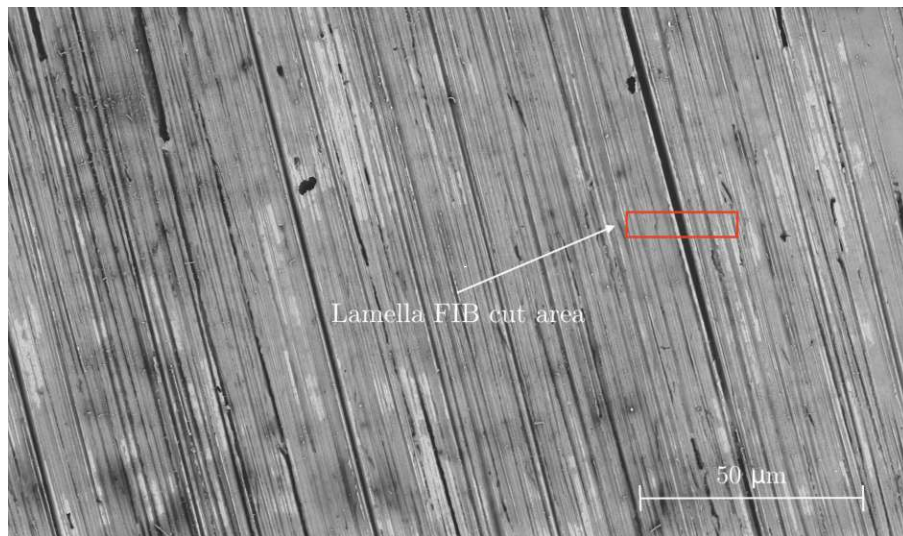
Figure 9: SEM image of the wear scar surface.

Figure 10 displays the lamella at two stages: first, after being cut from the disc and welded onto the sample holder and second, after the thinning procedure, involving the sequential removal of material layers. The protective wolfram layer is visible in both images atop the surface.
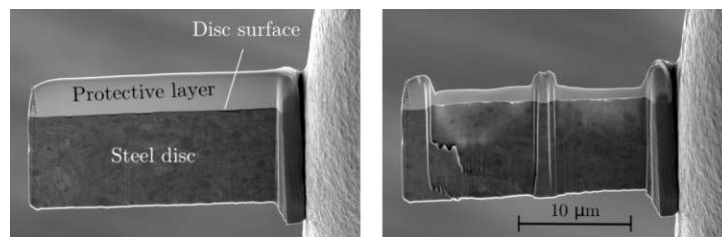
Figure 10: SEM images depicting a lamella both before (left) and after the milling process (right).

4 Results and Discussion

4.1 Assessment of Dispersion Stability

As an initial assessment, the dispersion stability was evaluated. As illustrated in Figure 11, using polar ILs or glycerol as the dispersion medium significantly mitigates issues of sedimentation and agglomeration. We observed that notable sedimentation in our samples occurred only after exceeding 48 hours.

The intrinsic ionic nature of hydrophobic ILs leads to strong electrostatic interactions with polar MXenes, despite their hydrophobicity [118]. MXenes have reactive -OH groups as their surface terminations. These can interact with negatively charged ions, forming charge-induced hydrogen bonds. This interaction between the IL's anion and MXenes polar O-H bonds enhances the overall interaction between ILs and MXenes, resulting in improved dispersibility [57]. This delayed sedimentation can

also be attributed to the higher viscosities and the thus increased kinetic dispersion
stability of the ILs and glycerol [119].

Figure 11: Dispersion after sonication/stirring (left) and after 24
hours (right)

4.2 Evaluation of the Brugger Load Carrying Capacity

The efficiency of ILs and glycerol mixed with MXenes was initially assessed under
high-pressure conditions using the Brugger tester. The Brugger-Tester operates in
the boundary lubrication regime, where significant metal-to-metal contact occurs,
leading to considerable abrasive and adhesive wear [57] on the test cylinders. The
analysis of the wear scar was achieved by using the VK-X1000 laser microscope
built by Keyence to measure the width and length of the wear scar and substitut-
ing these values into the Brugger load-carrying capacity formula. This evaluation
aimed to determine whether these combinations could exhibit synergistic effects and
compatibility [57].

The test results in Figure 12 demonstrate, that IL-MXene mixtures have enhanced
lubricating capabilities. The added MXenes lead to an increased Brugger load carry-
ing capacity of 26 % for IL1, 6 % for IL2 and 7 % for glycerol [57]. It was found [57],
that the Brugger load-carrying capacity of pure IL1 and IL2 does already outperform
non-additivated FVA2 base oils and fully formulated and commercially available
turbine oils that were tested under identical conditions [57].

Our team has previously investigated these ILs, utilizing a concentration of 5 % IL
in combination with standard, non-additivated FVA2 base oils [17]. In comparison
to the IL-additivated base oils the pure ILs have marginally enhanced performance
attributed to the higher viscosity, which supports the formation of a thicker lubricant
film and the increased presence of phosphorous-based compounds, which contribute
to the development of tribofilms [17]. An observation in this regard is the superior
performance of IL1 compared to IL2. This outcome diverges from the findings
reported by Faruck et al. [17], where IL2 exhibited better performance in combination
with PAO based oils. As already mentioned the MXenes further improved the
load carrying capacity. This improvement can be attributed to the incorporation of
MXenes into the tribofilm and a resulting increase in durability of this protective film
[17, 57]. Faruck et al. concluded that the reduced viscosity of IL2 facilitated a more
efficient integration of MXenes into the IL/MXene tribolayer [17]. Thus effectively
minimizing wear by ensuring a consistent presence of MXenes at the tribological
interface. Nonetheless, when testing the pure ILs we observed that smaller wear scar
dimensions with IL1, indicating greater wear resistance compared to IL2.

Our results therefore contradict such previous studies [17, 120] with these ILs showing
better performance for anions having shorter alkyl chain lengths due to quicker
reactions of these anions with the surface leading to the formation of tribolayers

29

[120]. However these studies were performed under lower loads and with the ILs as an additive instead of a pure lubricant. Consequently, we anticipated that the lower reactivity of IL1 is advantageous under the high applied load in our study, thus promoting a slower degradation of the IL and a longer lifetime of the tribofilm. Additionally, it has been shown that the thickness and compactness of the formed IL-based tribolayers mainly depend on the alkyl chain lengths of the ions [57].[43,45,46] Therefore, we concluded that IL1 can form a thicker and more compact tribolayer on the steel surface, which protects the underlying surface from wear and results in a higher load-carrying capacity [57]. This is supported by the fact that the viscosity of IL2 is significantly lower than that of IL1, as demonstrated in the following section. This increased viscosity is then responsible for a thicker lubricant film with IL1.

Our findings diverge from earlier research [17, 120] indicating superior performance of ILs with shorter alkyl chain anions, attributed to their faster surface reactions promoting tribolayer formation [120]. These prior studies, however, were conducted under different conditions, using ILs as additives rather than standalone lubricants. In contrast, our experiments, performed under higher loads with ILs serving as the sole lubricant, suggest that the reduced reactivity of IL1 may actually be beneficial [57]. This slower reactivity likely contributes to a decreased degradation rate of the IL1 tribofilm, extending its operational lifespan and wear resistance [57]. Moreover, research has established that the thickness and density of IL-derived tribolayers are largely influenced by the alkyl chain lengths of the ions [57, 121, 122]. As a result, we anticipated that IL1 to create a denser, more robust tribolayer, offering enhanced protection against wear and superior load-bearing capabilities [57]. This hypothesis is reinforced by the observed viscosity differences. IL2's lower viscosity compared to IL1 leads to a thinner lubricant film, whereas IL1's higher viscosity facilitates the formation of a thicker lubricant film, further corroborating our conclusions. The results from the Brugger analysis however give only a rough estimate of the capabilities the substances have to offer. Therefore further investigation with the MTM system is carried out.
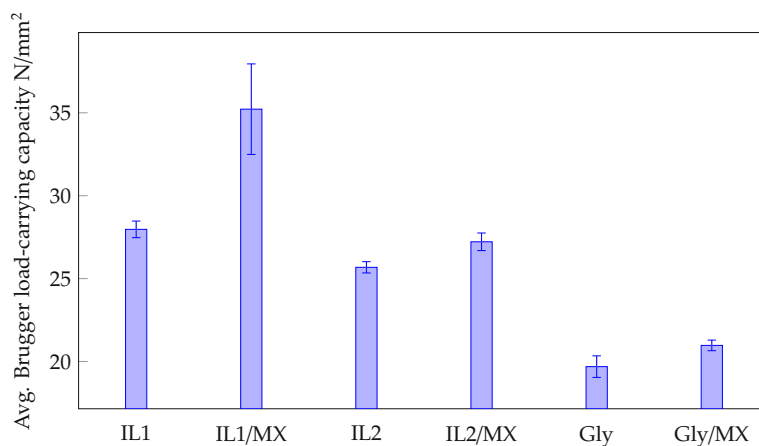
Figure 12: Brugger test results of the ionic liquids and glycerol

4.3 Examination of Rheological Behavior

As a baseline characterization, the viscosities of the three tested liquids were evaluated at a temperature range from 25 to 80 °C using an Anton Paar MCR 300 rheometer, as seen in Figure 13. The results of the viscosity measurements indicate that with the added percentages of MXenes the rheological properties do not change.
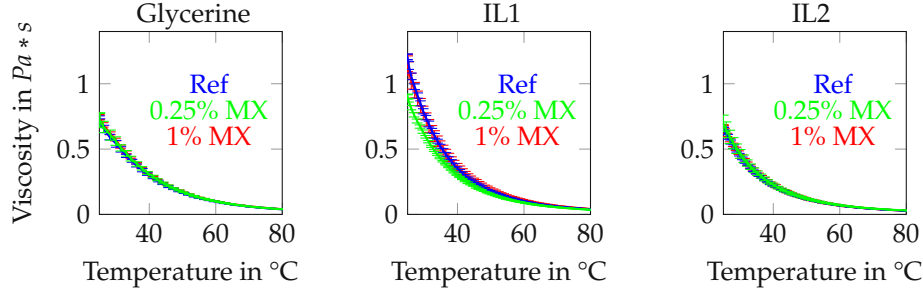
Figure 13: Average viscosity of three results at each concentration, measured with the Anton Paar MCR 300 rheometer.

This observation is consistent with the findings reported by Boidi et al. and suggests that MXene nanosheets primarily enhance interfacial properties, including the formation of tribofilms, leading to a notable reduction in friction, rather than significantly altering the rheological properties of the liquid [12]. The rheological tests were carried out with a gap distance of 0.05 mm. It is essential to consider that while the gap in the rheometer is indeed small, it remains significantly larger than what is typically observed within the tribological interface itself. This distinction is critical because it suggests that the conditions and pressures within this gap differ from those at the actual contact points where tribological interactions occur. Consequently, the dynamics and lubrication mechanisms within this larger gap do not accurately reflect the behaviors and forces at play in the more confined spaces of direct tribological contact.

Given, that the MTM has a fully submerged contact zone, we will employ the Hamrock-Dowson model as presented in Equation 3 to estimate the central and minimum gap distances of the ball and disc under EHL conditions.

$$H_{central} = 2.69 \cdot G^{0.53} \cdot U^{0.67} \cdot W^{-0.067} \left(1 - 0.61 e^{-0.73k}\right)$$

$$H_{min} = 3.63 \cdot G^{0.49} \cdot U^{0.68} \cdot W^{-0.073} \left(1 - e^{-0.68k}\right)$$

To apply the formula from Hamrock and Dowson introduced in Section 2.1.3 we must first determine the radii of the contact area using Hertzian contact analysis. Considering the setup of the MTM, which involves a ball-on-disc arrangement, we encounter a circular contact area. Therefore the radius of the contact circle, denoted as a, is determined through the application of Equation 13. For the ball-on-disc setup in the MTM analysis, the ball and the disc are characterized by the following parameters: both the ball and the disc are AISI 52100 steel and have an elasticity

modulus (E) of 210 GPa and a Poisson ratio (v) of 0.3. The ball has a radius (R) of 9.525 mm and a force (F) of 10 N is applied. These parameters will be utilized in the calculation of the contact radius a.

$$a = \sqrt[3]{\frac{3F}{8} \cdot \frac{R}{E'}} = \sqrt[3]{\frac{3F}{8} \cdot \frac{\frac{1-v_1^2}{E_1} + \frac{1-v_2^2}{E_2}}{\frac{1}{R_1} + \frac{1}{R_2}}} = 85.23 \mu m \tag{13}$$

Subsequently, the parameters G, U, W, and k are calculated using the following formulas with temperature-dependent constants, evaluated at 30 °C. The contact radius a is equal to R_X and R_Y.

$$k \approx 1.03 \left(\frac{R_Y}{R_X}\right)^{0.64} \qquad G = \alpha_p E' \qquad U = \frac{\eta u}{E' R_X} \qquad W = \frac{F}{E' R_X^2}$$

In particular, the calculation of the coefficient G presents a challenge due to the inclusion of the pressure-viscosity coefficient, a parameter that was not determined for the ILs utilized in our experiments. However, for glycerol, this coefficient is well-established, with a value of 5.9 GPa^{-1}, as documented in the literature [123]. The literature also indicates that the pressure-viscosity coefficients for the limited selection of ILs studied fall within the range of 8 to 12 GPa^{-1} [124–127]. Consequently, the decision was made to adopt an average value of 10 GPa^{-1} and to reflect errors corresponding to the observed deviations from this average. For calculating the pressure-viscosity coefficient, the dynamic viscosity values recorded at 30°C using the rheometer at TU Wien are employed. Our measurements and the literature indicates that the viscosity of ILs, particularly IL1, exhibits a significant sensitivity to both temperature and pressure [128]. This variation in IL viscosity can influence both frictional behavior and the dispersion of nanoparticles within the IL [129]. It is important to mention that the pressure-viscosity properties of lubricants containing MXenes were not evaluated in this work, resulting in no specific calculations related to these parameters. Anticipated alterations in the pressure-viscosity coefficient for the MXene-lubricant mixtures are expected to be substantial. Consequently, this variation may contribute to observed discrepancies in the COF measurements obtained using the MTM.

As depicted in Figure 14, the gap sizes in tribological contacts are over two orders of magnitude smaller, ranging from 200 to 2250 nm. This is in contrast to the rheological analysis, which employs substantially larger gaps, approximately 50000 nm in our experiments. Such larger gaps facilitate the examination of fluid bulk properties, but they do not capture the effects of surface-to-surface interactions and the influence of the MXenes. Moreover, in rheological analyses, the contact zone is subjected to ambient pressure conditions, contrasting sharply with our findings, where the maximum contact pressure calculated reaches 0.66 GPa.
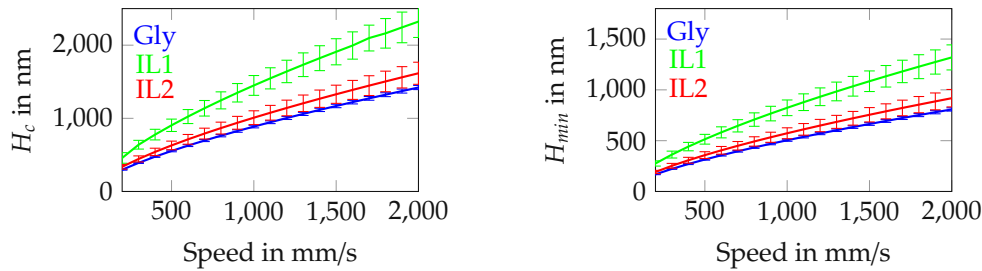
Figure 14: Central (H_c) and minimum (H_{min}) film thickness of Glycerol, IL1 and IL2 as calculated employing the Hamrock and Dowson formula, based on viscosity measurements at 30°C and an applied load of 10 N. The analysis incorporates an average pressure-viscosity coefficient of 10 GPa^{-1} for the ILs and 5.9 GPa^{-1} for glycerol). This plot highlights the differences in tribological gap distances in comparison to the gap distance of 50000 nm used in the rheometer.

4.4 Impact of Ionic Liquids on Polymer Durability

An unexpected finding during our experiments was the rapid degradation of rubber components, specifically the rubber shaft seal and O-ring in the MTM2 apparatus. The degradation of the seal material intensified notably with the samples that were tested with a higher temperature of 80 °C. This observation raises concerns about the broader applicability and material compatibility of ILs in tribological contexts.

Rubber degradation in the presence of ILs is a phenomenon that has yet to be thoroughly investigated about its impact on the long-term reliability and performance of tribological systems. The integrity of rubber components is essential for the proper functioning of many mechanical systems. Thus, degradation can lead to significant operational challenges. To evaluate the impact of ILs on rubber materials, a long-term immersion test was performed with IL2. For this the circular seal was cut into five pieces, and fully submerged in the IL2 for one month at room temperature. The results, depicted in Figure 15 show the pronounced deterioration of the seal. In addition to the undesirable deterioration of the seals, the presence of degraded rubber particles within the tribological system could notably impact the accuracy of measurements. At higher temperatures, these dislodged particles were visibly circulating within the lubricant reservoir. This can also be observed in Figure 15.

Figure 15: Rubber seal after one month in IL2.

According to PCS (the supplier of the MTM), both seals are constructed from Viton, a type of fluoropolymer elastomer [130]. Viton contains copolymers of hexafluoropropylene and vinylidene fluoride, along with minor quantities of additional compounds to enhance their properties, the exact composition and concentration of these

additives remain undisclosed and vary among suppliers [131]. This degrading effect on fluorinated polymers was already observed by other groups [130]. They demonstrated that incorporating ILs into various polymers resulted in reduced thermal stability, suggesting interactions between the IL's and the CH_2-CF_2 groups in the fluorinated matrix. Additionally, it has been determined that the composite material's thermal stability diminishes as the cation chain length increases [130].

This finding underscores the necessity for understanding the interactions between ILs and polymers in order to find compatible ILs in the future. The degradation of rubber by ILs suggests that while ILs may offer promising tribological properties, their compatibility with polymers is concerning.

4.5 Investigation of the Tribological Properties with the MTM

4.5.1 Analysis of Stribeck Curves Obtained from MTM Experiments

Upon the initial application of the ILs to the MTM steel disc, we observed that the ILs, though generally hydrophobic, displayed good wettability on the steel surface. Like all metals, the used steel is also hydrophilic, since metallic ions will dissolve in a polar solvent, such as water [132]. The ILs exhibit adherence to the metal surface as a result of their low interfacial energy [133]. This reduced interfacial energy implies that less energy is needed for the ILs to attach to the steel surface, resulting in behavior that is effectively hydrophilic [133].

Figure 16 presents the complete dataset for IL1 at 10 N and 30 °C. It is evident that the COF decreases with each sequence of SRRs, particularly in regions with increased sliding (higher SRR). The observed enhancement in performance might be attributed to the formation of an amorphous $P-O$ based tribofilm, as previously identified by our group [17].

Utilizing the Hamrock-Dowson formula, we determined a minimum film thickness of IL1 at 10N and the lowest speed (100 mm/s) to be 172 nm. Given that both the ball and disc initially present a surface finish of 20 nm, we have an averaged surface roughness of 20 nm. Through Equation 14, where H_{min} signifies the calculated minimum film thickness and S_a the averaged surface roughness of the interacting surfaces, we calculate the λ-coefficient.

$$\lambda = \frac{H_{min}}{S_a} = \frac{172\,\text{nm}}{20\,\text{nm}} = 8.6 \qquad (14)$$

This calculation predicts that the entire measurements at 10 N will occur within the hydrodynamic regime ($\lambda > 3$) as higher speeds will lead to an increase of H_{min} and therefore even higher λ-parameters. Figure 16 verifies the result of the calculation that demonstrated that the COF will be the hydrodynamic regime. These plots were selected as they provide additional insights into single measurements, that may not be evident in the plots and heatmaps that will follow. Numerous research studies have demonstrated the ability of ILs to achieve exceptionally low friction in lubricated contact pairs [14, 91, 129]. Consistently, in our investigation, we also observed low friction coefficients across all tested lubricants, whether with or without MXenes. In

Figure 16, it is evident that as the sliding increases (higher SRR), the performance of the second and third runs also improves.
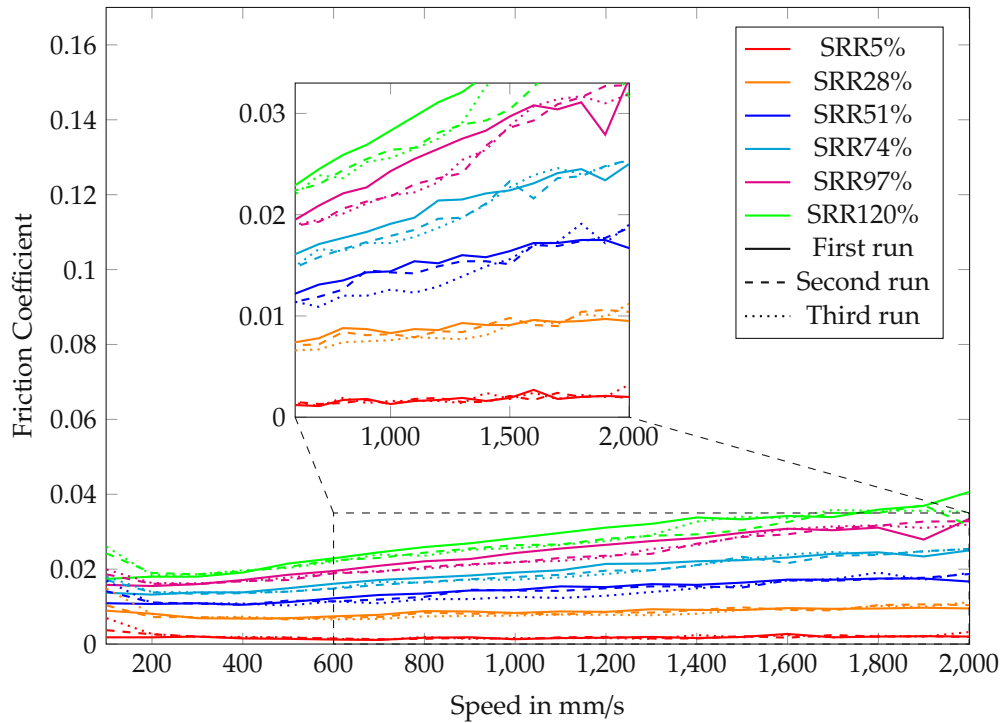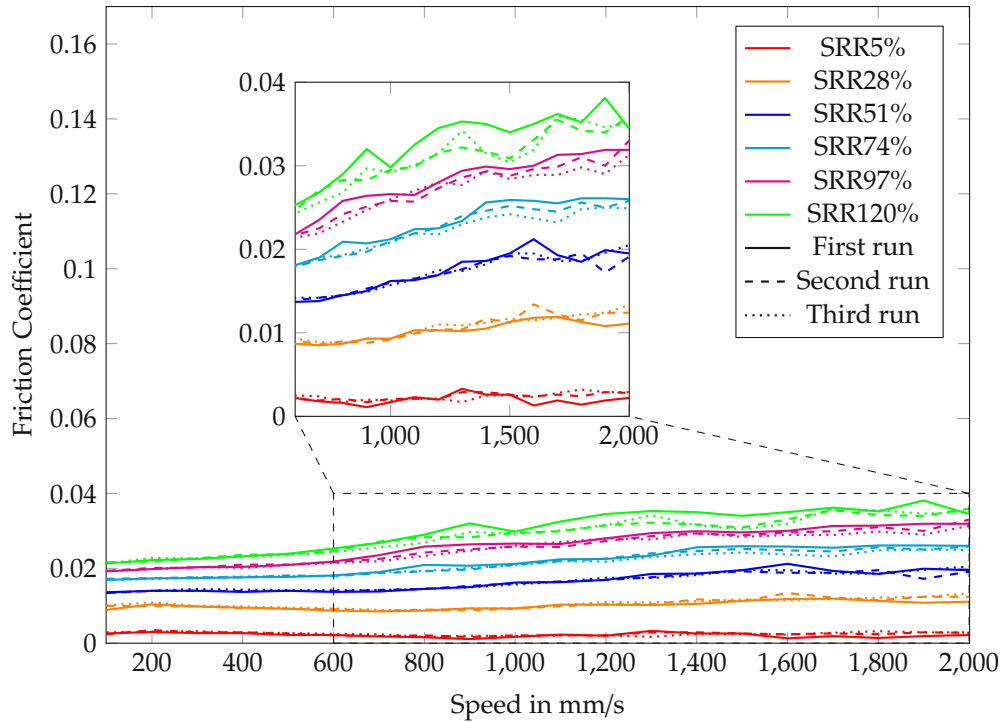

Figure 16: Stribeck curves for pure IL1 at 10 N and 30°C, with SRRs ranging from 5% to 120%. The curves were collected in three sequences, with each sequence covering the entire SRR range. The entire curve falls within the hydrodynamic regime, aligning with numerical predictions.

In Figure 17, measurements with 1 wt.-% MXenes are presented, where the COF also remains within the hydrodynamic regime throughout, leading to only minimal differences in performance. This minimal impact cannot be attributed to MXenes known effectiveness, that is contingent upon direct surface contact, through which they modify the interfacial properties of the surface [10]. Rheological tests have shown that the viscosity remains relatively unchanged, but these viscosity tests were conducted at ambient pressure. It's important to recognize that tribological contacts, particularly under high loads as in this work, can generate significant pressures [125], potentially altering viscosity. Previous observations have indicated that nanomaterials in a lubricant can significantly affect the pressure-viscosity coefficient [134]. Thus, we hypothesize that the presence of MXene could have indeed influenced the pressure-viscosity coefficient, thereby affecting the COF in the hydrodynamic regime. However, the verification of this hypothesis was beyond our capabilities, as we lacked the means to measure the pressure-viscosity coefficient directly.
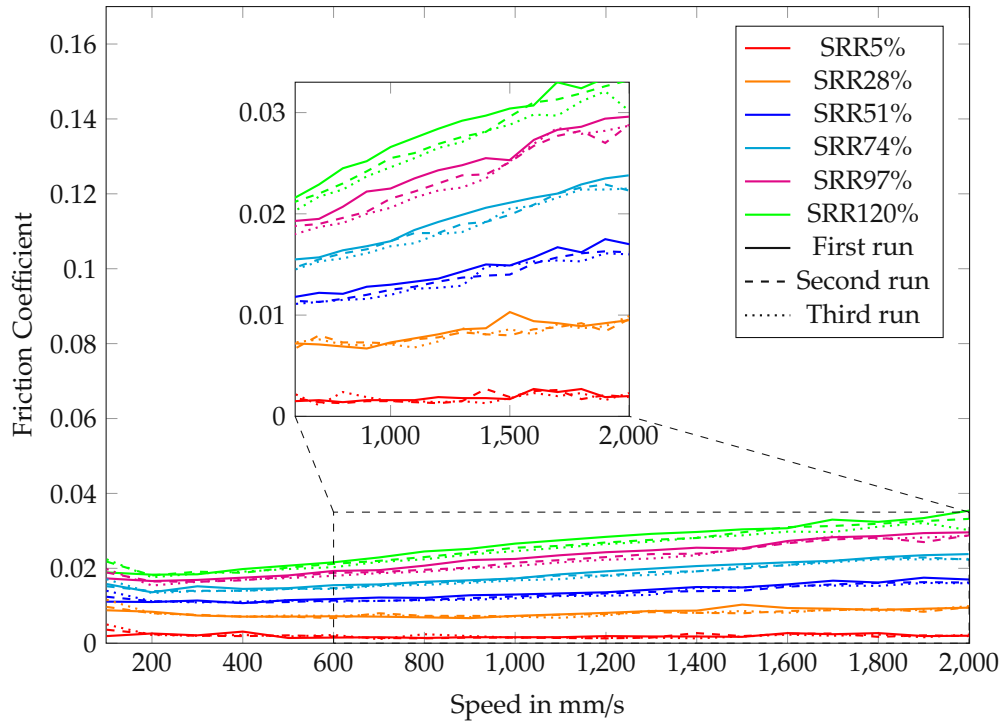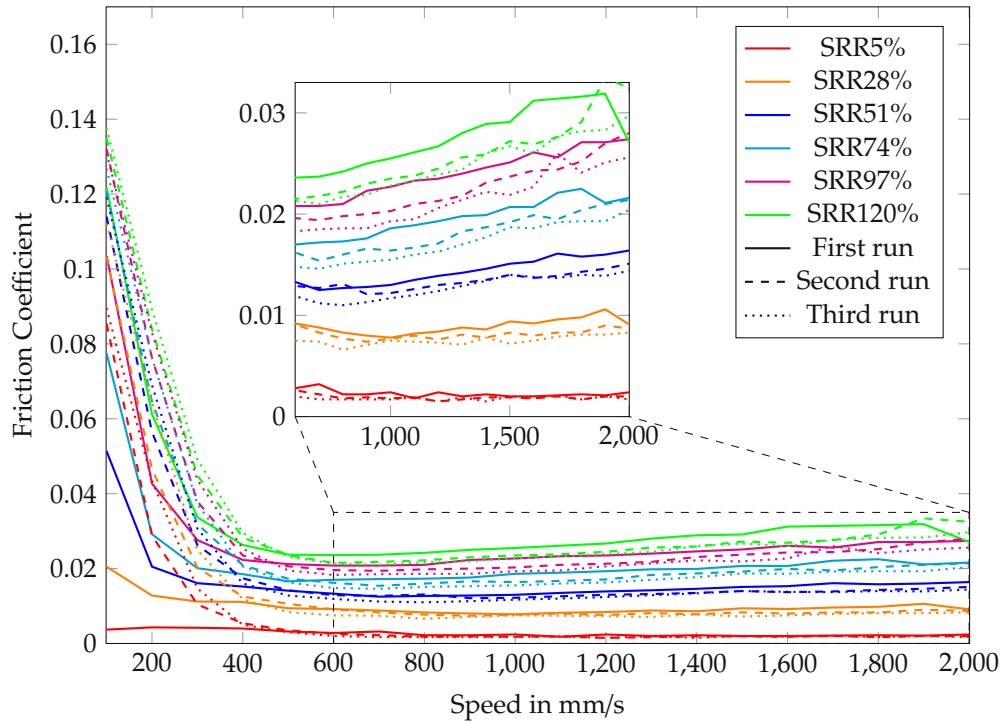
Figure 17: Stribeck curves for IL1 with 1% MXenes at 10 N and 30°C, with SRRs ranging from 5% to 120%. The curves were collected in three sequences, with each sequence covering the entire SRR spectrum. The portion of the plot corresponding to lower speeds initiates in the mixed lubrication regime.

Utilizing the Hamrock-Dowson formula, we determined a minimum film thickness of IL2 at 10N and the lowest speed (100 mm/s) to be 119.74 nm. Through Equation 14, where $H_{\min}$ signifies the calculated minimum film thickness and S_a the averaged surface roughness (20 nm) of the interacting surfaces, we calculate the λ-coefficient. Applying Equation 14 results in a λ-parameter of 5.99, indicating that measurements at 10 N will also fall within the hydrodynamic regime, as defined by $\lambda > 3$. Figure 18 presents the complete dataset from the 10 N test of IL2 at 30 °C, verifying the calculation by showing that the COF remains within the hydrodynamic regime throughout the experiment.
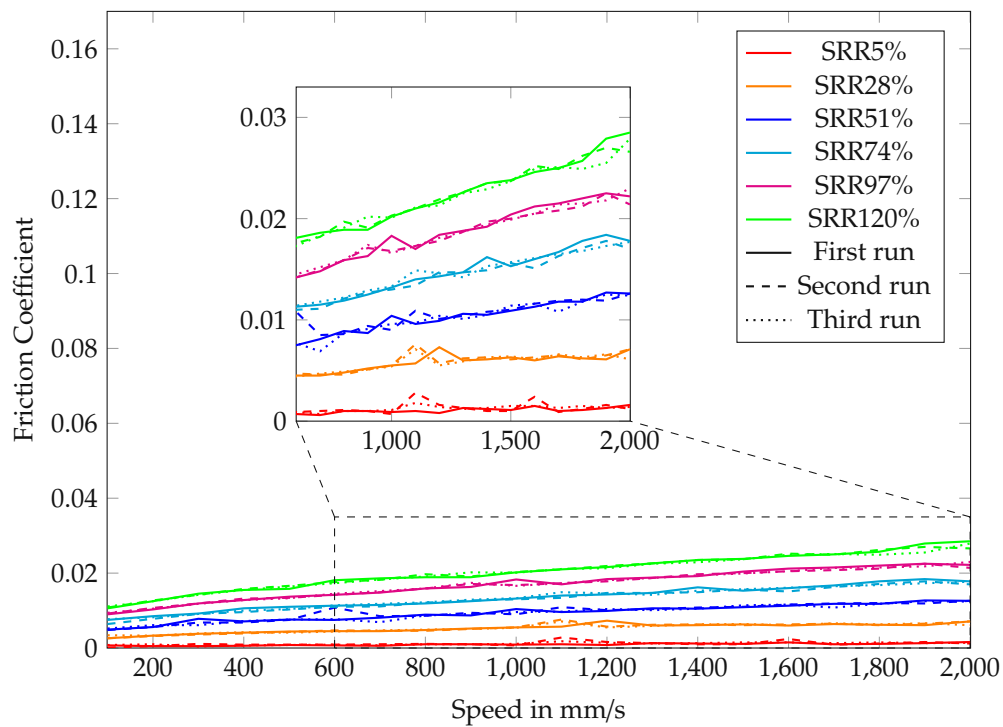
Figure 18: Stribeck curves for pure IL2 at 10 N and 30°C, with SRRs ranging from 5% to 120%. The curves were collected in three sequences, with each sequence covering the entire SRR range. The entire curve falls within the hydrodynamic regime, aligning with numerical predictions.

Figure 19 illustrates the same test of IL2 with 1 wt.-% of MXenes. Interestingly, this measurement showed that the MXenes had a negative impact on the COF at lower speeds where the COF falls within the mixed lubrication regime of the Stribeck curve. Similar to IL1 it can also be observed in Figure 19 that the second and third runs outperform the first run in the hydrodynamic region. However, as the number of repetitions of the same test increases, the COF tends to increasingly reside within the mixed lubrication regime. This trend may be attributed to an increase in surface roughness, as the initial measurements already led to solid-body contact, as evidenced by the COF residing in the mixed lubrication regime. The question that remains is what leads to solid-body contact when the MXenes were added.

MXenes are non-abrasive [65], thereby ruling out the possibility of them being the cause for an increase in surface roughness. Upon examining the minimum film thickness values calculated in the preceding section, it becomes evident that the film thickness of IL2 at the lowest speed falls within a range of approximately 120 nm, placing it in a similar size regime as MXenes flakes (lateral size). Our previous analysis (Figure 5) has demonstrated that the MXenes used for this work consist of multilayer stacks that fall within a size range of several μm. Consequently, there exists the potential for the MXenes to interfere with the buildup of a continuous lubricant film in the contact zone. An inconsistent lubricant film subsequently leads to a decrease in the lambda parameter and solid-solid contact.

Another aspect to consider, although less plausible given the low concentrations

(0.25 wt.-% and 1 wt.-%), is the potential existence of MXene agglomerates. These agglomerates could contribute to additional disturbances in the film buildup process. Previous research has highlighted that MXenes, when inadequately dispersed within the base lubricant, can result in diminished performance [10, 66]. Therefore, it is evident that the quality of dispersion plays a crucial role in determining the performance of MXenes. It is possible, that the two hours of sonication that were done before the test were not properly dispersing the MXenes, as sonicating in highly viscous liquids has shown to be less effective [64].

The described effect at low speeds, where the COF is in the mixed lubrication regime with MXenes, and in the hydrodynamic regime without MXenes, was not detected in the measurement for IL1. Calculations for IL1 resulted in the highest minimum film thickness among the tested lubricants. This suggests that the separation distance was sufficiently large to prevent the potential negative impacts of MXenes. Despite this, as indicated by Figure 14, the film thickness of IL1 was still relatively close to that of the other lubricants tested and in the range of the MXenes size. A further explanation for this anomaly could be, that the anion in IL1 interacts more effectively with the MXenes O−H bond, as suggested by the studies referenced [57, 135]. This enhanced interaction possibly leads to better bonding with the MXenes in IL1 compared to IL2, thereby preventing the MXenes from adversely affecting film buildup. These results imply that in terms of synergizing with MXenes, IL1 surpasses the performance of the other liquids tested.
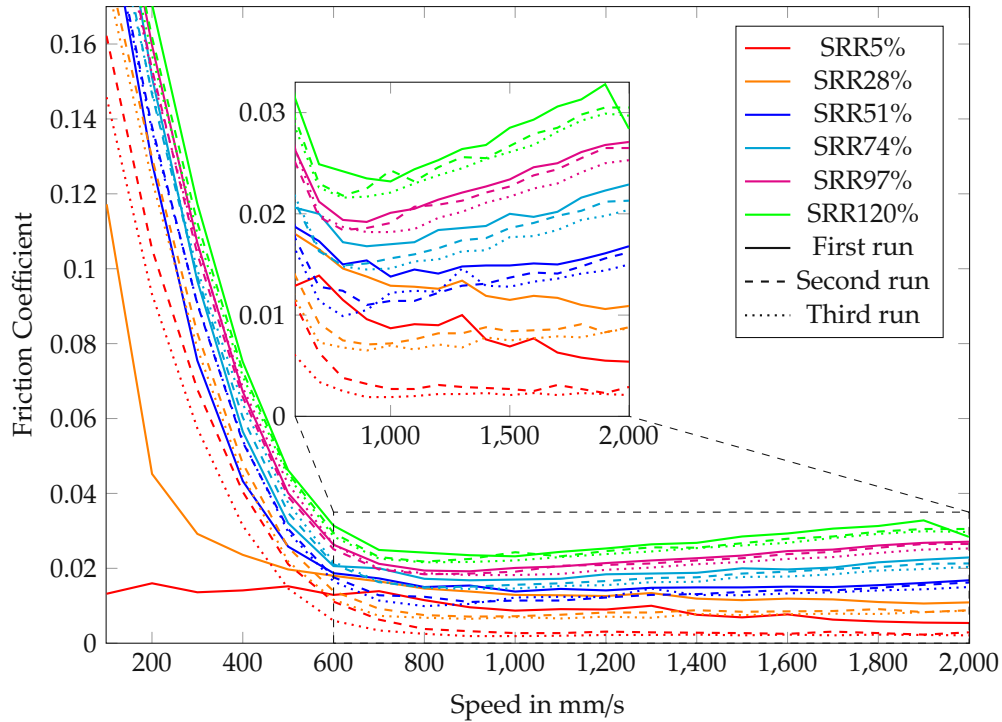

Figure 19: Stribeck curves for IL2 with 1% MXenes at 10 N and 30°C, with SRRs ranging from 5% to 120%. The curves were collected in three sequences, with each sequence covering the entire SRR spectrum. The portion of the plot corresponding to lower speeds initiates in the mixed lubrication regime.

Figure 20 shows the measurement results for pure glycerol under the same experimental conditions as for IL1 and IL2. Similar to the ILs, the COF for glycerol remains within the hydrodynamic regime across the entire range of speeds tested. This consistency is supported by a calculated lambda parameter of 5.25 at the lowest speed. Remarkably, glycerol demonstrates superior performance compared to the ILs, achieving a COF below 0.02 across nearly the entire speed range, except at the highest SRR and speeds. This observation of a low COF with glycerol aligns with findings reported by several other research groups [15, 104]. Unlike with the ILs, glycerol does not exhibit the phenomenon where successive test runs lead to improved tribological performance.

It is reported that under modest tribotesting conditions, there's a possibility of tribochemical polishing, driven by the chemical interaction between glycerol and the steel surface [108]. This polishing effectively diminishes local roughness, consequently facilitating the formation of lubricant films in those areas [136]. Our results suggest that the formation of such a tribofilm did not have a noticeable effect on the subsequent test runs. Hence, we anticipate that the tribological benefits of this polishing effect manifest without requiring a substantial running-in time.

Figure 20: Stribeck curves for pure glycerol at 10 N and 30°C, with SRRs ranging from 5% to 120%. The curves were collected in three sequences, with each sequence covering the entire SRR range. The entire curve falls within the hydrodynamic regime, aligning with numerical predictions.

In Figure 21, the COF for the glycerol-MXene mixture is plotted using the same settings on the MTM. A similar effect to that observed with IL2 is noted. However, the negative impact of MXenes at lower speeds is more pronounced here. Except for the initial run at a SRR of 5 %, all curves fall within the mixed lubrication regime. Notably, the first curve demonstrates a significantly higher friction than that of pure

glycerol, suggesting it does not fully reside in the hydrodynamic regime and that some surface contact does occur, leading to increased wear and consequently, a higher COF in subsequent runs. This phenomenon can be explained with the same reasoning as before. We anticipate two potential influences of MXenes on the gap distance when they enter the contact zone: firstly, they may prevent the formation of a continuous lubricating film and secondly, they could alter the rheological pressure-viscosity parameter. By examining the formula by Hamrock and Dawson, we can estimate the pressure-viscosity coefficient required for the COF to enter the mixed lubrication regime ($\lambda < 3$) at a speed of 100 mm/s, would need to be below 2. This indicates that MXenes would have to reduce the original coefficient to one-fifth of its value. Although nanomaterials are known to significantly affect this parameter [134], such a drastic change is very unlikely. Therefore, the unfavorable effect of MXenes is anticipated to be a result of the two factors combined. What is also striking, is that compared to the test with pure glycerol the COF experiences a decrease in the EHL region, while experiencing the just described increase in the mixed lubrication regime.

We hypothesize that variations in surface roughness offer a plausible explanation for the observed phenomena. While it is evident that in the mixed lubrication regime, an increase in surface roughness directly correlates with an elevation in the COF, the dynamics within the hydrodynamic regime are not as straightforward. A potential mechanism for the observed decrease in COF under EHL could be attributed to induced changes in effective viscosity [137]. These changes are possibly a result of pressure ripples caused by surface roughness, which, in turn, lead to a reduction in shear resistance [137].

Figure 21: Stribeck curves for glycerol with 1% MXenes at 10 N and 30°C, with SRRs ranging from 5% to 120%. The curves were collected in three sequences, with each sequence covering the entire SRR spectrum. The portion of the plot corresponding to lower speeds initiates in the mixed lubrication regime.

4.5.2 Visualizing Glycerol's Tribological Performance with a Heatmap COF Analysis

To enhance visibility and accommodate the extensive data volume, the MTM Stribeck curves are presented in the form of heatmaps. The MATLAB command 'shading interp' was employed for increased smoothness and improvement of the heatmap's visual quality. This means that the difference between each data point is displayed as a linear color gradient. All the subsequent heatmaps are designed to showcase the deviations in COF values between the pure base lubricants and their respective mixtures with MXenes, highlighting the impact of MXene addition on lubrication performance.

As explained in Section 3.3.2 and shown in Figure 20 and 21 each measurement was performed three times on the same disc to calculate the average COF. The initial measurement of several tests, conducted at a SRR of 5%, was excluded from the average value calculations for the heatmaps. This exclusion is due to the COF of the initial measurement typically being in the hydrodynamic lubrication regime, transitioning to the mixed lubrication regime in subsequent runs, a transition clearly evident in Figure 19. Following the initial test, subsequent measurements at different SRRs were conducted, which facilitated enough sliding to induce solid-solid contact and increase wear. Upon re-testing at an SRR of 5%, the now increased surface roughness, causes the lambda parameter to drop below three, thus indicating a shift to mixed lubrication. Removing these initial outlier measurements was important

for calculating the average COF, thereby ensuring the comparability of the heatmaps constructed from these values. Boidi et al. adopted a different approach in this context, employing a running-in period of 30 minutes (28 N and 195 % SRR) to ensure comparability [12].

Figure 22 illustrates the difference in COF (ΔCOF) between pure glycerol and glycerol with 0.25 wt.-% MXenes. As indicated by the Stribeck plots previously presented, glycerol's efficacy is reduced under a majority of the tested parameters when it is blended with MXenes. To demonstrate the increase in COF, the range of the color map for the glycerol heatmaps is adjusted accordingly and varies from that of the ILs heatmaps. Remarkably, even at a low concentration of 0.25 wt.-% MXenes, the effect on lubrication efficiency is significant. The heatmap demonstrates, that the scale of the COF increase is serious and exceeds 100 % increases under specific conditions. It is also noticeable that there are cases where reductions in friction (in the range of 10 %) are observable. This COF reduction occurs in regions experiencing the highest loads at elevated speeds. Regarding the improvements, it is noteworthy that all the mentioned enhancements are observed within the hydrodynamic regime, where both surface topography and the presence of MXenes typically exert minimal influence [65]. This suggests that the impact on the COF is predominantly governed by rheological behavior [65]. In comparison to pure glycerol, the surface roughness is heightened in the hydrodynamic regime due to wear from the preceding mixed lubrication regime. Consequently, it is anticipated that alterations in surface roughness induce a different pressure, which in turn leads to variations in viscosity.
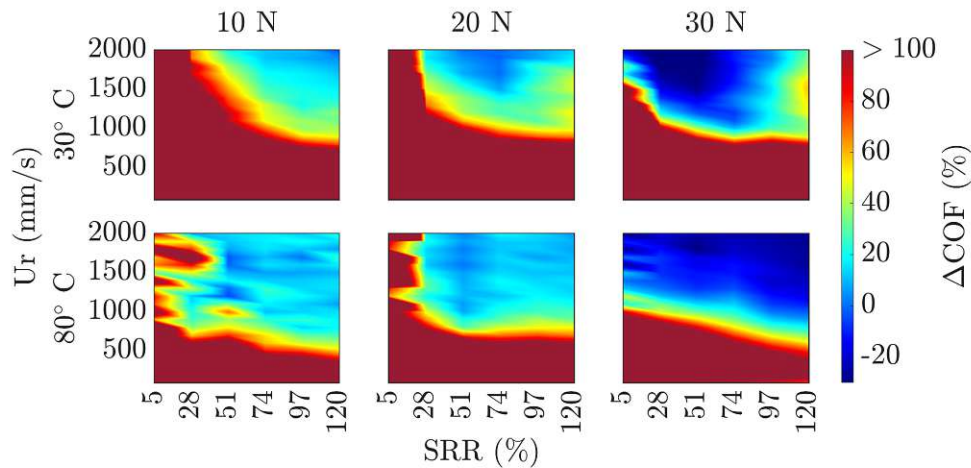
Figure 22: Heatmaps illustrating the change in coefficient of friction (ΔCOF) for glycerol with and without 0.25 % MXenes, across a range of SRRs from 5 to 120 % and speeds from 100 to 2000 mm/s, at both 30 and 80 °C.

Figure 23 presents the heatmap for glycerol with a 1 % addition of MXenes. When comparing this to the plots with a 0.25 % MXene concentration, we observe a notable increase in the COF at 80 °C for the higher MXene concentration. In comparison to the measurement with the lower concentration the measurement for 30 °C at 10 and 20 N yielded better results with a COF reduction in the range of 10 % at higher speeds.

The values for 30 N are missing here because not enough material was available and the force of 30 N was later added to the glycerol test matrix.

This observed behavior can be attributed to several factors. At elevated temperatures like 80 °C, the increased MXene concentration leads to a higher COF due to the potential decrease in film thickness. As the film thickness decreases the influence of the higher MXene particle concentration gets bigger, which in turn interferes with the lubricant's ability to form a coherent and effective lubricating film in the mixed lubrication regime. This implies that the Stribeck curves, at elevated temperatures, undergo an extended period of mixed lubrication. This extension consequently shifts the zones of improvement (illustrated as blue areas in Figure 23) towards higher speeds.
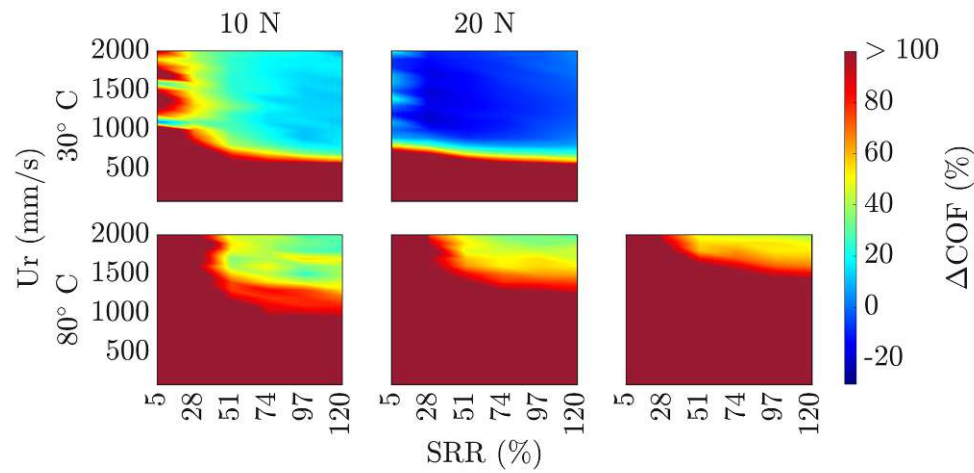
Figure 23: Heatmaps illustrating the change in coefficient of friction (ΔCOF) for glycerol with and without 1 % MXenes, across a range of SRRs from 5 to 120 % and speeds from 100 to 2000 mm/s, at both 30 and 80 °C.

During each measurement conducted at 10 N, an image of the ball surface was captured using the previously described SLIM setup. The lenses of the SLIM setup are prone to scratching, primarily because the ball repeatedly makes contact with the delicate silica spacer layer. To minimize costs, the glass lens was used for as long as possible, rotating the glass after each measurement. This rotation of the glass moves surface defects away from the contact zone, but they still manifest in the outer areas of the image. For enhanced clarity, defects outside the contact zone were digitally removed using Photoshop. In Figure 24, all captured images for glycerol are presented. Notably, at an SRR of 5 %, the accumulation of MXenes in the contact area is observable, indicated by the darker areas on the ball surface. We hypothesize that the presence of MXenes during this initial test run at an SRR of 5 % impedes the formation of a continuous lubricating film, resulting in a decrease in the lambda parameter of the MXene lubricants. Interestingly, at 80 °C, the presence of MXenes at the lowest SRR is not as noticeable as with the lower temperature. A possible explanation for this could be the significantly lower viscosity of glycerol at 80 °C. We evaluated the viscosity at 40 mPa*s at this temperature. Therefore, it is likely that less glycerol, and consequently fewer MXenes, adhere to the surface of the ball, leaving a cleaner ball surface with fewer MXenes. While the SLIM setup isn't optimal for wear analysis, necessitating subsequent laser microscope analysis, the SLIM images already illustrate that the presence of MXenes notably amplifies abrasive wear. This is caused by the surfaces coming into contact earlier during the measurement when MXenes are present.
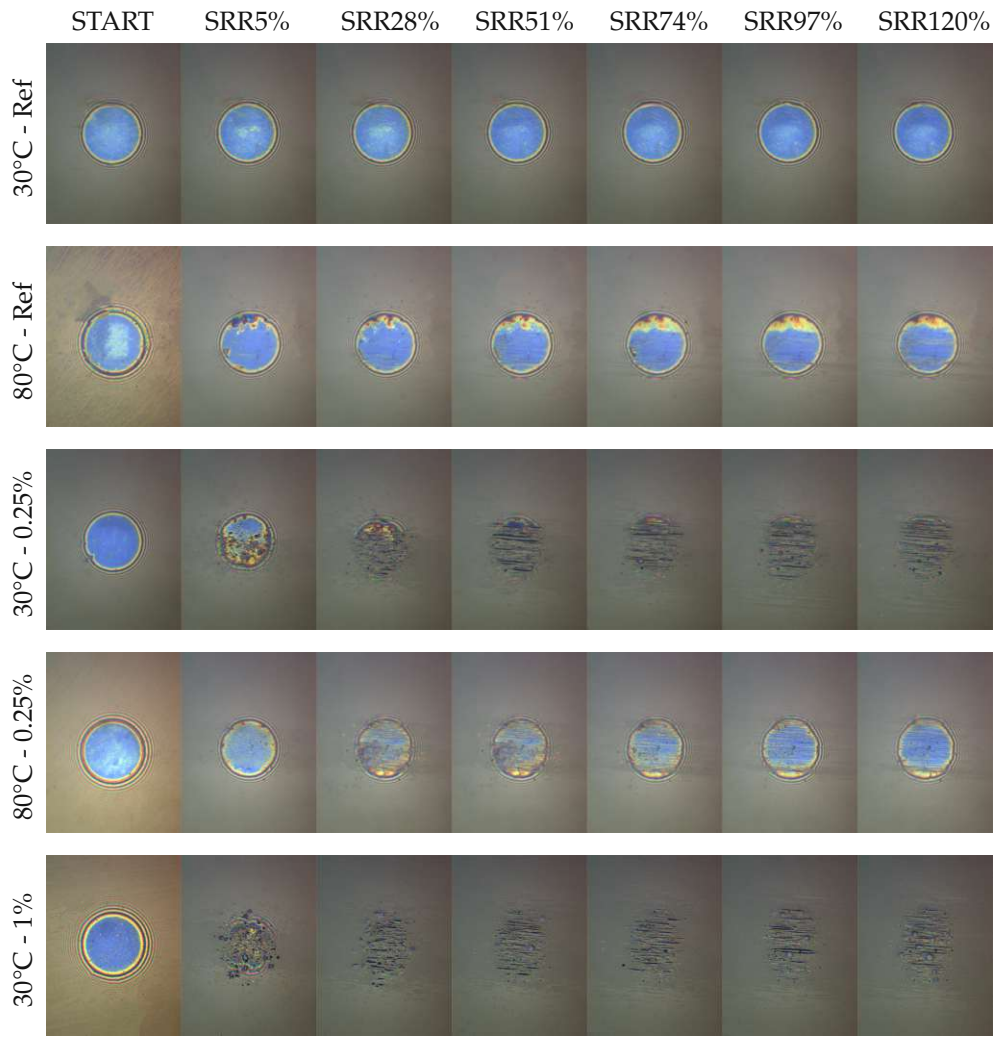
Figure 24: SLIM images during glycerol measurements captured without MXenes and with MXenes at concentrations of 0.25 and 1 wt.-%, conducted at 10N and temperatures of 30 °C and 80 °C, across SRRs ranging from 5 to 120 %.

4.5.3 Comparative Analysis: Investigating the Challenges of Glycerol-MXene Mixtures

To further investigate the poor results of the glycerol and MXene combination, additional analysis of the test conditions is needed. The quantity of MXenes used in the conducted MTM tests falls within a comparable range as employed by previous groups [11, 65], indicating that this factor is not responsible for the elevated friction. However, one notable difference regarding the sample composition is the amount of glycerol used. In Yi et al.'s experiments, MXene powder was initially mixed with deionized water, followed by the addition of a small amount of glycerol in a 5:1 ratio. This indicates a substantial difference in the quantity of glycerol used. Additionally, the sonication process was carried out when the solution did not contain any glycerol. The sonication of MXenes in water can produce varied outcomes compared to MXenes in pure glycerol due to differences in viscosities [64] and the potential intercalation of water molecules. When working with nanomaterials, it has been previously noted [64] that favorable outcomes through sonication are only achievable when the base liquid exhibits low viscosity. Another aspect is that a Si_3N_4 ball and a sapphire substrate were used, while the experiments for this thesis were run with a steel ball and disc. The differences of the surfaces in the contact zones can have adverse effects on the performance of the MXene flakes. For example, Yi et al. demonstrated that a tribochemical reaction occurred with the Si_3N_4 ball surface, leading to the presence of titanium and silicon oxides on the surface of this tribofilm. The tribofilm on the sapphire substrate retained the stacked morphology of MXenes with a reduced presence of oxides. Another significant distinction between their work and this analysis lies in the aspect of timing. The test profile utilized in this study involved frequent changes in parameters. In contrast, Yi et al.'s work maintained consistent parameters, allowing for a 20-minute run-in phase after which superlubricity was achieved.

To validate that our measurements are not influenced by inadequate sample preparation or test parameters, supplementary tests were conducted using alternative methods and parameters. The measurement parameters were configured in the same order of magnitude outlined by Yi et al [11] and are described in Section 3.4. Notably, a post-test observation revealed a distinctive color change. Both the ball and disc were covered in a black layer. This points towards the presence of either an oxide layer or a tribofilm. The formation of this tribofilm could be attributed to the enhanced exfoliation of MXenes during sonication in the less viscous deionized water [64]. Better-exfoliated MXenes have an increased surface area, which improves substrate interactions, including with steel, through physical mechanisms like Van der Waals forces and mechanical interlocking, or chemical means such as covalent bonding [138]. The development of this black film may also be ascribed to increased oxidation due to the introduction of water [63]. The chemical oxidation process for the MXenes is illustrated in Equation 15. Given that TiO_2 particles typically have a white coloration, the black layer observed on your samples, suggests the presence of different oxidation states of MXenes and possibly magnetite. This indicates a complex oxidation process distinct from the straightforward creation of TiO_2.

$$Ti_3C_2O_2 + 4\,H_2O \longrightarrow 3\,TiO_2 + 2\,C + 4\,H_2 \tag{15}$$
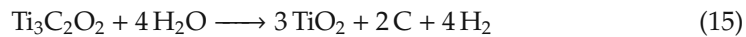
The black layer adhered to the ball and disc of the MTM, leaving the steel lubricant container uncovered. With the laser scanning microscope VK-X1000 built by Keyence the wear scar was analyzed. Figure 25 shows the surface of the disc in the wear scar area. The black dots visible in the 20x magnification could be the result of micro pitting. Micro pitting in tribology refers to the formation of very small pits or craters on the surface that formed due to oxidation. The craters are created when the oxidation pits are removed due to the rolling or sliding motion of the surfaces. Given the presence of this potential micro pitting during the test, it is reasonable to assume that oxidation occurred. However, in instances of pronounced oxidation, surface scars or fissures are typically anticipated, yet they are not evident in this case.

Figure 25: Laser microscope image revealing the wear scar of the sample subjected to the water-glycerol-MXene mixture.

Figure 26 illustrates the COF values measured during the experiment involving the glycerol, water and MXene mixture. The experimental conditions underwent a modification after five hours, as previously explained. This parameter change is denoted by the red line in the plot. These results prove that the run-in phase, the sample preparation and the nature of the lubricant were not the decisive factors that led to the low performance of glycerol with MXenes in the previous tests. This is evident because the friction was not significantly lower than during the previous tests and substantially higher than the superlubricity archived by Yi et al. The only remaining differences to the tests conducted by Yi et al. [11] are the nature of the surfaces and the size of the ball. The ball used by Yi et al. had a surface finish of Ra = 10 nm and a diameter of 4 mm [11]. In the tests conducted for this thesis the ball had a diameter of 3/4" (19.05 mm) and both surfaces had a surface finish of 20 nm. On the other hand, they used a Si_3N_4 ball surface and a sapphire substrate, in comparison to AISI 52100 steel in this work. The influence of the Si_3N_4 surface involves the formation of a tribofilm during the running-in period, characterized by tribochemical reactions with $Ti_3C_2T_x$ MXenes [11]. This results in a composite layer of colloidal silicon oxides and titanium oxides. Furthermore. the detection of Ti–N and Ti–O–N bonds confirmed the chemical interplay between MXene and Si_3N_4 [11]. In contrast to the reported improvements with MXenes on Si-based surfaces, our work does not reveal significant beneficial effects of glycerol-MXene mixtures on reducing the COF. However this does not mean that MXenes are incompatible with steel surfaces as beneficial tribolayers, composed of thermally and mechanically degraded MXene nanosheets alongside amorphous/nanocrystalline iron oxide, have been observed by other groups [9, 138].
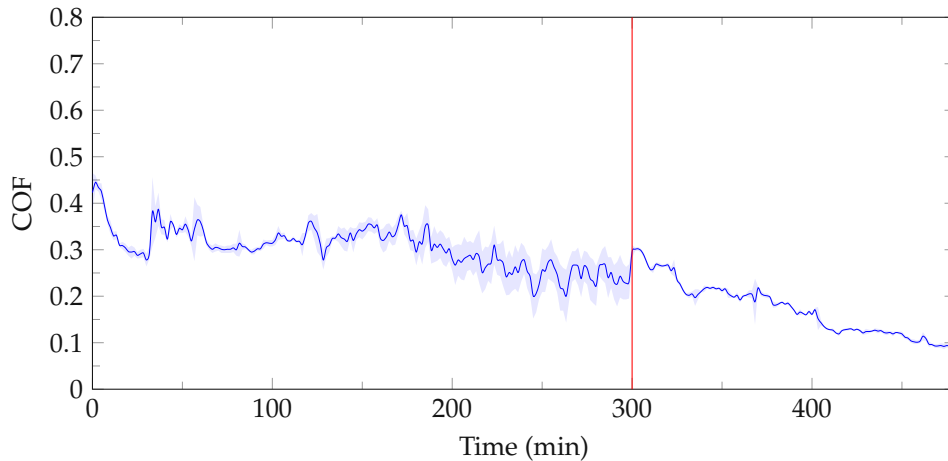
Figure 26: COF plot for water-glycerol-MXene lubricant at a constant speed of 200 mm/s and force of 2N for 5 hours, followed by a parameter change (red line) with speed and force increasing to 1000 mm/s and 5N over the next 3 hours.

To investigate the surface interactions and potential formation of a tribofilm on our samples, we employed Raman spectroscopy with a green laser, at a maximum aperture and an exposure duration of 75 seconds over two cycles. The Raman measurements, depicted in Figure 27, were conducted both within the contact zone and on the areas of the disc covered by the black layer, denoted by blue and red circles, respectively. These captured data was then refined using the Asymmetric Least Squares method and compared to the Raman spectra of MXene powder depicted in Figure 5.

The wear track sample exhibited distinct peaks indicative of MXenes, notably a broad peak at approximately 157 cm^{-1} and a sharper one at 222.7 cm^{-1}, closely aligning with the initial powder measurements at 160 and 220 cm^{-1}, respectively. The peak at 222.7 cm^{-1} also corresponds with the anatase form of TiO_2, as identified at 221 cm^{-1} by Yi et al. [11]. The subsequent peak at 285.4 cm^{-1} matches observations of the -O surface termination and the peak at 388.1 cm^{-1}, although not perfectly aligned with our group's reported measurement for -OH termination at 376 cm^{-1}, likely signifies the presence of -OH MXene terminations. Although this peak does not precisely match the result from our measurement it can be noted, that we are observing the MXenes in a completely different state. Sarycheva et al. have reported similar deviations in peak positions when comparing different states of MXenes, such as flakes, films, or clays [139].

Additionally, the peak at 448.1 cm^{-1} can be attributed to TiO_2 (E_g mode) in its rutile phase, consistent with literature reports of Raman shifts around 448 cm^{-1} [140]. The peak at 610 cm^{-1} aligns with the A1g mode of TiO_2, closely matching the reported value of 612 cm^{-1}. Furthermore, the peak at 1067.1 cm^{-1} parallels the primary Raman peak for glycerol at 1055 cm^{-1}, typically associated with the C-O stretching vibration in C-OH groups [141]. The final two peaks are reminiscent of the D and G bands of graphitic carbon, further supporting the presence of MXenes on the disc's surface. The Raman measurements demonstrate, that MXene nanoflakes indeed adsorbed

on the worn surfaces of the steel disc maintaining their original structure. Yi et al. observed a similar surface composition on their sapphire substrates. However, the Raman spectrum from the Si_3N_4 ball surface they used indicated the presence of colloidal silicon oxides, suggesting a tribochemical reaction with the Si_3N_4 surface [11]. Our experiments yielded a COF greater than 0.2, which, although not reaching the superlubricity threshold, still provides valuable insights into the behavior of this unique lubricant mixture on steel surfaces, particularly under the specific test conditions of pure sliding without rolling. Based on our observations, we anticipate that employing a Si_3N_4/steel interface might also achieve COFs at a superlubricity level. The potential for this lubricant mixture to perform effectively with steel counterparts, as opposed to solely with sapphire substrates, significantly enhances its applicability. Given the widespread use of Si_3N_4 ceramics as rolling elements in ball bearings [142, 143], this compatibility could broaden the lubricant's utility across a wider range of applications.

The red line in the Raman spectrum, representing measurements from areas covered in the black layer, confirms the widespread presence of MXenes across the disc. The black coloration of both the ball and disc could be attributed to two factors: the inherent color of MXenes and the close proximity of observed peaks to those of magnetite (668 and 193 cm^{-1}), which could explain the uniform black coating observed. In light of these findings, further analysis using XPS is recommended to provide a more comprehensive understanding of the surface chemistry and composition of the black layer.
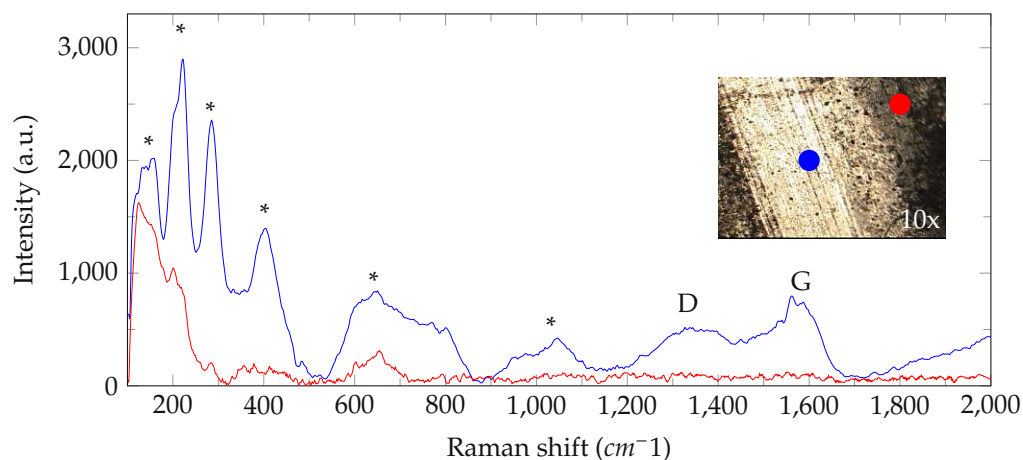
Figure 27: Raman spectra of the disc's wear track, showcasing the characteristic peaks that elucidate material transformations and stress-induced modifications at the molecular level.

4.5.4 Heatmap Visualization and Analysis of the Tribological Performance of Ionic Liquids

Shifting the focus from glycerol-based lubricants, the next segment analyses the interaction between ILs and MXenes. This segment unveils how ILs perform in the presence of 0.25 and 1 wt.-% of MXenes, by illustrating the COF measurements in heatmaps. In these heatmaps for IL1 and IL2, white areas indicate that the lubricants containing MXenes exhibited inferior performance compared to the pure base liquids.

49

In general collected results with ILs present a more promising outlook, suggesting compatibility with MXenes. The utilization of pure ILs as base lubricants is currently improbable, mainly due to availability and cost. However, ILs are also being explored as additives to lubricants [101]. Therefore the information in the following heatmaps is also crucial for understanding the coexistence of these two lubricant additive candidates.

Figure 28 illustrates the performance of IL1 with 0.25 wt.-% MXenes. What is evident, is that the IL1 with 0.25 wt.-% of MXenes exhibited superior performance compared to the pure IL. MXene addition significantly enhances lubrication under higher loads and temperatures, demonstrating their value in challenging environments. The IL-MXene mixture shows optimal performance at 80 °C and lower speeds, with effectiveness increasing at lower SRRs, broadening the effective speed range. This is visually represented by the blue areas in the plots, highlighting the conditions under which MXenes contribute most to lubrication efficiency. A remarkable decrease in the COF of up to 90 % was measured. This substantial reduction in friction is unquestionably attributed to the outstanding solid lubricant properties of MXenes. In the heatmap images obtained at room temperature with 10 and 20 N, the performance was relatively modest.

An interesting observation with IL1, which was already discussed with the Stribeck plots, is that the mixed lubrication regime does not experience a significant shift to higher COFs when MXenes are added. With IL1 the MXenes improving capabilities start in the mixed lubrication regime. However at the bottom of the plots at 80 °C a fine line where the performance was reduced can be seen. We anticipate that MXenes play a crucial role during the initial formation of the tribofilm at the onset of the Stribeck curves. After a certain running in time (the small band at the bottom of the plots) the MXenes are integrated into the film and provide a cushioning effect, therefore effectively improving the protective capabilities of the tribofilm. Essentially, we observe that the COF initially increases with the addition of MXenes, followed by a more pronounced decrease. At first, MXenes slightly interfere with film formation, but they later engage in synergistic interactions with IL1, facilitating possible incorporation into the tribofilm. Once MXenes are integrated into the film and aligned in the contact zone [10], they introduce a significant drop in COF. Due to this effect, TEM analysis was deemed necessary in order to verify that the MXenes are an integral part of the phosphorous IL1 tribofilm, which was already observed by our group [17]. The absence of this effect at lower speeds in the plots at 30 °C stems from all Stribeck curves for IL1 being in the hydrodynamic regime. Consequently, they do not undergo surface contact significant enough to showcase the influence of a tribofilm buildup.

What stands out here is that the results do not correlate with Boidi et al. [12]. They measured the performance of Polyalphaolefin (PAO) oil with 0.5 and 3 % MXenes. Their findings indicate that, with PAO, the friction reduction by MXenes increases with decreasing load and temperature. This is in direct contrast to the observations from this work. A possible explanation for this effect is that higher loads lead to the tribochemical generation of tribofilms [17, 92], as discussed in Section 2.3.2. The

performance issues may also be related to the ILs higher viscosity. ILs require more "activation" compared to oils [144]. At lower loads, the oil combination might have already operated at its limit and its performance only worsened under higher loads, to a point where even the addition of MXenes could not offer further improvement. Other possible reasons for this contrasting behavior may be attributed to the nature of MXenes and the nanoscale interactions with the base liquids.
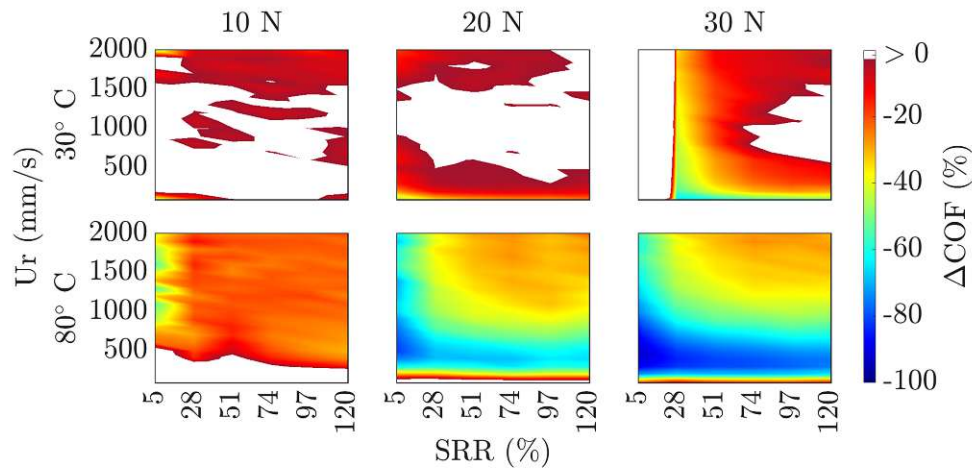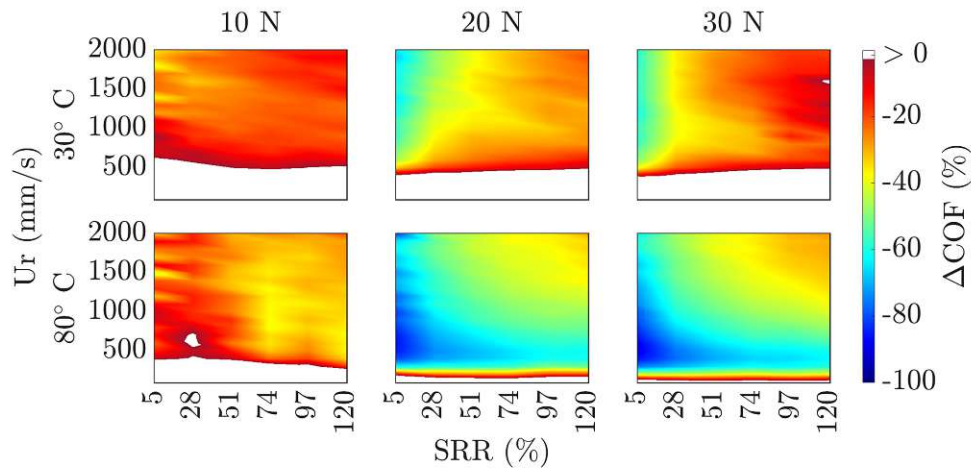
Figure 28: Heatmaps illustrating the change in coefficient of friction (ΔCOF) for IL1 with and without 0.25 % MXenes, across a range of SRRs from 5 to 120 % and speeds from 100 to 2000 mm/s, at both 30 and 80 °C.

After testing samples with a concentration of 0.25 wt.-%, the concentration was increased to 1 wt.-% and the results are illustrated in Figure 29. The COF values indicate a significantly improved performance of the lubricant, particularly at higher loads and temperatures, where fewer areas with increasing friction are evident. The principle phenomena observed at lower concentrations are also evident here. As with the lower concentration, the measurements at 30 °C fall within the hydrodynamic region. Of particular interest is the slight enhancement of the film's lubricating capabilities across nearly the entire speed and SRR spectrum in the presence of MXenes. This improvement is supported by a subtle shift in the Stribeck curves recorded with MXene additives. As MXenes facilitate an earlier exit from the boundary regime (at speeds below 100 mm/s), the hydrodynamic regime demonstrates improved COFs. In this context, a significant role can be attributed to the potential alteration of the pressure-viscosity coefficient, influenced by the incorporation of MXenes.
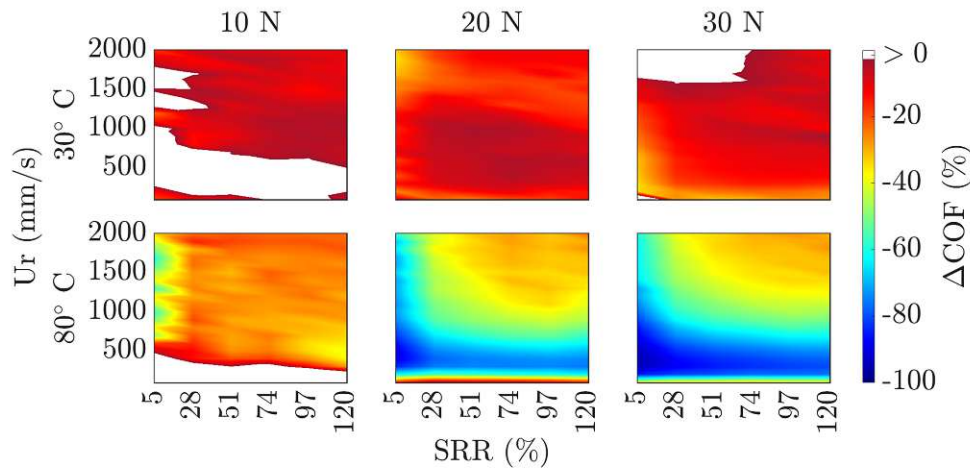
Figure 29: Heatmaps illustrating the change in coefficient of friction (ΔCOF) for IL1 with and without 1 wt.-% MXenes, across a range of SRRs from 5 to 120 % and speeds from 100 to 2000 mm/s, at both 30 and 80 °C.

Similar to the glycerol measurements, the SLIM setup was utilized to in-situ capture images of the ball surface for IL1. Figure 30 presents all the images for IL1 captured during the initial test run at 10 N. Interestingly, at 30 °C, no significant accumulation of MXenes on the surface is evident at lower SRRs. This can be attributed to the majority of measurements with IL1 at 30 °C occurring within the full film hydrodynamic regime. Consequently, no notable film buildup is observed, as there is minimal contact to facilitate the tribochemical reaction leading to tribofilm formation. However, at 80 °C, the measurement indicates that the COF was in the mixed lubrication regime under certain parameters. Therefore, we anticipate that this results in the incorporation of MXenes into the phosphorus-based amorphous tribofilm. This incorporation is observable at both concentrations at 80 °C. Of significance is the second image at an SRR of 5 %, which exhibits minimal wear. It is known that significant wear compromises SLIM measurements, leading to inaccurate thickness measurements and difficulties evaluating tribofilm formations [145]. Both of these images at the lowest SRR indicate the presence of MXenes on the surface, as evidenced by the darker dots within the contact area.
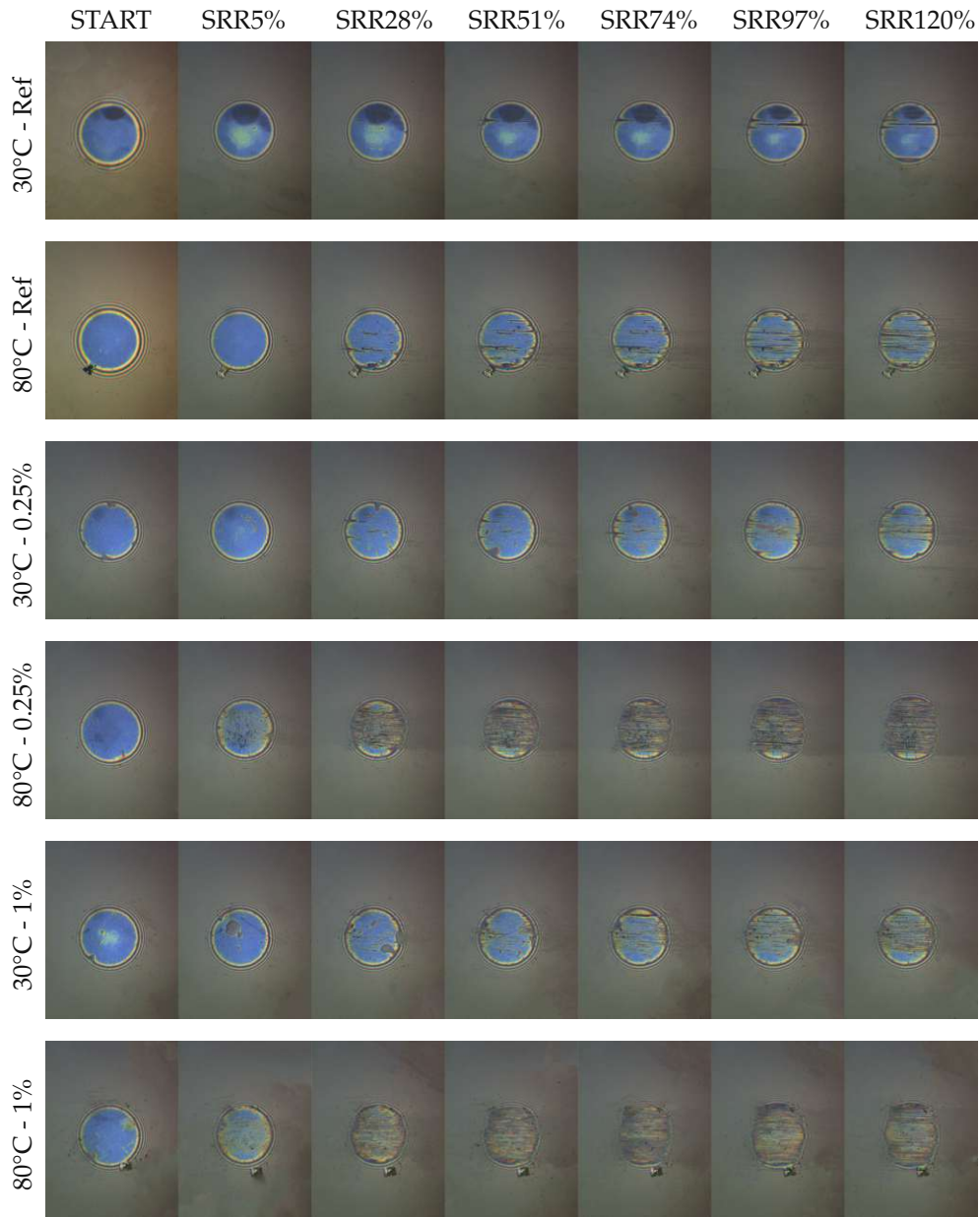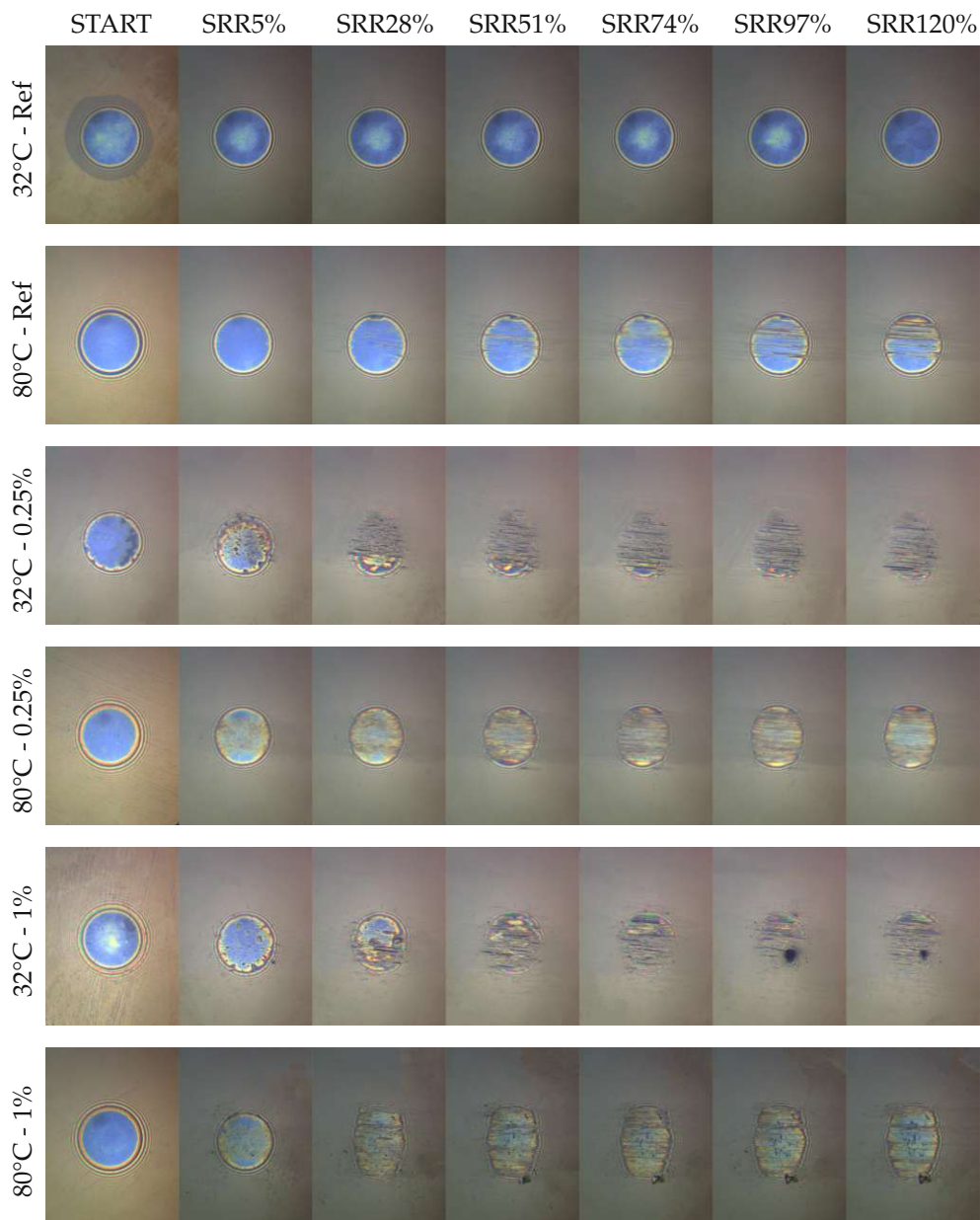
Figure 30: SLIM images depicting IL1 measurements captured without MX-enes and with MXenes at concentrations of 0.25 and 1 wt.-%., conducted at 10N and temperatures of 30 and 80 °C, across SRRs ranging from 5 to 120 %.

The following two heatmaps present the outcomes of the tests conducted with IL2. Notably, with a 0.25 wt.-%. MXene concentration, the reduction in friction is considerably enhanced at lower temperatures compared to IL1, as depicted in Figure 31, where the COF reduction reaches 60 %. The enhancements at 30 °C occur in the hydrodynamic regime again. Similarly to glycerol, the addition of MXenes to IL2 leads to mixed lubrication, where the pure IL2 is already in the hydrodynamic regime. This effect is resembled by the white gaps at low speeds at 30 °C and was not observed with IL1 at 30 °C. The overall performance at higher loads and temperatures is reduced in comparison to IL1 as the improvements are in the range of approximately 80 %. This aligns with the Brugger evaluation, where high loads, speeds and temperatures are present and where IL1 also emerged as the top performer. At higher temperatures, IL2 has a comparable behaviour to IL1 as improvements in the mixed regime are evident after an initial performance reduction at the lowest speed.
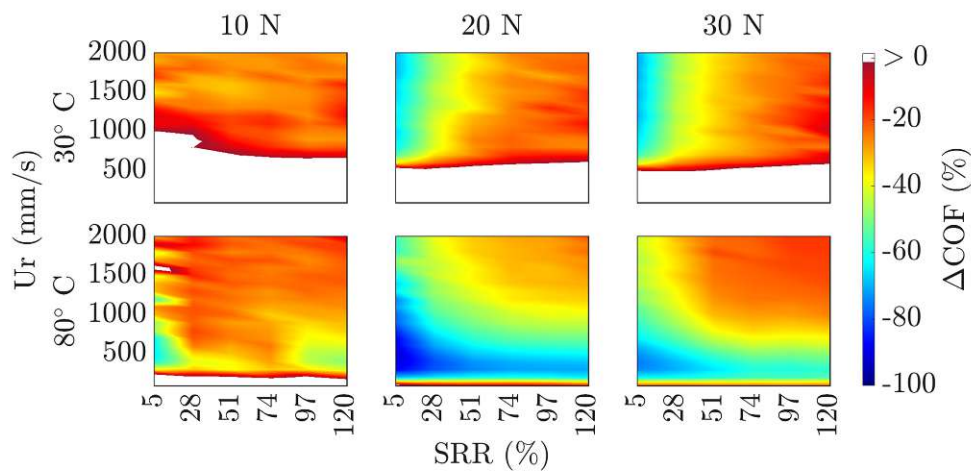
Figure 31: Heatmaps illustrating the change in coefficient of friction (ΔCOF) for IL2 with and without 0.25 wt.-% MXenes, across a range of SRRs from 5 to 120 % and speeds from 100 to 2000 mm/s, at both 30 and 80 °C.

The lower sections (up to speeds of 500 mm/s) in both IL2 heatmaps reveal an increase in the COF at 30 °C. This is once again a consequence of the previously discussed phenomenon associated with the IL2-MXene combination's delayed exit from the mixed lubrication regime. The properties of MXenes that enhance performance do not become more pronounced with the slight increase in concentration. This suggests, that the change of MXene concentration from 0.25 to 1 wt.-% did not significantly alter the tribological performance.

Figure 32: Heatmaps illustrating the change in coefficient of friction (ΔCOF) for IL2 with and without 1 wt.-% MXenes, across a range of SRRs from 5 to 120 % and speeds from 100 to 2000 mm/s, at both 30 and 80 °C.

A notable observation evident in all the IL heatmaps is the substantial reduction at lower speeds, higher loads and higher temperatures. Under these conditions, increased surface contact becomes more probable. When surface contact occurs the tribological influence of a tribofilm starts and consequently leads to a reduction of the COF. Therefore this is an indication for the presence of such a protective layer that was formed.

Figure 33 presents a compilation of SLIM images for the IL2 measurements. What is evident here is the significant increase in abrasive wear attributed to the presence of MXenes with IL2. Subsequent roughness measurements will confirm that IL2 indeed experienced the highest increase in abrasive wear due to the presence of MXenes. Of particular interest in this observation is that while the MXenes initially hindered the formation of a continuous lubricating film, the heatmaps indicated that the reduction in COF remained significant under certain conditions, as discussed earlier. Therefore, it can be concluded that while the MXenes led to more surface contact (lower λ-parameter) at the beginning of the measurements, they subsequently revealed their beneficial tribological properties, resulting in lower shear resistance and reduced COFs.

Figure 33: SLIM images depicting IL2 measurements captured without MX-enes and with MXenes at concentrations of 0.25 and 1 wt.-%, conducted at 10 N and temperatures of 30 and 80 °C, across SRRs ranging from 5 to 120 %.

4.5.5 Tribological Performance Comparison of Glycerol and two Ionic Liquids

To deepen the insights into the performance of the base lubricants and to compare the three liquids when paired with MXenes, the COF values at a SRR of 51 % are plotted in Figure 34. This specific SRR was chosen based on the previous heatmap analyses, which showed that MXenes significantly enhance friction reduction in regimes with a higher proportion of rolling. However, an SRR of 51 % was selected to ensure a substantial amount of sliding is still present, where the friction-reducing capabilities of MXenes remain notably effective, maintaining a balance between rolling dominance and meaningful sliding interaction.

The analysis reveals that pure glycerol consistently outperforms pure ILs across all evaluated conditions at an SRR of 51 %. When comparing pure glycerol against IL1 and IL2, with the addition of MXenes at concentrations of 0.25 and 1 wt.-%, the COF values closely approach those of glycerol, indicating a marked improvement in lubrication performance. However, as Figure 35 has previously demonstrated, there are no instances where IL1 exceeds the performance of glycerine at an SRR of 51 %, affirming that pure glycerine remains the superior lubricant at these parameters. The outstanding tribological performance of glycerol has been extensively reported in the literature [15, 104, 111, 146]. In our work, we used pure glycerol, but concerning the use of glycerol as a lubricant, adjustments to the water content in glycerol-water mixtures have been shown to reduce the lubricant's viscosity, facilitating a low, consistent COF alongside low wear rates [110]. The performance of glycerol as a lubricant remains uncompromised even with water additions up to 40 % [146]. This, according to Chen et al. can be attributed to the glycerol molecules ability to dissolve and form a hydrogen-bonded layer with water molecules, effectively sustaining nominal loads [111]. When we look at glycerol in combination with MXenes, the COF values generally exhibited an increase at an SRR of 51 %. This suggests that under the given circumstances, the anticipated improvement from glycerol-MXene mixtures was not observed. These results deviate from research by other groups [11, 16], which have even achieved superlubricity on the macroscale with such material combinations.

Considering the exceptionally low COFs for all tested lubricants, highlights their potential as viable alternatives to conventional oils. This potential is further emphasized when comparing our results with those of Boidi et al. [12], who reported COFs of 0.022 at 10 N and 0.028 at 30 N for PAO 8 oil under the same conditions (51 % SRR and 80 °C) in the hydrodynamic regime. In contrast, this work demonstrates that all tested lubricants, including ILs and glycerol, exhibit COFs of 0.01 or lower at 10 N and do not exceed 0.015 at 30 N in the hydrodynamic regime. This represents a substantial reduction in COF, nearly halving the values compared to PAO 8 oil and underscores the impressive lubrication efficiency of these green lubricants under the tested parameters.
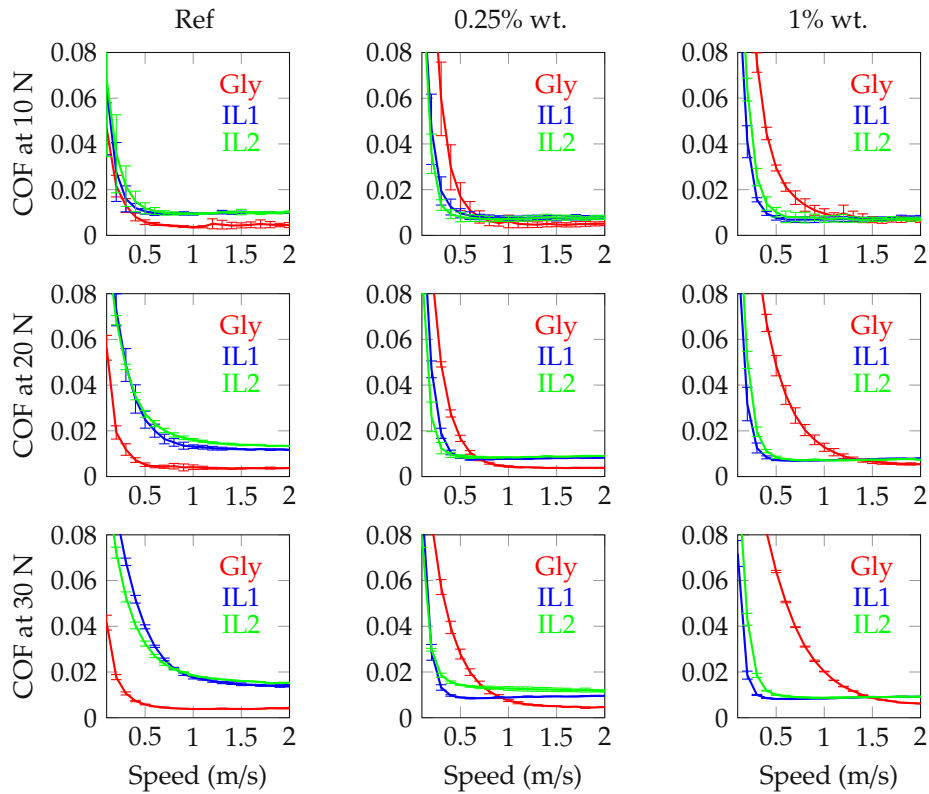
Figure 34: COF compared at SRR51% and 80 °C

As previously discussed, pure glycerol emerged as the unexpectedly superior performer among the three lubricants at the applied test conditions. To provide a more detailed analysis of glycerol's performance, a heatmap depicting the delta COF values for glycerol and IL1 with 1 wt.-% MXenes (the top performer among the lubricants with MXenes) is shown in Figure 35. As this plot shows, the areas where IL1 outperformed glycerol are very limited. The IL demonstrated reduced COF values at lower speeds and higher temperatures. The three images at 30 °C consistently show higher COF values for IL1 across the entire SRR range, except at 10 and 30 N where the IL1 test had a slightly better performance at low a SRR. It is important to note that the discrepancy at 10 N could also be attributed to measurement inconsistencies, as deviations in measured values were particularly evident at low SRRs and small loads. At 30 N, on the other hand, a small blue area is visible at the lowest speeds, demonstrating that under severe conditions, where both lubricants are in the mixed lubrication regime, the MXenes significantly improve the interfacial properties of the friction pairs [65]. This enhancement results in MXenes significantly improving IL1, enabling it to surpass the performance of glycerol, a lubricant that has demonstrated lower COFs when comparing the pure forms. At 80 °C the areas where the MXenes can unveil their tribological properties become more pronounced. It is once again evident that the improvement occurs primarily in the parts of the Stribeck curves where inter-facial contact occurs.
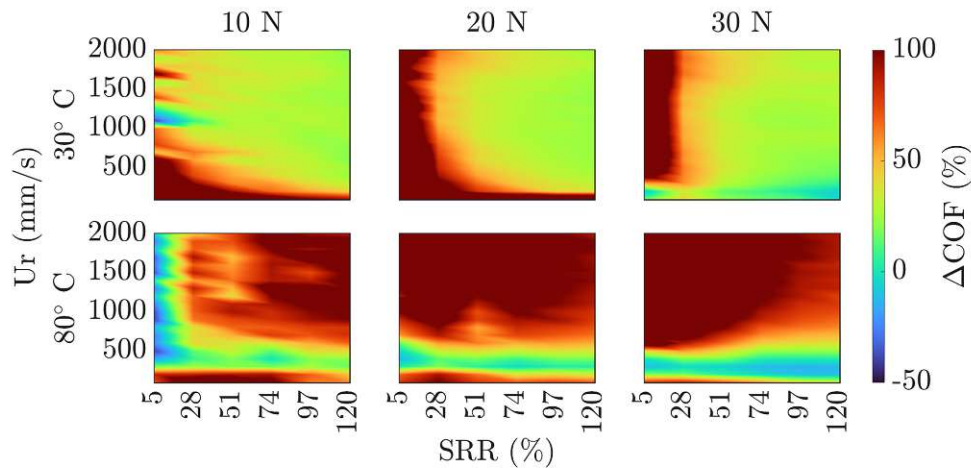
Figure 35: Comparison of IL1 with 1 wt.-% MXenes and pure glycerol. Negative values mean, that IL1 with MXenes performed better than the glycerol.

After undertaking the MTM experiments, the evaluation of the surface roughness parameter S_z was performed using the VK-X1000 microscope. This microscope provides the capability to select a specific area for calculating the S_z value. The chosen area maintained a consistent scale across all measurements. Figure 36 reveals an observable increase in the size of the wear scar in tests conducted with MXene additives. This phenomenon has been previously observed by Boidi et al. [12] and it aligns with the findings from the MTM Stribeck curves. As illustrated in the plotted Stribeck curves, the introduction of MXenes leads to an earlier transition of the COF to the boundary lubrication regime. Taking the IL2 example, lubricants enhanced with MXenes exhibit entry into boundary lubrication at 10 N and a SRR of 28 %, whereas pure base liquids experience this transition at higher loads and SRR values. As anticipated by the Stribeck plots, Figure 36 confirms that the addition of MXenes had a minimal impact on the wear scar size of the IL1 samples. Notably, the images reveal that the samples with glycerol at a 0.25 wt.-%. MXene concentration underwent significant corrosion, attributed to the storage conditions with the glycerol coating their surfaces. This corrosion complicates the accurate assessment of the actual wear scar depth for this sample.
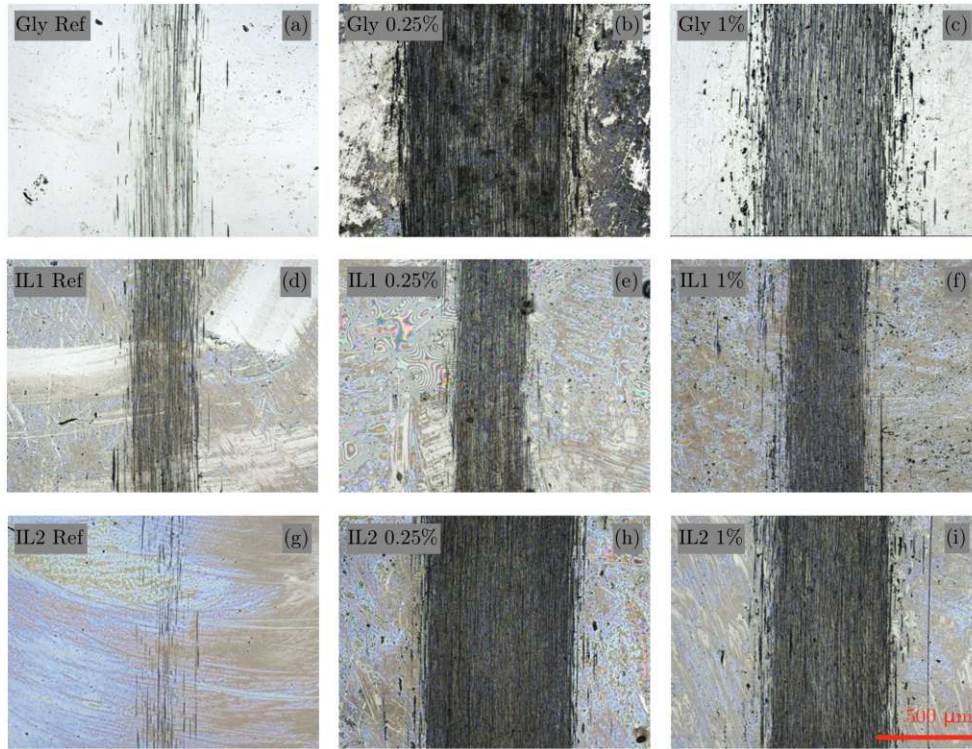
Figure 36: Wear scars from the examined samples, with the selected area for roughness parameter evaluation highlighted by the blue rectangle.

To gain a deeper understanding of the wear scars, depth profiles were selected for a more detailed examination of the wear on the MTM discs. These profiles, as depicted in Figure 37, correspond to the same regions illustrated in Figure 36. The presence of grooves aligned with the wear direction suggests abrasive wear. However, given that MXenes are non-abrasive by nature [65], it is clear that the observed wear does not directly result from the MXene additives. Instead, it appears to be due to the impact of MXenes on film formation and oxidation processes. The abrasive particles may be steel chips that have undergone hardening through deformation or oxidation. On the other hand, MXenes become TiO_2 particles during the oxidation process. These particles are known to exhibit moderate abrasiveness [86].
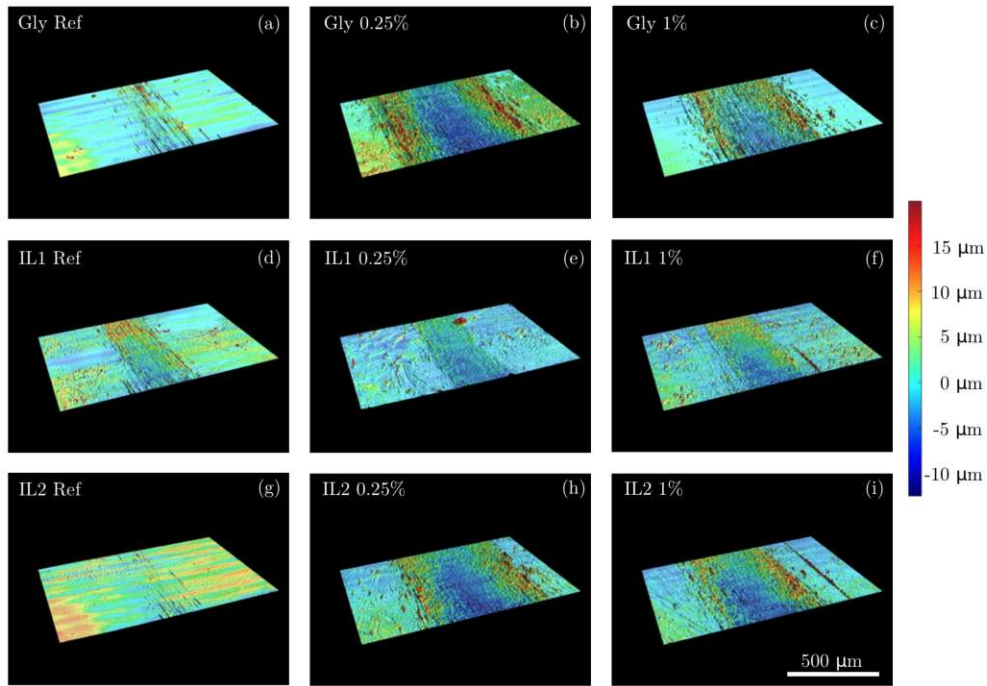
Figure 37: Wear scars from the examined samples, with the selected area for roughness parameter evaluation highlighted by the blue rectangle.

Figure 38 illustrates the assessment of the S_z parameters. As the images above indicated, the depth of the wear scar increases with the addition of 0.25 wt.-% of MXene powder. Taking this phenomenon into account, a question arises: why does increased wear result in the measurement of decreased friction? This can be explained through two conclusions. Firstly, the lubricants exhibit poorer performance in the white heatmap areas. These white areas in the heatmaps are in the mixed lubrication regime where MXenes lead to surface contact at lower speeds and loads compared to the pure base liquids. This diminished performance in specific areas contributes to increased wear. Secondly, the resulting wear increase leads to an enlarged contact area, possibly responsible for decreased friction in the hydrodynamic regime. Hao et al. [147], for instance, observed a similar effect in their study on friction testing of textured steel surfaces under cylindrical line contact conditions. Wear contributed to an expansion of the cylinder's contact area. This increase in contact area resulted in reduced contact pressures, which in turn facilitated the improvement of the hydrodynamic film. This gives rise to the open matter of what role this effect played in areas of decreased friction. The extent of this phenomenon cannot be entirely verified and it is possible that this led to a seemingly increased performance with MXenes. Most likely the decreased friction can be attributed to a mix of the just-discussed contact surface effect and the positive impact of MXene nanosheets.
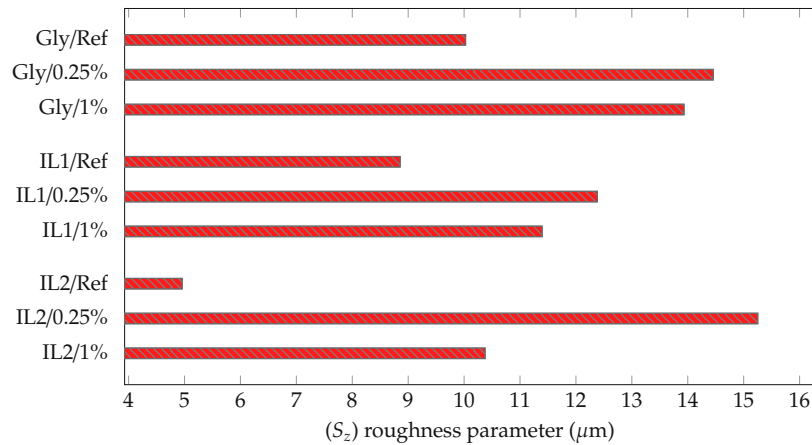
Figure 38: Surface roughness parameters (S_z) for the tests conducted at room temperature.

4.5.6 SLIM-based Film Thickness Evaluation

The SLIM setup, previously detailed in Section 3.3.1, offers the capability for in-situ measurement of film thickness formation. The results of this thickness measurement are shown in Figure 39. The thickness measurements reveal the accumulation of a potential tribological film; however, this assessment may be subject to influence from wear. Considering the uncertainty associated with the measured values, a more thorough investigation with TEM was deemed necessary. This supplementary analysis will be explored further in Section 4.6. The SLIM evaluation was conducted at each load, but it became evident that with the prolonged test duration, the glass surface experienced substantial scratching, leading to a distortion of the results. Consequently, the decision was made to exclude images and thickness values from the SLIM data after the 10 N MTM run. This can also be argued by asserting that the initial measurements are of the most importance for the formation of the tribofilm.

The data presented in Figure 39 reveals that, at room temperature, the film thickness was highest when using glycerol. The observation of a glycerol tribofilm of this magnitude has not been noted in the literature and the values would only align with previous experiments if they would resemble the central film thickness (H_c) [15]. However, during the mapping step, the glass window load was set to 20 N without any movement. Consequently, only solid tribofilms should be measured. Therefore, it can be assumed that the film thickness values with glycerol are likely inaccurate and significantly influenced by wear on the ball surface or the silica spacer layer.

Azhaarudeen et al. [17] demonstrated the formation of a solid phosphate (P–O)-based amorphous tribo-chemical layer with a thickness of approximately 20 nm in the presence of ILs. The formation of this film, with an estimated height of 20 nm, can be demonstrated by the captured measurements presented in this work. Only with IL1 a deviation from these values is observable.
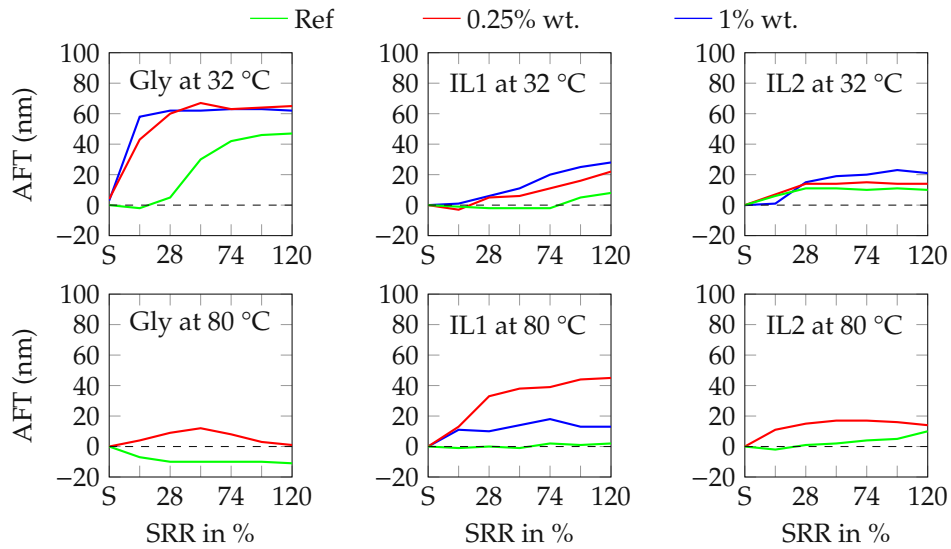
Figure 39: SLIM film thickness measurements

4.6 TEM Analysis of the Tribofilm

For additional analysis, the TECNAI F20 field emission electron microscope at USTEM was utilized to investigate the cut lamellae, with a particular focus on determining the formation of a tribofilm. The EDAX-AMETEK Apollo XLTW SDD module that is included in the TEM setup was used for measuring the composition of the film.

Figure 40 displays two scanning transmission electron microscopy (STEM) images of the lamellae cut from the IL1 samples containing 1 wt.-% of MXenes. This sample was selected because it demonstrated compatibility, as MXenes had the most significant impact on the COF, when combined with IL1 at a concentration of 1 wt.-% This suggests that MXenes notably influenced the structure of the IL1 tribofilm, leading to the observed improvements in COF within the mixed lubrication regime.

At the provided magnification, a tribofilm is already visible. However, for a more detailed assessment of this film, images with higher resolution were captured. Interestingly, the samples subjected to a maximum load of 10 N exhibit a thicker tribofilm, suggesting that under higher loads, the film dissociated. The dissociation under higher loads can be further discussed by observing that, while these tribofilms provided effective protection of the surfaces, their integrity was compromised at higher sliding loads and speeds. Mao et al. [148] observed that the triphenyl phosphate additives in their study formed tribofilms that effectively resisted scuffing. However, these protective films were gradually diminished at elevated sliding velocities [148]. This phenomenon mirrors the reduction in tribofilm thickness we noted in our research. Considering the heatmaps, this prompts the question of why the COF decreased more in areas with higher loads, even though the tribofilm was relatively thin. A possible explanation for this phenomenon is that the lower load conditions did not facilitate enough surface contact, thus preventing the full manifestation of the tribofilm's effects.

63
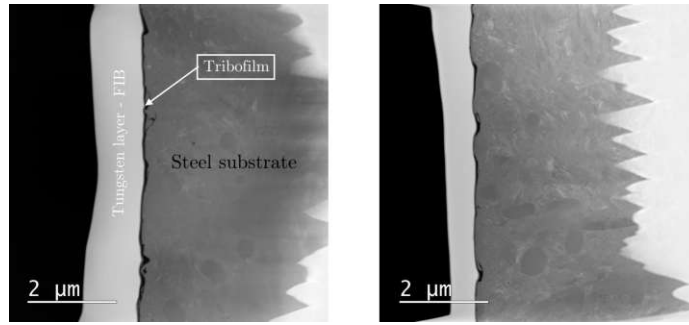
Figure 40: STEM analysis of the lamellae from the IL1-1 wt.-% MXene MTM samples subjected 10 N (left) and to a progressive loading sequence of 10 N, followed by 20 N and 30 N (right). This series showcases the structural evolution of the tribofilm as it undergoes increasing mechanical forces, highlighting the impact of load intensities on the thickness of the tribofilm.

In Figure 41, a targeted region within the lamellae that was chosen for in-depth analysis can be seen. The main reason for the selection of this specific area is the deep groove in the steel sample. The second image within the figure depicts the area that was chosen for the energy dispersive X-ray (EDX) map scan.
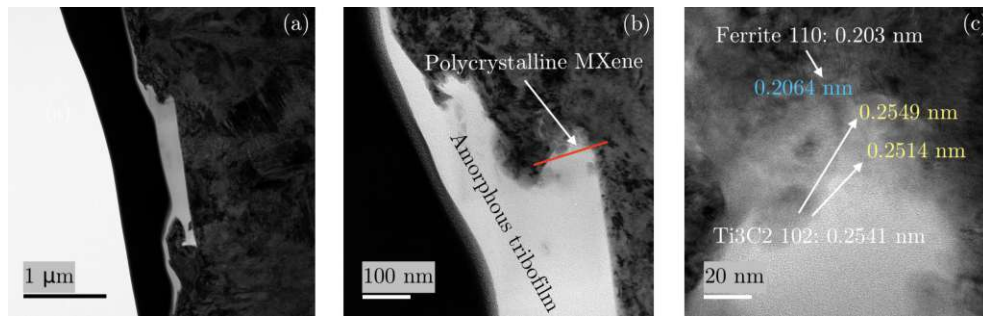
Figure 41: Progressive magnification (from left to right) showcasing the groove in the wearscar (a), the line for the EDX profile (b) and high-magnification lattice distance measurements compared with literature values (c)

The captured EDX map, as illustrated in Figure 42, reveals the presence of titanium within the tribofilm. The detection of MXene flakes within the film is a significant observation, underscoring the compatibility between IL1 and MXenes. It is anticipated that not all MXene flakes in the film were detected, owing to the limited resolution capabilities of the EDX setup. The majority of MXene flakes are likely oriented in the sliding direction. Consequently, MXenes that integrate into the film and align with the sliding direction are likely to present a thickness of merely one nanometer, surpassing the resolution limits of our EDX analysis. The identified flake is possibly a larger aggregation of MXene sheets or a singular flake that is oriented perpendicular to the sliding direction, facilitating its detection.
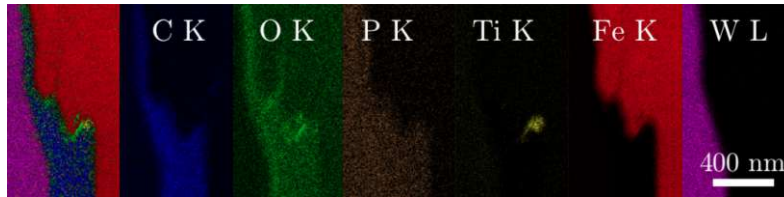
Figure 42: Graphical illustration of an EDX measurement, presenting an overlay (Image 1) and individual elementary maps detailing the selected area.

After the EDX map scan depicted in Figure 42, it became evident that MXenes had accumulated in specific regions of the tribofilm. To verify that the measured titanium from EDX corresponds to Ti_3C_2, lattice distances were measured. As illustrated in the third image of Figure 41, the observed lattice distances align with literature values for the used MXene. A detailed analysis of the region where titanium was detected indicated the lack of any distinctive stacks of MXene sheets. This suggests that the MXenes present are oriented in such a manner that their lateral dimensions are visible to us, rather than their stacked arrangement.

The white arrow in Figure 41 indicates the area where titanium was detected. A SAED measurement was conducted in this specific region to analyze the diffraction patterns from various crystallographic planes. The obtained d-spacing values were then compared with literature values, further validating the presence of Ti_3C_2 MXene in the tribofilm. As depicted in Figure 43, the distances measured align closely with the literature values provided by the USTEM department at the TU Vienna.

d (Å) (Literature)	d (Å)	Indices
9.4	9.35	0/0/2
2.54	2.52	1/0/2
2.02	2.08	1/0/6
1.5	1.49	1/1/2
1.2	1.19	1/0/14
1.04	1.04	0/0/18
0.93	0.93	1/1/16
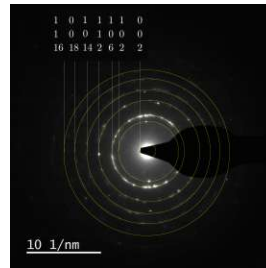
Figure 43: Table of d-spacings in Angstroms alongside the corresponding SAED pattern, illustrating the diffraction from various crystallographic planes.

The EDX line scan indicates a notable pattern: as the iron signals diminish, there's a simultaneous increase in the levels of oxygen, titanium and carbon. Interestingly, the phosphorus content remains notably reduced compared to measurements taken in other regions. Phosphorous would be expected, as also previous findings by Faruck et al. showed that the formed tribofilm typically consists of a phosphorus-oxygen-based amorphous layer [17].
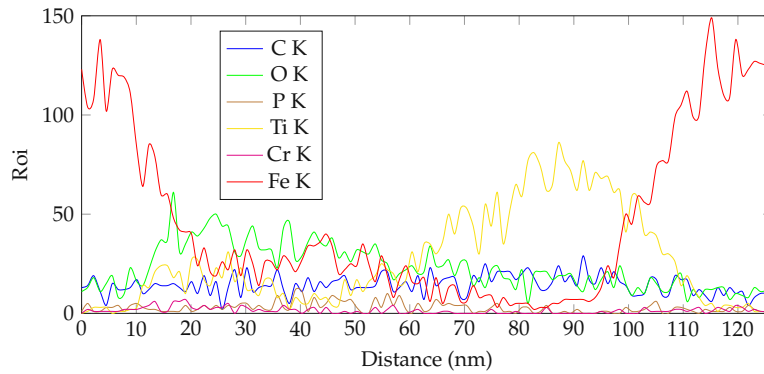
Figure 44: Region of interest (ROI) values of the EDX line profile.

After analyzing the MXene samples with TEM, we also examined the non-MXene samples to identify other potential differences of the tribofilm, aside from the incorporation of MXenes. During the FIB lamellae cutting, we noticed a persistent layer of liquid ILs on the sample. This layer, clearly not the amorphous tribofilm observed earlier, posed challenges during cutting and milling due to its movement. This highlights the complexities in the post-tribological treatment of samples with liquid lubricants and tribofilms. To preserve the tribofilm's integrity, we avoided using solvents or abrasive cleaning methods, explaining the residual liquid on the surface. Remarkably, despite these challenges, we succeeded in cutting and analyzing the lamella with the liquid IL layer intact. As shown in Figure 45, the thick layer between the steel substrate and the protective tungsten layer is not the tribofilm. However, the density and composition of the layer adjacent to the steel substrate suggest the presence of a solid tribofilm. Notably, its thickness appears comparable to that of the MXene-included samples.
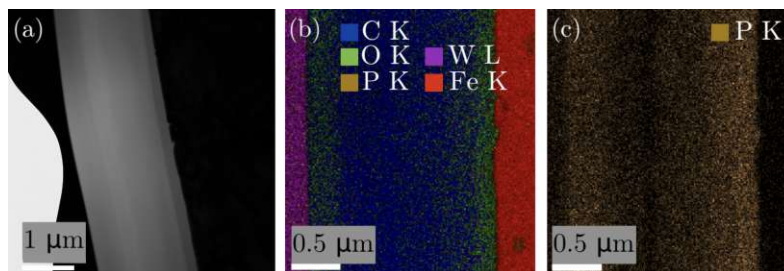
Figure 45: TEM image of the wear scar surface (a), EDX map overlay (b) and phosphorus-specific EDX map (c)

Discovering MXenes within the tribofilm formed in combination with ILs is an intriguing result. The incorporation of MXenes, known for their exceptional mechanical and electronic attributes, into tribofilms alongside a phosphate based amorphous layer suggests a complex enhancement of the film characteristics. Firstly, MXenes might provide physical reinforcement, bolstering the tribofilm's resistance to wear and mechanical stresses due to their high mechanical strength and aspect ratio [65]. These physical reinforcements are a plausible explanation for the observed increase in the films load-carrying capacity. Additionally, the interaction between MXenes and ILs may increase chemical stability within the tribofilm [149]. This interaction

could lead to the formation of a more durable tribofilm structure. Moreover, the thermal conductivity of MXenes benefits the tribofilm by aiding in the dissipation of the heat generated during tribological processes [150], potentially mitigating the thermal degradation of both the lubricant and the contact surfaces. This aspect is particularly critical in maintaining the integrity and performance of the tribofilm under high-friction conditions (like in the Brugger-Tester). Lastly, the low COFs of MXenes, attributed to the easy sliding of their sheets with minimal resistance [82], plays a crucial role in this context. When combined with the lubricating properties of ILs, known for their thermal stability and low volatility, a synergistic effect emerges. Therefore we anticipate, that this combination also leverages the unique sliding mechanism of MXene sheets to further enhance the tribofilm's effectiveness. The combination of physical reinforcement, chemical stability, thermal management and enhanced lubricity underlines the complex yet beneficial interactions between MXenes and ILs within the tribofilm.

5 Conclusion and Outlook

The primary aim of this study was to evaluate the tribological performance of three different lubrication systems across a broad spectrum of testing parameters. ILs with identical cations (trioctyl(methyl)phosphonium) but differing in their anions' alkyl chain lengths, specifically, dimethyl phosphate (IL1) and dibutyl phosphate (IL2) were used. Glycerol was the third lubricant that was tested. The compatibility of these lubricants with MXenes was a key focus, driven by the growing anticipation that MXenes will become common tribological additives for future lubricants. We assessed the performance of our selected lubricants integrated with two distinct MXene concentrations (0.25 and 1 wt.-%), comparing their effectiveness and compatibility.

Visual assessment of dispersion stability revealed that MXenes exhibit outstanding dispersibility in both ILs over 24 hours and glycerol. This stability can be attributed to the inherent ionic characteristics of the ILs, which promote electrostatic interactions with the polar MXenes. Additionally, the potential for hydrogen bond formation between the negatively charged ions of the ILs and the hydroxyl (OH) terminations on the MXenes, along with the ILs' high viscosity, plays a crucial role in preventing reagglomeration.

The COF measurements presented complex outcomes, underscoring that the effectiveness of MXene additives in lubrication is significantly influenced by the precise conditions of the tribological tests. Glycerol, despite having the lowest COF among the tested lubricants, showed negligible enhancement with the incorporation of MXenes. More often, combining glycerol with MXenes led to a notable increase in COF. A different approach with glycerol-water-MXene mixture, despite its potential, did not yield COFs that aligned with the favorable results reported by other researchers on silica based surfaces. Raman spectroscopy of this sample confirmed MXene and glycerol presence on the steel surfaces. Film thickness calculations were in a range as the MXene's lateral dimensions, indicating that MXenes might prevent the formation of a seamless lubricating layer.

In contrast, due to the addition of MXenes, the two ILs experienced a significant COF reduction in certain scenarios, with reductions reaching up to 100 %. Previous investigations by our team have demonstrated that these ILs form an amorphous tribofilm on steel surfaces. Our analysis with TEM revealed a 20-50 nm thick phosphorus-oxygen-based amorphous layer containing MXenes. The incorporation of MXenes within this tribofilm is believed to substantially enhance the IL lubricants' performance. A combination of longer alkyl chains in anions and the viscosity contributes to thicker tribolayers, enhancing the performance of IL1, in combination with MXenes. This results in less stress on the IL1 tribolayer, slowing degradation and boosting wear resistance.

A critical observation in this work is the harmful effect of the applied ILs on rubber polymers, leading to degradation and damage. This phenomenon is of particular concern in industrial applications where rubber components are integral to machinery and device function, such as in seals, gaskets, and flexible joints. The compatibility of lubricants with rubber polymers is essential to ensure longevity and reliability of

equipment. This interaction prompts the need for developing or identifying alternative ILs that are compatible with rubber materials.

It is known that the performance of MXenes greatly depends on the nature of the contacting surfaces. Given that most industrial contact surfaces are steel-on-steel, the results from this work highlight the crucial importance of surface compatibility. Therefore, identifying MXenes that are particularly compatible with steel-on-steel contacts is essential to optimize performance in widespread industrial applications.

Building on the insights gained, the following key areas are identified for further exploration:

- Finding rubber-compatible ionic liquids, ensuring their safe use in machinery.

- Long-term durability studies, particularly to evaluate the implications of MXene oxidation when used as lubricant additives in industrial applications.

- Evaluating viscosity under different pressures is crucial to comprehend the impact of MXene addition on the lubricant's rheological behavior.

- For future research, measuring the adhesion of lubricants with and without MXene additives is crucial. This will help to understand how MXenes affect surface interactions of the base lubricants.

- Further assessment of the biocompatibility and environmental impact of ILs and MXenes is necessary to ascertain their suitability and sustainability in tribological applications.

List of Figures

References

[1] Kenneth Holmberg. Reliability aspects of tribology. *Tribology International*, 34: 801–808, 12 2001. doi: 10.1016/S0301-679X(01)00078-0.

[2] Adedotun Adetunla, Adeniran Afolalu, Tien-Chien Jen, and Ayodele Ogundana. The development of tribology in lubrication systems of industrial applications: Now and future impact. *E3S Web of Conferences*, 391, 06 2023. doi: 10.1051/e3sconf/202339101013.

[3] Kenneth Holmberg and Ali Erdemir. The impact of tribology on energy use and co2 emission globally and in combustion engine and electric cars. *Tribology International*, 135, 03 2019. doi: 10.1016/j.triboint.2019.03.024.

[4] Joseph Kayode, Adeniran Afolalu, Moses Emetere, Stella Monye, and Lukeman Lawal. Application and impact of tribology in energy-an overview. *E3S Web of Conferences*, 391, 06 2023. doi: 10.1051/e3sconf/202339101081.

[5] Kenneth Holmberg and Ali Erdemir. Global impact of friction on energy consumption, economy and environment. *FME Transactions*, 43:181–185, 01 2015. doi: 10.5937/fmet1503181H.

[6] Shuai Zhang, Tian-Bao Ma, Ali Erdemir, and Qunyang Li. Tribology of two-dimensional materials: From mechanisms to modulating strategies. *Materials Today*, 26, 12 2018. doi: 10.1016/j.mattod.2018.12.002.

[7] Diana Berman, Ali Erdemir, and Anirudha Sumant. Approaches for achieving superlubricity in two-dimensional materials. *ACS Nano*, 12, 03 2018. doi: 10.1021/acsnano.7b09046.

[8] Jiahao Yuan, Rong Yang, and Guangyu Zhang. Structural superlubricity in 2d van der waals heterojunctions. *Nanotechnology*, 33, 12 2021. doi: 10.1088/1361-6528/ac1197.

[9] Philipp Grützmacher, Aura Tolosa, Carsten Gachot, Guichen Song, Wang Bo, Volker Presser, Frank Mücklich, Babak Anasori, and Andreas Rosenkranz. Superior wear-resistance of ti3c2t x multilayer coatings. *ACS Nano*, 15, 04 2021. doi: 10.1021/acsnano.1c01555.

[10] Andreas Rosenkranz, M. Clelia Righi, Anirudha Sumant, Babak Anasori, and Vadym Mochalin. Perspectives of 2d mxene tribology. *Advanced Materials*, 35, 12 2022. doi: 10.1002/adma.202207757.

[11] Yi Shuang, Jinjin Li, Yanfei Liu, Xiangyu Ge, Jie Zhang, and Jianbin Luo. In-situ formation of tribofilm with ti3c2tx mxene nanoflakes triggers macroscale superlubricity. *Tribology International*, 154, 10 2020. doi: 10.1016/j.triboint.2020.106695.

[12] Guido Boidi, João Carlos Queiroz, Francisco Profito, and Andreas Rosenkranz. Ti3c2tx mxene nanosheets as lubricant additives to lower friction under high loads, sliding ratios, and elevated temperatures. 12 2022. doi: 10.1021/acsanm.2c05033.

[13] Mohd Ab Rani, A Brant, L Crowhurst, A Dolan, Matthew Lui, Nur Hassan, Jason Hallett, Patricia Hunt, H Niedermeyer, Juan Perez-Arlandis, M Schrems, T Welton, and R Wilding. Understanding the polarity of ionic liquids. *Physical chemistry chemical physics : PCCP*, 13:16831–40, 08 2011. doi: 10.1039/c1cp21262a.

[14] Ichiro Minami. Ionic liquids in tribology. *Molecules (Basel, Switzerland)*, 14: 2286–305, 02 2009. doi: 10.3390/molecules14062286.

[15] Yijun Shi, Ichiro Minami, Mattias Grahn, Marcus Björling, and Roland Larsson. Boundary and elastohydrodynamic lubrication studies of glycerol aqueous solutions as green lubricants. *Tribology International*, 69:39–45, 01 2014. doi: 10.1016/j.triboint.2013.08.013.

[16] Yanfei Liu, Jinjin Li, Xiangyu Ge, Yi Shuang, Hongdong Wang, Yuhong Liu, and Jianbin Luo. Macroscale superlubricity achieved on the hydrophobic graphene coating with glycerol. *ACS Applied Materials & Interfaces*, 12:18859–18869, 04 2020. doi: 10.1021/acsami.0c01515.

[17] Azhaarudeen Anifa Mohamed Faruck, Philipp Grützmacher, Chia-Jui Hsu, Dominik Dworschak, Hsiu-Wei Cheng, Markus Valtiner, Kristof Stagel, Philipp Mikšovsky, Apurba Sahoo, Aitor Martinez, Katharina Bica-Schröder, Michael Weigand, and Carsten Gachot. Applying ionic liquids as oil additives for gearboxes: Going beyond the state of the art by bridging the nano-scale and component level. *Friction*, 11:1–22, 07 2022. doi: 10.1007/s40544-022-0650-5.

[18] Duncan Dowson. *History of Tribology*. 03 1998. ISBN 978-1-860-58070-3.

[19] G. Amontons. De la resistance causee dans les machines. *Mem. Acad. R.*, pages 275–282, 1699.

[20] C. A. Coulomb. Theorie des machines simples, en ayant egard au frottement de leurs parties, et a la roideur des cordages. *Mem. Math. Phys*, No. 10:161–342, 1785.

[21] F. P. Bowden and D. Tabor. Mechanism of metallic friction. *Nature*, 150(3798): 198, 1942.

[22] Peter Jost. *Lubrication (Tribology) - A report on the present position and industry's needs*. H. M. Stationery Office, London, UK, 1966. Department of Education and Science.

[23] Ian M. Hutchings and Philip H. Shipway. *Tribology: Friction and Wear of Engineering Materials*. Elsevier, Oxford, UK, 2017. ISBN 978-0-08-100910-8.

[24] ASM International. *ASM Handbook Volume 18, "Friction, Lubrication, and Wear Technology"*. American Society for Metals, Metals Park, Ohio, 1992.

[25] D M Nuruzzaman, M A Chowdhury, and M L Rahaman. Effect of duration of rubbing and normal load on friction coefficient for polymer and composite materials. *Industrial Lubrication and Tribology*, 63:320–326, 2011.

[26] A. Meshref, A. Mazen, and Y. Ali. Wear behavior of hybrid composite reinforced with titanium dioxide nanoparticles. *Journal of Advanced Engineering Trends*, 39: 89–101, 2020. doi: 10.21608/jaet.2020.75738.

[27] Tribonet. Wear - tribonet. `https://www.tribonet.org/wiki/wear/`, 2022. Accessed on 2024-02-10.

[28] Akimasa Tsujimoto, Wayne Barkmeier, Robert Erickson, Kie Nojiri, Yuko Nagura, Toshiki Takamizawa, Mark Latta, Masashi Miazaki, and Nicholas Fischer. Wear of resin composites: Current insights into underlying mechanisms, evaluation methods and influential factors. *Japanese Dental Science Review*, 54, 12 2017. doi: 10.1016/j.jdsr.2017.11.002.

[29] Gwidon W. Stachowiak and Andrew W. Batchelor. *Engineering Tribology*. Elsevier, Oxford, UK, 4 edition, 2013. ISBN 978-0-12-397047-3.

[30] Dariush Semnani. *Geometrical characterization of electrospun nanofibers*, pages 151–180. 01 2017. ISBN 9780081009079. doi: 10.1016/B978-0-08-100907-9. 00007-6.

[31] Duncan Dowson. Elastohydrodynamic lubrication. Technical report, NASA, Washington: Interdisciplinary Approach to the Lubrication of Concentrated Contacts, 1970.

[32] Bernard J. Hamrock and Duncan Dowson. Isothermal elastohydrodynamic lubrication of point contacts: Part 1—theoretical formulation. *Journal of Tribology*, pages 223–228, 1976.

[33] Ton Lubrecht, C. Venner, and François Colin. Film thickness calculation in elasto-hydrodynamic lubricated line and elliptical contacts: The dowson, higginson, hamrock contribution. *Proceedings of The Institution of Mechanical Engineers Part J-journal of Engineering Tribology - PROC INST MECH ENG J-J ENG TR*, 223:511–515, 05 2009. doi: 10.1243/13506501JET508.

[34] Emmanuelle Querlioz, Fabrice Ville, H. Lenon, and Ton Lubrecht. Experimental investigations on the contact fatigue life under starved conditions. *Tribology International*, 40:1619–1626, 10 2007. doi: 10.1016/j.triboint.2006.11.002.

[35] Richard Stribeck. *Kugellager für beliebige Belastungen*. Buchdruckerei AW Schade, Berlin N., 1901.

[36] Michael Naguib, Murat Kurtoglu, Volker Presser, Jun Lu, Junjie Niu, Min Heon, Lars Hultman, Yury Gogotsi, and Michel Barsoum. Two-dimensional nanocrystals produced by exfoliation of ti3alc2. *Advanced materials (Deerfield Beach, Fla.)*, 23:4248–53, 10 2011. doi: 10.1002/adma.201102306.

[37] Zhimei Sun, Denis Music, Rajeev Ahuja, Sa Li, and Jochen Schneider. Bonding and classification of nanolayered ternary carbides. *Physical review. B, Condensed matter*, 20, 09 2004. doi: 10.1103/PhysRevB.70.092102.

[38] Michael Naguib, Vadym Mochalin, Michel Barsoum, and Yury Gogotsi. Cheminform abstract: 25th anniversary article: Mxenes: A new family of two-dimensional materials. *ChemInform*, 45, 04 2014. doi: 10.1002/chin.201417232.

[39] Yury Gogotsi and Qing Huang. Mxenes: Two-dimensional building blocks for future materials and devices. *ACS Nano*, 15:5775–5780, 04 2021. doi: 10.1021/acsnano.1c03161.

[40] Mikhail Shekhirev, Christopher Shuck, Asia Sarycheva, and Yury Gogotsi. Characterization of mxenes at every step, from their precursors to single flakes and assembled films. *Progress in Materials Science*, 120, 11 2020. doi: 10.1016/j.pmatsci.2020.100757.

[41] Liu Yong, Xuefeng Zhang, Shangli Dong, Zhuyu Ye, and Yidan Wei. Synthesis and tribological property of ti3c2t x nanosheets. *Journal of Materials Science*, 52, 02 2017. doi: 10.1007/s10853-016-0509-0.

[42] Ali Nikkhah, Hasan Nikkhah, Hadis langari, Alireza Nouri, Abdul Mohammad, Wei Lun Ang, Ng Yong, Rosiah Rohani, and Ebrahim Mahmoudi. Mxene: From synthesis to environment remediation. *Chinese Journal of Chemical Engineering*, 61, 04 2023. doi: 10.1016/j.cjche.2023.02.028.

[43] Quanpeng Yang, Stefan Eder, Ashlie Martini, and Philipp Grützmacher. Effect of surface termination on the balance between friction and failure of ti3c2tx mxenes. 10 2022. doi: 10.21203/rs.3.rs-2130945/v1.

[44] Anupma Thakur, Nithin B.S., Karis Davidson, Annabelle Bedford, Hui Fang, Yooran Im, Vaishnavi Kanduri, Brian Wyatt, Kartik Nemani, Valeriia Poliukhova, Ravi Kumar, Zahra Fakhraai, and Babak Anasori. Step-by-step guide for synthesis and delamination of ti 3 c 2 t x mxene. *Small Methods*, 7, 05 2023. doi: 10.1002/smtd.202300030.

[45] Michel Barsoum and Miladin Radovic. Mechanical properties of the max phases. *Annual Review of Materials Research*, 41:195–227, 07 2011. doi: 10.1146/annurev-matsci-062910-100448.

[46] Xiaoyao Wang, Cyril Garnero, Guillaume Rochard, Damien Magne, Sophie Morisset, Simon Hurand, Patrick Chartier, Julie Rousseau, Thierry Cabioch, C. Coutanceau, Vincent Mauchamp, and Stéphane Celerier. New etching environment (fef3/hcl) for the synthesis of two-dimensional titanium carbide mxenes: a route towards selective reactivity vs water. *J. Mater. Chem. A*, 5, 09 2017. doi: 10.1039/C7TA01082F.

[47] Liyuan Liu, Metin Orbay, Sha Luo, Sandrine Duluard, Hui Shao, Justine Harmel, Patrick Rozier, Pierre-Louis Taberna, and P. Simon. Exfoliation and delamination of ti 3 c 2 t x mxene prepared via molten salt etching route. *ACS Nano*, 16, 11 2021. doi: 10.1021/acsnano.1c08498.

[48] Jizhang Chen, Minfeng Chen, Weijun Zhou, Xinwu xu, Bo Liu, Wenqing Zhang, and Chingping Wong. Simplified synthesis of fluoride-free ti3c2tx via electrochemical etching toward high-performance electrochemical capacitors. *ACS nano*, 16, 01 2022. doi: 10.1021/acsnano.1c09004.

[49] Tianran Zhang, Xi Jiang, Guochun Li, Qiaofeng Yao, and Jim Lee. A red phosphorous-assisted ball-milling synthesis of few layered ti3c2tx (mxene) nanodot composite. *ChemNanoMat*, 4, 08 2017. doi: 10.1002/cnma.201700232.

[50] Tahta Amrillah, che azurahanim che abdullah, Fitri Sari, Angga Hermawan, and Vani Alviani. Towards greener and more sustainable synthesis of mxenes: A review. *Nanomaterials*, 12:4280, 12 2022. doi: 10.3390/nano12234280.

[51] Di Wang, Chenkun Zhou, Alexander S. Filatov, Wooje Cho, Francisco Lagunas, Wang Mingzhan, Suriyanarayanan Vaikuntanathan, Chong Liu, Rober Klie, and Dmitri Talapin. Direct synthesis and chemical vapor deposition of 2d carbide and nitride mxenes. 12 2022. doi: 10.48550/arXiv.2212.08922.

[52] Louisiane Verger, Chuan Xu, Varun Natu, Hui-Ming Cheng, Wencai Ren, and Michel Barsoum. Overview of the synthesis of mxenes and other ultrathin 2d transition metal carbides and nitrides. *Current Opinion in Solid State and Materials Science*, 23, 03 2019. doi: 10.1016/j.cossms.2019.02.001.

[53] Siavash Iravani. Mxenes and mxene-based (nano)structures: A perspective on greener synthesis and biomedical prospects. *Ceramics International*, 48, 05 2022. doi: 10.1016/j.ceramint.2022.05.137.

[54] Faisal Shahzad, Mohamed Alhabeb, Christine Hatter, Babak Anasori, Soon Hong, Chong Min Koo, and Yury Gogotsi. Electromagnetic interference shielding with 2d transition metal carbides (mxenes). *Science*, 353:1137–1140, 09 2016. doi: 10.1126/science.aag2421.

[55] Qingxiao Zhang, Runze Fan, Weihua Cheng, Peiyi Ji, Jie Sheng, Qingliang Liao, Huirong Lai, Xueli Fu, Chenhao Zhang, and Hui Li. Synthesis of large-area mxenes with high yields through power-focused delamination utilizing vortex kinetic energy. *Advanced Science*, 9:2202748, 08 2022. doi: 10.1002/advs.202202748.

[56] Jizhen Zhang, Na Kong, Simge Uzun, Ariana Levitt, Shayan Seyedin, Peter Lynch, Si Qin, Meikang Han, Wenrong Yang, Jingquan Liu, Xungai Wang, Yury Gogotsi, and Joselito Razal. Scalable manufacturing of free-standing, strong ti 3 c 2 t x mxene films with outstanding conductivity. *Advanced Materials*, 32:2001093, 04 2020. doi: 10.1002/adma.202001093.

[57] Philipp Grützmacher, Roman Neuhauser, Kristof Stagel, Katharina Bica-Schröder, Guido Boidi, Carsten Gachot, and Andreas Rosenkranz. Combining tailored ionic liquids with ti 3 c 2 t x mxenes for an enhanced load-carrying capacity under boundary lubrication. *Advanced Engineering Materials*, 06 2023. doi: 10.1002/adem.202300721.

[58] Jun Zhao, Yiyao Huang, Yongyong He, and Yijun Shi. Nanolubricant additives: A review. *Friction*, 9, 12 2020. doi: 10.1007/s40544-020-0450-8.

[59] Bharat Bhanvase and Divya Barai. *Nanofluids for Heat and Mass Transfer: Fundamentals, Sustainable Manufacturing and Applications*. 01 2021. doi: 10.1016/B978-0-12-821955-3.09993-3.

[60] Daxiong Wu, Haitao Zhu, Liqiu Wang, and Lumei Liu. Critical issues in nanofluids preparation, characterization and thermal conductivity. *Current Nanoscience*, 5, 02 2009. doi: 10.2174/157341309787314548.

[61] Kathleen Maleski, Vadym Mochalin, and Yury Gogotsi. Dispersions of two-dimensional titanium carbide mxene in organic solvents. *Chemistry of Materials*, 29, 02 2017. doi: 10.1021/acs.chemmater.6b04830.

[62] Jianfeng Shen, Yongmin He, Jingjie Wu, Caitian Gao, Kunttal Keyshar, Xiang Zhang, Yingchao Yang, Mingxin Ye, Robert Vajtai, Jun Lou, and Pulickel Ajayan. Liquid phase exfoliation of two-dimensional materials by directly probing and matching surface tension components. *Nano letters*, 15, 07 2015. doi: 10.1021/acs.nanolett.5b01842.

[63] Aamir Iqbal, Junpyo Hong, Tae Ko, and Chong Min Koo. Improving oxidation stability of 2d mxenes: synthesis, storage media, and conditions. *Nano Convergence*, 8, 12 2021. doi: 10.1186/s40580-021-00259-6.

[64] Huma Bader Ul Ain, Tabussam Tufail, Farhan Saeed, Muhammad Arshad, Tanazzam Tufail, Ahmad Din, Madiha Khan Niazi, and Muzzamal Hussain. *Sonication: An overview*, pages 1–18. 01 2023. ISBN 9780323959919. doi: 10.1016/B978-0-323-95991-9.00016-3.

[65] Xiaonan Miao, Zhangpeng Li, Shuwen Liu, Jinqing Wang, and Shengrong Yang. Mxenes in tribology: Current status and perspectives. *Advanced Powder Materials*, 2:100092, 09 2022. doi: 10.1016/j.apmate.2022.100092.

[66] Jin Yang, Beibei Chen, Hao-Jie Song, Hua Tang, and Changsheng Li. Cheminform abstract: Synthesis, characterization, and tribological properties of two-dimensional ti 3 c 2 . *Crystal Research and Technology*, 49, 11 2014. doi: 10.1002/crat.201400268.

[67] Roman Neuhauser. Solid lubrication of mxene coated mica studied with afm friction force microscopy. Project Thesis, Technische Universität Wien, 4 2021.

[68] Fangcheng Cao, Ye Zhang, Hongqing Wang, Karim Khan, Ayesha Khan Tareen, Wenjing Qian, and Hans Ågren. The oxidation chemistry of two-dimensional mxenes. *Advanced Materials*, 34, 02 2022. doi: 10.1002/adma.202107554.

[69] Roghayyeh Lotfi, Michael Naguib, Dundar Yilmaz, Jagjit Nanda, and Adri van Duin. A comparative study on the oxidation of two-dimensional ti 3 c 2 mxene structures in different environments. *Journal of Materials Chemistry A*, 6, 06 2018. doi: 10.1039/C8TA01468J.

[70] Roman Neuhauser. Mxene based dipole antenna: Evaluating the performance of Ti_3C_2 coated fabrics for communication applications. Project Thesis, Technische Universität Wien, 2 2023.

[71] Tyler Mathis, Kathleen Maleski, Adam Goad, Asia Sarycheva, Mark Anayee, Alexandre Foucher, Kanit Hantanasirisakul, Eric Stach, and Yury Gogotsi. Modified MAX Phase Synthesis for Environmentally Stable and Highly Conductive Ti3C2 MXene. *American Chemical Society*, 08 2020. doi: 10.26434/chemrxiv.12805280.

[72] Yonghee Lee, Seon Joon Kim, Yong-Jae Kim, Younghwan Lim, Yoonjeong Chae, Byeong-Joo Lee, Young-Tae Kim, Hee Han, Yury Gogotsi, and Chi Won Ahn. Oxidation-resistant titanium carbide MXene film. *Journal of Materials Chemistry A*, 8, 11 2019. doi: 10.1039/C9TA07036B.

[73] Touseef Habib, Xiaofei Zhao, Smit Shah, Yexiao Chen, Wanmei Sun, Hyosung An, Jodie Lutkenhaus, Miladin Radovic, and Micah Green. Oxidation stability of Ti3C2Tx MXene nanosheets in solvents and composite films. *2D Materials and Applications*, 3:8, 02 2019. doi: 10.1038/s41699-019-0089-3.

[74] K. Novoselov, A. Geim, S. Morozov, Da Jiang, Yanshui Zhang, S. Dubonos, Irina Grigorieva, and Anatoly Firsov. Electric field effect in atomically thin carbon films. *Nat. Mater.*, 6, 01 2004.

[75] Israt Ali, Muhammad Faraz Ud Din, and Zhi-Gang Gu. Mxenes thin films: From fabrication to their applications. *Molecules*, 27:4925, 08 2022. doi: 10.3390/molecules27154925.

[76] Qing Feng, Jing Yang, Mingyuan Dou, Shuai Zou, Lixia Wei, and Fuchuan Huang. Modified ti3c2tx mxene/go nanohybrids: An efficient lubricating additive for tribological applications. *Arabian Journal for Science and Engineering*, pages 1–13, 10 2023. doi: 10.1007/s13369-023-08303-9.

[77] Yury Gogotsi and Babak Anasori. The rise of mxenes. *ACS Nano*, 13:8491–8494, 08 2019. doi: 10.1021/acsnano.9b06394.

[78] Xianghua Zhang, Maoquan Xue, Xinghua Yang, Zhiping Wang, Guangsi Luo, Zhide Huang, Xiaoli Sui, and Changsheng Li. Preparation and tribological properties of ti3c2(oh)2 nanosheets as additives in base oil. *RSC Adv.*, 5, 12 2014. doi: 10.1039/C4RA13800G.

[79] Edoardo Marquis, Michele Cutini, Babak Anasori, Andreas Rosenkranz, and M. Clelia Righi. Nanoscale mxene interlayer and substrate adhesion for lubrication: A density functional theory study. *ACS Applied Nano Materials*, 5, 08 2022. doi: 10.1021/acsanm.2c01847.

[80] Kosty Firestein, Joel Treifeldt, Dmitry Kvashnin, Joseph Fernando, Chao Zhang, Alexander Kvashnin, Evgeny Podryabinkin, Alexander Shapeev, Dumindu Thanaweera Achchige, Pavel Sorokin, and Dmitri Golberg. Young's modulus and tensile strength of ti3c2 mxene nanosheets as revealed by in situ tem probing, afm nanomechanical mapping, and theoretical calculations. *Nano Letters*, 4, 07 2020. doi: 10.1021/acs.nanolett.0c01861.

[81] Mengrao Tang, Jiaming Li, Yu Wang, Wenjuan Han, Shichong Xu, Ming Lu, Wei Zhang, and Haibo Li. Surface terminations of mxene: Synthesis, characterization, and properties. *Symmetry*, 14:2232, 10 2022. doi: 10.3390/sym14112232.

[82] Wenwen Ma, Tongyang Li, Zhen Fang, Weimin Li, Huaguo Tang, Lizhi Zhang, Yuan Yu, and Zhuhui Qiao. Effect of ti3c2tx mxenes on tribological and rheological properties of greases. *Tribology International*, 191:109137, 11 2023. doi: 10.1016/j.triboint.2023.109137.

[83] Maoquan Xue, Zhiping Wang, Feng Yuan, Xianghua Zhang, Wei Wei, Hua Tang, and Changsheng Li. Preparation of tio 2 /ti 3 c 2 t x hybrid nanocomposites and their tribological properties as base oil lubricant additives. *RSC Adv.*, 7: 4312–4319, 01 2017. doi: 10.1039/C6RA27653A.

[84] Yalin Zhang, Xuzhao He, Miao Cao, Xiaojun Shen, Yaru Yang, Jie Yi, Jipeng Guan, Jianxiang Shen, Man Xi, Yuanjie Zhang, and Bolin Tang. Tribological and thermo-mechanical properties of tio2 nanodot-decorated ti3c2/epoxy nanocomposites. *Materials*, 14:2509, 05 2021. doi: 10.3390/ma14102509.

[85] Yanbao Guo, Xuanli Zhou, Deguo Wang, Xiaqing Xu, and Quan Xu. Nanomechanical properties of ti3c2 mxene. *Langmuir*, 2019, 10 2019. doi: 10.1021/acs. langmuir.9b02619.

[86] Karel Van Acker and Karen Vercammen. Abrasive wear by tio2 particles on hard and on low friction coatings. *Wear*, 256:353–361, 02 2004. doi: 10.1016/ S0043-1648(03)00462-9.

[87] Birleanu Corina, M. Pustan, Mircea Cioaza, Andreia Molea, Florin Popa, and Glad Contiu. Effect of tio2 nanoparticles on the tribological properties of lubricating oil: an experimental investigation. *Scientific Reports*, 12:5201, 03 2022. doi: 10.1038/s41598-022-09245-2.

[88] Maggel Deetlefs and Kenneth Seddon. Ionic liquids: Fact and fiction. *Chimica Oggi-Chemistry Today*, 24:16–23, 03 2006.

[89] Yurong Wang, Ping Yang, Bin Guo, Nan Jiang, Jinyin Chi, Jinjie Liu, Yijing Liang, Qiangliang Yu, Shuyan Yang, Feng Guo, Meirong Cai, and Feng Zhou. Functionalized phosphate ionic liquids as additives in peg with excellent tribological properties for boundary/mixed /elastohydrodynamic lubrication. *Tribology International*, 164:107242, 08 2021. doi: 10.1016/j.triboint.2021.107242.

[90] Intezar Mahdi, Rajnish Garg, and Anupam Srivastav. "zddp- an inevitable lubricant additive for engine oils", international journal of engineering and inventions (ijei) volume 1, issue 1, pp.48-49 . *"ZDDP- An Inevitable Lubricant Additive for Engine Oils", International Journal of Engineering and Inventions (IJEI)*, 1:2278–7461, 09 2012.

[91] CF Ye, WM Liu, YX Chen, and LG Yu. Room-temperature ionic liquids: A novel versatile lubricant. *Chemical communications (Cambridge, England)*, 21: 2244–5, 12 2001. doi: 10.1039/B106935G.

[92] Lili Zhu, Qin Zhao, Xinhu Wu, Gaiqing Zhao, and Xiaobo Wang. A novel phosphate ionic liquid plays dual role in synthetic ester oil: From synthetic catalyst to anti-wear additive. *Tribology International*, 97, 01 2016. doi: 10.1016/ j.triboint.2015.12.047.

[93] Haizhong Wang, Qiming Lu, Chengfeng Ye, Weimin Liu, and Zhaojie Cui. Friction and wear behaviors of ionic liquid of alkylimidazolium hexafluorophosphates as lubricants for steel/steel contact. *Wear*, 256:44–48, 01 2004. doi: 10.1016/S0043-1648(03)00255-2.

[94] Ty Christoff-Tempesta and Thomas Epps. Ionic-liquid-mediated deconstruction of polymers for advanced recycling and upcycling. *ACS macro letters*, 12: 1058–1070, 07 2023. doi: 10.1021/acsmacrolett.3c00276.

[95] Katarzyna Wilpiszewska and Tadeusz Spychaj. Ionic liquids: Media for starch dissolution, plasticization and modification. *Carbohydrate Polymers*, 86:424–428, 08 2011. doi: 10.1016/j.carbpol.2011.06.001.

[96] Megawati Zunita, Haryo Winoto, M. Fauzan, and Rahmat Haikal. Recent advances in plastics waste degradation using ionic liquid-based process. *Polymer Degradation and Stability*, 211:110320, 03 2023. doi: 10.1016/j.polymdegradstab. 2023.110320.

[97] Ya-Fai Yuan, Jinming Zhang, Baoqing Zhang, Jiajian Liu, Yan Zhou, Ming-Xuan Du, Lin-Xue Han, Kuang-Jie Xu, Xin Qiao, and Chenyang Liu. Polymer solubility in ionic liquids: Dominated by hydrogen bonding. *Physical Chemistry Chemical Physics*, 23, 09 2021. doi: 10.1039/D1CP03193G.

[98] Ali Mouawia, Arnaud Nourry, Annie-Claude Gaumont, Jean-François Pilard, and Isabelle Dez. Controlled metathetic depolymerization of natural rubber in ionic liquids: From waste tires to telechelic polyisoprene oligomers. *ACS Sustainable Chemistry & Engineering*, 5, 10 2016. doi: 10.1021/acssuschemeng. 6b01777.

[99] Yuta Tomimatsu, Hiroki Suetsugu, Kazuyoshi Kaneko, Hiroshi Abe, Takahiro Takekiyo, Yukihiro Yoshimura, and Akio Shimizu. Possible contamination of ionic liquids upon dissolution and absorption of rubber and resin components. *Journal of Molecular Liquids*, 278:78–85, 01 2019. doi: 10.1016/j.molliq.2019.01. 038.

[100] Jerzy Chruściel. *Silicon-Based Polymers and Materials*. 01 2023. ISBN ISBN: 9783110639933 (hard cover).

[101] Azhaarudeen Faruck, Chia-Jui Hsu, Nicole Dörr, Michael Weigand, and Carsten Gachot. How lubricant formulations and properties influence the performance of rotorcraft transmissions under loss of lubrication conditions. *Tribology International*, 151:106390, 05 2020. doi: 10.1016/j.triboint.2020.106390.

[102] Arno Behr, Jens Eilting, Ken Irawadi, Julia Leschinski, and Falk Lindner. New chemical products on the basis of glycerol. *Chimica Oggi*, 26:13, 01 2008.

[103] Hamid Safaei, Mohsen Shekouhy, Sudabeh Rahmanpur, and Athar Shirinfeshan. Cheminform abstract: Glycerol as a biodegradable and reusable promoting medium for the catalyst-free one-pot three-component synthesis of 4h-pyrans. *Green Chemistry*, 14:1969, 10 2012. doi: 10.1039/C2GC35135H.

[104] Marcus Björling and Yijun Shi. Dlc and glycerol: Superlubricity in rolling/sliding elastohydrodynamic lubrication. *Tribology Letters*, 67:23, 01 2019. doi: 10.1007/s11249-019-1135-1.

[105] Bin Yu. Glycerol. *Synlett*, page 601–602, 01 2014. doi: 10.1055/s-0033-1340636.

[106] C. Matta, Lucile Joly-Pottuz, M. Bouchet, Jean Martin, Makoto Kano, Qing Zhang, and William Goddard. Superlubricity and tribochemistry of polyhydric alcohols. *Phys. Rev. B*, 78, 08 2008. doi: 10.1103/PhysRevB.78.085436.

[107] M. Bouchet, Jean Martin, José Ávila, Makoto Kano, Kentaro Yoshida, Takeshi Tsuruda, Shandan Bai, Yuji Higuchi, Nobuki Ozawa, Momoji Kubo, and Maria Asensio. Diamond-like carbon coating under oleic acid lubrication: Evidence for graphene oxide formation in superlow friction. *Scientific Reports*, 7:46394, 04 2017. doi: 10.1038/srep46394.

[108] Yun Long, M. Bouchet, Ton Lubrecht, Tasuku Onodera, and Jean Martin. Superlubricity of glycerol by self-sustained chemical polishing. *Scientific Reports*, 9:6286, 04 2019. doi: 10.1038/s41598-019-42730-9.

[109] Qingyuan Yu, Xinchun Chen, Chenhui Zhang, and Jianbin Luo. Influence factors on mechanisms of superlubricity in dlc films: A review. *Frontiers in Mechanical Engineering*, 6, 08 2020. doi: 10.3389/fmech.2020.00065.

[110] Qiang Ma, Wang Wei, and Guangneng Dong. Achieving macroscale liquid superlubricity using lubricant mixtures of glycerol and diols, 03 2021.

[111] Zhe Chen, Yuhong Liu, Zhang Shaohua, and Jianbin Luo. Controllable super lubricity of glycerol solution via environment humidity. *Langmuir : the ACS journal of surfaces and colloids*, 29, 08 2013. doi: 10.1021/la402422h.

[112] Gim Lim, Chin Soon, Nyuk Ling Ma, Marlia Morsin, Nafarizal Nayan, Mohd Ahmad, and Kian Tee. Cytotoxicity of MXene-based nanomaterials for biomedical applications: A mini review. *Environmental Research*, page 111592, 06 2021. doi: 10.1016/j.envres.2021.111592.

[113] Cheng-Yu Jin, Bangshang Zhu, Xuefeng Wang, and Qinghua Lu. Cytotoxicity of Titanium Dioxide Nanoparticles in Mouse Fibroblast Cells. *Chemical research in toxicology*, 21:1871–7, 09 2008. doi: 10.1021/tx800179f.

[114] Lili Chen, Muhammad Rana, Dr. Tanveer Haq, Njud Alharbi, Changlun Chen, and Xuemei Ren. Recent progress in environmental remediation, colloidal behavior and biological effects of MXene: A review. *Environmental Science: Nano*, 9, 01 2022. doi: 10.1039/D2EN00340F.

[115] Mostafa Firouzjaei, Kartik Nemani, Mohtada Sadrzadeh, Evan Wujcik, Mark Elliott, and Babak Anasori. Life cycle assessment of ti3c2tx mxene synthesis. *Advanced Materials*, 06 2023. doi: 10.1002/adma.202300422.

[116] Vijaya Bhaskar Reddy A, Mansoor Shah, Akil Ahmad, and Muhammad Moniruzzaman. *Introduction to ionic liquids and their environment-friendly applications*, pages 1–15. 01 2022. ISBN 9780128245453. doi: 10.1016/ B978-0-12-824545-3.00001-5.

[117] Deutsches Institut für Normung. Din 51347-2 prüfung von schmierstoffen prüfung im mischreibungsgebiet mit dem schmierstoffprüfgerät nach brugger teil 2: Verfahren für schmieröle. 2000.

[118] Shu Chen, Yuanfang Xiang, M. Banks, Chang Peng, Weijian Xu, and Ruoxi Wu. Correction: Polyoxometalate-coupled mxene nanohybrid via poly(ionic liquid) linkers and its electrode for enhanced supercapacitive performance. *Nanoscale*, 10, 11 2018. doi: 10.1039/C8NR90228C.

[119] Yong Li, Qiang Zhang, Weidong Zhou, Yongwang Huang, and Jingbin Han. Study on the dispersion and lubrication properties of ldh in lubricating oil. *Lubricants*, 11:147, 03 2023. doi: 10.3390/lubricants11030147.

[120] Shouhei Kawada, Seiya Watanabe, Shinya Sasaki, and Masaaki Miyatake. *Tribochemical Reactions of Halogen-Free Ionic Liquids on Nascent Steel Surface*, pages 47–65. 09 2018. ISBN 978-1-78984-117-6. doi: 10.5772/intechopen.77352.

[121] Hongling Fang, Yi Li, Songwei Zhang, Qi Ding, Litian Hu, and Kuan Louis. The superior lubricating performance and unique mechanism of oil-soluble protic ionic liquids with short alkyl chains. *Journal of Colloid and Interface Science*, 623, 05 2022. doi: 10.1016/j.jcis.2022.04.174.

[122] Meirong Cai, Qiangliang Yu, Weimin Liu, and Feng Zhou. Ionic liquid lubricants: when chemistry meets tribology. *Chemical Society Reviews*, 49:7753–7818, 11 2020. doi: 10.1039/D0CS00126K.

[123] Tribonet. Pressure viscosity coefficient and characteristics of lubricants. `https://www.tribonet.org/wiki/pressure-viscosity-coefficient-and-characteristics-of-lubricants/`, 2019. Accessed on 2024-02-10.

[124] A. Pensado, María Comuñas, and Josefa Fernández. The pressure–viscosity coefficient of several ionic liquids. *Tribology Letters*, 31:107–118, 08 2008. doi: 10.1007/s11249-008-9343-0.

[125] A. Pensado, María Comuñas, Luis Lugo, and Josefa Fernández. High-pressure characterization of dynamic viscosity and derived properties for squalane and two pentaerythritol ester lubricants: Pentaerythritol tetra2-ethylhexanoate and pentaerythritol tetranonanoate. *Industrial & Engineering Chemistry Research - IND ENG CHEM RES*, 45:2394–2404, 03 2006. doi: 10.1021/ie051275w.

[126] Xavier Paredes, Olivia Fandiño, A. Pensado, María Comuñas, and Josefa Fernández. Pressure–viscosity coefficients for polyalkylene glycol oils and other ester or ionic lubricants. *Tribology Letters*, 45:89–100, 01 2011. doi: 10.1007/s11249-011-9861-z.

[127] Félix Gaciño, Xavier Paredes, María Comuñas, and Josefa Fernández. Effect of the pressure on the viscosities of ionic liquids: Experimental values for 1-ethyl-3-methylimidazolium ethylsulfate and two bis(trifluoromethyl-sulfonyl)imide salts. *The Journal of Chemical Thermodynamics*, 54:302–309, 11 2012. doi: 10.1016/j.jct.2012.05.007.

[128] Leila Darabi and Morteza Zare. High correlate simple equations for temperature and pressure dependence of the viscosity of ionic liquids. *Chemical Physics*, 539:110933, 2020. ISSN 0301-0104. doi: 10.1016/j.chemphys.2020.110933.

[129] Thi-Na Ta, Shin-Yuh Chern, and Jeng-Haur Horng. Tribological behavior of ionic liquid with nanoparticles. *Materials*, 14:6318, 10 2021. doi: 10.3390/ma14216318.

[130] J.C. Dias, Daniela M. Correia, Carlos Costa, Gabriela Botelho, J. Vilas, and Senentxu Lanceros-Méndez. Thermal degradation behavior of ionic liquid/fluorinated polymer composites: Effect of polymer type and ionic liquid anion and cation. *Polymer*, 229:123995, 07 2021. doi: 10.1016/j.polymer.2021.123995.

[131] Lilla Lukács and Edit Cséfalvay. Compatibility study of viton, nbr 70 and epdm o-rings with selected solvents. *Periodica Polytechnica Chemical Engineering*, 61, 09 2016. doi: 10.3311/PPch.9606.

[132] J.-L Mansot, Yves Bercion, L. Romana, and Jean Martin. Nanolubrication. *Brazilian Journal of Physics (Brasil) Num.1A Vol.39*, 39, 04 2009. doi: 10.1590/S0103-97332009000200011.

[133] Hizb Ullah Sajid and Ravi Kiran. Improving the wettability of structural steels by employing ionic liquids. *Journal of Molecular Liquids*, 324, 12 2020. doi: 10.1016/j.molliq.2020.115137.

[134] Glenn Gyimah, Zhong-ning GUO, Ping HUANG, Shu-zhen JIANG, Gary Barber, Gui-xian LIU, and J. LIU. Improvers of pressure-viscosity coefficients of two-phase liquid-solid lubricants. *DEStech Transactions on Engineering and Technology Research*, 11 2016. doi: 10.12783/dtetr/amita2016/3562.

[135] Ekaterina Izgorodina and Douglas MacFarlane. Nature of hydrogen bonding in charged hydrogen-bonded complexes and imidazolium-based ionic liquids. *The journal of physical chemistry. B*, 115:14659–67, 12 2011. doi: 10.1021/jp208150b.

[136] Qiang Ma, Tao He, Arman Khan, Qian Wang, and Yip-Wah Chung. Achieving macroscale liquid superlubricity using glycerol aqueous solutions. *Tribology International*, 160:107006, 03 2021. doi: 10.1016/j.triboint.2021.107006.

[137] Tomas Zapletal, Petr Šperka, Ivan Krupka, and Martin Hartl. The effect of surface roughness on friction and film thickness in transition from ehl to mixed lubrication. *Tribology International*, 128, 08 2018. doi: 10.1016/j.triboint.2018.07.047.

[138] Ali Macknojia, Aditya Ayyagari, Elena Shevchenko, and Diana Berman. Mxene/graphene oxide nanocomposites for friction and wear reduction of rough steel surfaces. *Scientific Reports*, 13, 07 2023. doi: 10.1038/s41598-023-37844-0.

[139] Asia Sarycheva and Yury Gogotsi. Raman spectroscopy analysis of structure and surface chemistry of ti 3 c 2 t x mxene. *Chemistry of Materials*, XXXX, 04 2020. doi: 10.1021/acs.chemmater.0c00359.

[140] U. Balachandran and N. G. Eror. Raman spectra of titanium dioxide. *Journal of Solid State Chemistry*, 42:276–282, 1982.

[141] Ali Jaafar, Malik Mahmood, Roman Holomb, László Himics, Tamás Váczi, Anton Sdobnov, Valery Tuchin, and Miklos Veres. Ex-vivo confocal raman microspectroscopy of porcine skin with 633/785-nm laser excitation and optical clearing with glycerol/water/dmso solution. *Journal of Innovative Optical Health Sciences*, 14:2142003, 05 2021. doi: 10.1142/S1793545821420037.

[142] A new apparatus for finishing large size/large batch silicon nitride (si3n4) balls for hybrid bearing applications by magnetic float polishing (mfp). *International Journal of Machine Tools and Manufacture*, 46(2):151–169, 2006. ISSN 0890-6955. doi: 10.1016/j.ijmachtools.2005.04.015.

[143] Materials failure mechanisms of hybrid ball bearings with silicon nitride balls. *Tribology International*, 37(6):463–471, 2004. doi: 10.1016/j.triboint.2003.12.015.

[144] M. Han and Rosa Espinosa-Marzal. Molecular mechanisms underlying lubrication by ionic liquids: Activated slip and flow. *Lubricants*, 6, 07 2018. doi: 10.3390/lubricants6030064.

[145] Joanna Dawczyk, Neal Morgan, Joe Russo, and Hugh Spikes. Film thickness and friction of zddp tribofilms. *Tribology Letters*, 67, 02 2019. doi: 10.1007/s11249-019-1148-9.

[146] Ana Trajkovski, Sebastjan Matkovič, Nejc Novak, Irfan Nadeem, Mitjan Kalin, and Franc Majdic. Glycerol aqueous solutions for the enhanced tribological behaviour of polymer composites sliding against steel. *Tribology International*, 192:109173, 12 2023. doi: 10.1016/j.triboint.2023.109173.

[147] Lichun Hao, Yonggang Meng, and Cheng Chen. Experimental investigation on effects of surface texturing on lubrication of initial line contacts. *Lubrication Science*, 26, 08 2014. doi: 10.1002/ls.1265.

[148] Mao Ueda, Hugh Spikes, and Amir Kadiric. In-situ observation of the effect of the tribofilm growth on scuffing in rolling-sliding contact. *Tribology Letters*, 70, 06 2022. doi: 10.1007/s11249-022-01621-3.

[149] Xuan Yin, Jie Jin, Xinchun Chen, Andreas Rosenkranz, and Jianbin Luo. Ultra-wear-resistant mxenes-based composite coating via in-situ formed nanostructured tribofilm. *ACS Applied Materials & Interfaces*, 11, 08 2019. doi: 10.1021/acsami.9b11449.

[150] Ruiyang Kang, Guo Liang Chao, Junfeng Cui, Yapeng Chen, Hou Xiao, Wang Bo, Cheng-Te Lin, Nan Jiang, and Jinhong Yu. Enhanced thermal conductivity of epoxy composites filled with 2d transition metal carbides (mxenes) with ultralow loading. *Scientific Reports*, 9, 06 2019. doi: 10.1038/s41598-019-45664-4.